

---

# **Atomic Friction and Symmetry-Breaking Transitions in Ion Coulomb Systems**

---

**Von der QUEST-Leibniz-Forschungsschule der  
Gottfried Wilhelm Leibniz Universität Hannover  
zur Erlangung des Grades**

**Doktor der Naturwissenschaften  
Dr. rer. nat.**

**genehmigte Dissertation  
von**

**M.Sc. Jan Kiethe  
geboren am 26. Oktober 1988 in Dresden**

**2021**

Referentin: Prof. Dr. Tanja E. Mehlstäubler  
Korreferent: Prof. Dr. Luis Santos  
Korreferent: PD Dr. Michael Johanning  
Tag der Promotion: 07.05.2021

## Abstract

Trapped ion Coulomb crystals are regularly used as analogue simulators for physical systems, for which the access to the dynamics of the individual particles is lacking or which are hard to simulate using classical computers. One area of interest are solid-state friction models with two atomically flat surfaces sliding against each other. Typically, the access to the dynamics of the individual particles is lacking in realistic interfaces, therefore, ion crystals have been proposed in order to test friction models. While a model system of an ion chain sliding over a rigid optical potential has been demonstrated, a model system that implements back action between the two sliding surfaces does not exist.

In this cumulative thesis, an atomic system with intrinsic back action and access to individual particles that allows the study of nanofriction is presented. The system consists of an ion Coulomb crystal in the two-dimensional zigzag phase, into which a topological defect is introduced. The defect leads to a mismatch between the ion chains, which allows for the observation of the pinning-to-sliding phase transition for a finite system. The transition shows symmetry breaking and the existence of a soft mode at zero temperature, which is a localized topological defect mode. The influence of the defect's position and type on the existence of the soft mode is studied. It is found that breaking the intrinsic symmetry of the topological defect in the sliding phase by external forces prevents the observation of the soft mode. In the presented experiments, mode frequencies are determined with resonant excitation of the collective motions of the ions via amplitude modulation of a Doppler cooling laser. A non-zero soft mode frequency at the transition is measured, which is attributed to the finite crystal temperature.

Furthermore, the linear-to-zigzag transition and the zigzag mode, i.e., the soft mode of this transition, under thermal noise are investigated. An increase in the mode frequency with temperature, as well as fast switching between the two possible ground states of the two-dimensional zigzag phase is found. An analytical model is derived that explains the observed temperature dependence of the low-frequency spectrum at the linear-to-zigzag transition. This analysis has important consequences for the cooling of a soft mode near a symmetry-breaking transition. In the future, this model could be adaptable to the pinning-to-sliding transition in order to further the understanding of the thermal effects of friction and heat transport.

**Keywords:** Coulomb crystals, nanofriction, phase transitions, symmetry breaking, topological defects

## **NOTE**

This version of the manuscript has been compiled after the work was submitted, reviewed, and defended. While the content remains unchanged, the following text changes were made:

- reworked the initial sentence of the introduction to emphasize that trapped ions are only possible under ultra-high vacuum and that an ion crystal is an atomically pure system
- added new citations 8, 12-14 to the first paragraph of the introduction with respect to optical clocks based on ion crystals
- updated hyphenation of adverbs throughout the introduction and summary, e.g. "ultra low temperatures" was changed to "ultra-low temperatures"
- Figure 1: added symbols for the potential amplitude, lattice spacing, particle equilibrium distance, spring constant and ion distances
- added a mathematical description of the Frenkel-Kontorova model to the introduction with symbols for physical quantities. Exchanged text reference to these quantities with newly added symbols when discussing the Frenkel-Kontorova model.
- replaced publication 3 with published version in Physical Review B
- fixed typographical errors in acknowledgments

# Contents

|          |  |           |
|----------|--|-----------|
| <b>1</b> | <b>Introduction</b>  | <b>1</b>  |
| <b>2</b> | <b>P1: Probing nanofriction and Aubry-type signatures in a finite self-organized system</b>      | <b>7</b>  |
| <b>3</b> | <b>P2: Nanofriction and motion of topological defects in self-organized ion Coulomb crystals</b> | <b>17</b> |
| <b>4</b> | <b>P3: Finite-temperature spectrum at the symmetry-breaking linear to zigzag transition</b>      | <b>37</b> |
| <b>5</b> | <b>Summary and Outlook</b>   | <b>53</b> |



# 1 Introduction

Laser cooling multiple ions in an ion trap under ultra-high vacuum below a few tens of mK temperature, leads to the atomically pure state of matter, known as ion Coulomb crystals (ICCs) [1]. First found at the end of the 1980s [2, 3], these crystals are utilized nowadays in many research areas, such as quantum computing [4–6], ion clocks [7–15], precision test of fundamental physics [16] and analogue simulations with trapped ions [17–22]. At ultra-cold temperatures, they form a well-isolated quantum system, with internal electronic and external vibrational states, over which excellent control has been established [23]. This cumulative thesis is part of the ongoing effort to utilize ICCs for simulation of solid state systems. Specifically, it investigates two structural transitions in ICCs, that are related to friction between two atomically flat layers.

Tribology, the study of friction, covers phenomena ranging over several orders of magnitude [24], from earthquakes on the scale of the earth, over sliding of everyday objects, such as a tea cup on a kitchen counter, to molecules and DNA strands [25, 26]. Especially, with the emergence of nanotechnology [27, 28], the understanding of friction on the nanoscale is of importance for many applications, such as the design of molecular machines with lower energy dissipation [29, 30].

In everyday life, friction is encountered on the macroscopic level and is described by the heuristic laws discovered in the 17th century by Amontons and Coulomb [24]. It exists, because uneven surfaces at macroscopic length scales prevent sliding of two solid bodies against each other. This can lead to the build-up of stress in a system, until a certain threshold is reached, where for instance an earthquake occurs [24]. This is contrasted by the situation on the microscopic level, where atomically flat surfaces can exist, e.g., two layers of graphene sliding against each other [31]. Here, the direct interaction between the individual particles of the two surfaces becomes important. In the first half of the 20th century, several mathematical models were proposed for describing the sliding of atomically flat bodies. Two important models being the Prandtl-Tomlinson model for a single particle [32, 33] and the Frenkel-Kontorova (FK) model for a chain of particles [34, 35]. In both cases, one surface is approximated by a periodic corrugation potential  $U_{\text{corr}} = U \sin(2\pi z_i \lambda^{-1})$  preventing particles from moving laterally over it, where  $U$  is the potential amplitude,  $z_i$  is the lateral position of particle  $i$  and  $\lambda$  the lattice period. In the FK model the sliding surface is given by an infinite chain of particles with mass  $m$  connected to their neighbors by identical springs with stiffness  $\kappa$ , as illustrated in Fig. 1.1 (a). The potential energy between two neighboring particles is  $U_{\text{PP}} = \frac{1}{2}\kappa(z_{i+1} - z_i - a)^2$ , where  $z_i$  is the position of particle  $i$  and  $a$  is the equilibrium distance without the corrugation potential.

Roughly 50 years after the initial publication of the FK model, Aubry found an interesting regime, in which the friction force, needed to translate the particle chain, becomes effectively zero [36]. If the periodicity of the corrugation potential  $\lambda$  and the periodicity of the sliding surface  $a$  are incommensurate, i.e., the fraction  $a/\lambda$  is irrational, this frictionless regime can be reached.

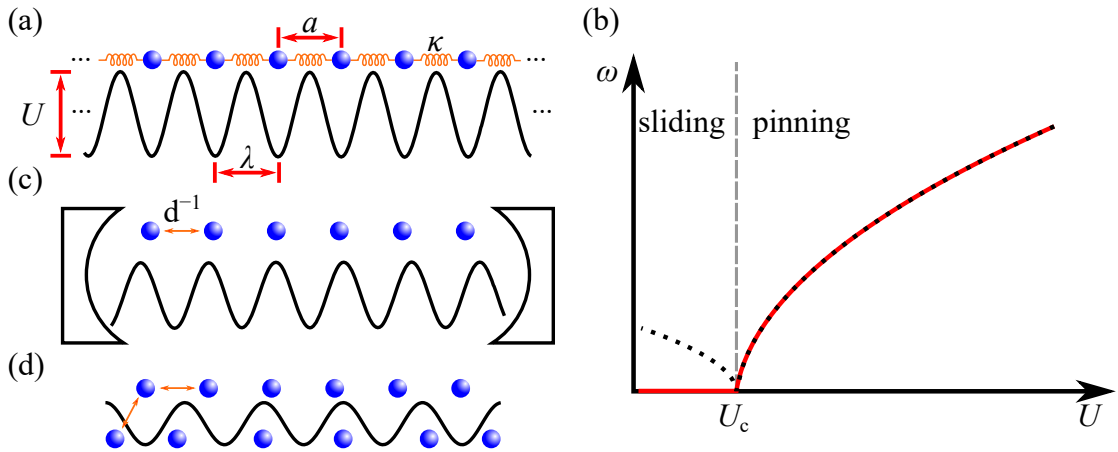


Figure 1.1: Overview friction models. (a) Frenkel-Kontorova model. An infinite chain of particles interacting with springs with stiffness  $\kappa$  is placed over a rigid, periodic corrugation potential with amplitude  $U$  and period  $\lambda$  that models the interaction of the other atomic surface. Without the corrugation potential the particles exhibit an uniform distance  $a$  between each other. (b) Schematic behavior of the soft mode. The frequency  $\omega$  of the vibrational mode that drives the pinning-to-sliding transition is plotted in dependence of the amplitude of the corrugation potential  $U$ . For the infinite case (red solid line) the frequency becomes zero at  $U_c$  and stays zero in the sliding phase. For the finite case (black dashed line) the frequency is only zero at  $U_c$  and finite in both the sliding and pinned phase. (c) Frenkel-Kontorova model implementation in trapped ions. A finite number of ions is confined in an ion trap, and placed in an optical cavity that generates the corrugation potential. The particle-particle interaction is given by the Coulomb potential, indicated by the orange arrow, inversely proportional to the distance  $d$  between neighboring ions. (d) Friction model with back action in trapped ions. An ion Coulomb crystal in the two-dimensional zigzag phase placed in an ion trap, here shown including a topological defect. The ions interact over the Coulomb potential indicated by the orange arrows, which also generates the mutual corrugation of the two chains.

For amplitudes of the corrugation potential  $U$  below a certain threshold  $U_c$ , the system is in the superlubric phase, where the interactions between the coupled particles counteract the friction due to the corrugation potential  $U_{\text{corr}}$  to allow for free sliding. For values above  $U_c$ , the system is in the pinned phase, where sliding motion is governed by the so-called stick-slip movement [32]. In this regime the particle chain will be repeatedly pinned to one potential well before moving to the next one.

The transition from the pinned phase to the superlubric phase is known as the pinning-to-sliding transition (PST) or the Aubry transition. The transition point of this second-order phase transition [36] can be identified with the help of several quantities, such as the static friction force, the hull function and the frequency of the sliding mode. The transition does not break the symmetry of the system in the ideal case of an infinite number of particles. It, however, breaks



---

the analytic behavior of the hull function [36], which parameterizes the reachable ground states under the presence of the corrugation potential. The hull function is continuous and therefore analytic in the sliding phase, while being discontinuous and non-differentiable, therefore no longer analytic, in the pinned phase. For finite-size systems, the PST still exists, but it becomes a symmetry-breaking transition [37]. Additionally, the static friction force needed to move the chain is non-zero above and below the transition. Only at the transition point, free sliding is possible. The transition is associated with a sliding vibrational mode, a collective oscillation of the chain over the potential. In order to determine the mode frequency, the equations of motion can be linearized for small oscillations around the equilibrium positions. At the transition point the frequency of the sliding mode  $\omega$  becomes zero and its amplitude diverges. Such a mode is often called a soft mode and its behavior is shown schematically in Fig. 1.1 (b). The frequency  $\omega$  stays zero as long as free sliding of the chain is possible [38]. In the finite system,  $\omega$  goes to zero frequency at the transition point, but it exhibits finite values above and below the transition.

The effect of reduced friction as predicted by Aubry was experimentally observed in systems with atomic scale contact of gold and graphene surfaces [31, 39, 40]. Using graphene flakes on the tip of an atomic force microscope sliding over a tungsten surface [31] allowed to modify the mismatch between the atomic lattices by changing the orientation of the flakes. Thus it was possible reach an regime of ultra-low friction for incommensurate, i.e., mismatched lattice constants.

However, these experiments lack *in-situ* access to the dynamics of individual particles during the sliding process. In order to find a controllable model system in which these degrees of freedom can be accessed, trapped ion Coulomb crystals inside an optical lattice have been proposed [41–43]. The optical lattice acts as the corrugation potential in this model system, while the Coulomb potential implements the particle-particle interaction, as displayed in Fig. 1.1 (c). These proposals were recently realized with up to five trapped ions placed in an optical resonator [44]. In further experiments the existence of the PST in a finite system, also called Aubry-type transition, was demonstrated [45]. This ion simulator allows to investigate the influence of velocity [46] on friction, and to observe the multi-slip behavior [47] and topological defects in the FK model [48].

Another experimental test system for the FK model with access to the particle dynamics are two-dimensional (2D) colloidal layers over optical periodic potentials [49]. This system consists of  $\mu\text{m}$  sized, charged polystyrene spheres suspended in water. When placing this sheet of spheres in an optical interference pattern, the spheres form triangular lattices [49]. In this 2D system, the Aubry-type transition was also found [50], which is a first-order transition due to the additional dimension.

Both approaches simulate the classical FK model for finite systems, in which one of the atomic layers is replaced by the periodic corrugation potential. In this model, the potential is treated as rigid and only the particle chain deforms. However, this is a simplification from realistic atomic surfaces [51, 52]. An example from nature is the sliding of F-actin filaments, which normally can be found in biological cells [53]. Both filaments are more or less identical and will therefore influence each other during a sliding process. In other words, the sliding chain exerts a back action on the corrugation potential, which is not captured by simulators implementing standard the FK model.

In the first publication contained in this cumulative thesis, P1, friction is studied in a self-

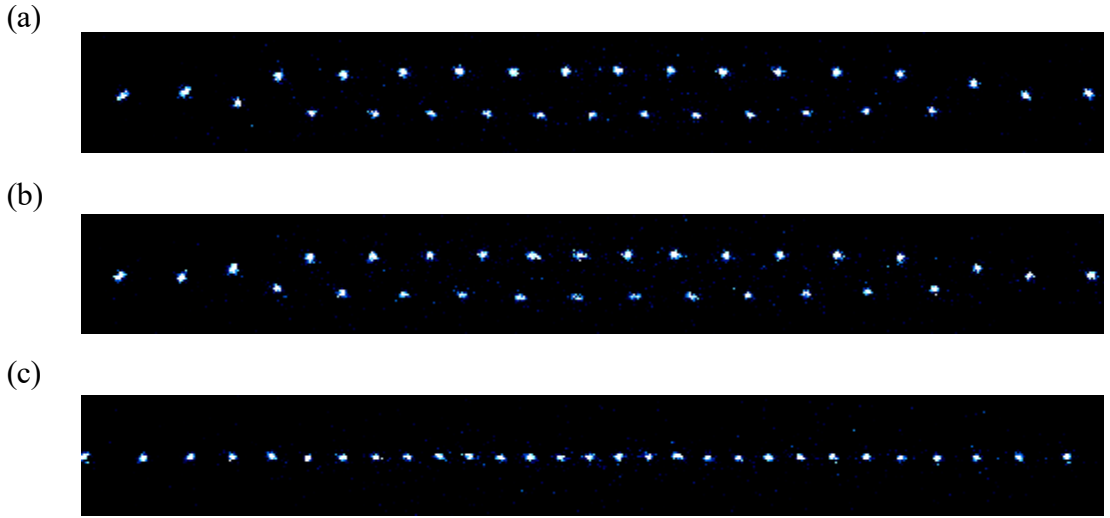


Figure 1.2: Photos of an ion Coulomb crystal with 30  $^{172}\text{Yb}^+$  ions in different phases. (a) Zigzag crystal. (b) Zigzag crystal with extended topological defect of the horizontal type. (c) Linear chain. Rightmost ion out of view.

organized ICC where the back action is intrinsically included [54]. In this model system, the ion crystal is in the 2D zigzag phase [55, 56] under the presence of a topological defect [57–61]. Example photos of a 2D crystals with and without a defect are shown in Fig. 1.2 (a) and (b). The 2D crystal can be interpreted as two linear ion chains on top of each other and the back action is given by the intrinsic Coulomb interaction between the ions of the two chains, see Fig. 1.1 (d). The main result of this publication is the demonstration, that the PST exists in a 2D Coulomb crystal with a topological defect, which enables tests of friction models that include back action. Typical signatures that identify the PST, such as the existence of a soft mode and symmetry-breaking [54] at the transition, are found.

Utilizing an ICC in the 2D phase as a model system circumvents technical issues, with respect to cooling ions into the wells of an optical lattice [62, 63] or with charge build-up in the trap by the light of the optical lattice. Even without an external corrugation potential, the amplitude of the corrugation can be chosen by the distance between the two chains, which is controlled by tuning the confining potential.

The topological defect in the 2D crystal introduces a mismatch between the ion-to-ion distance of the two chains, which is needed to observe reduced friction effects. The defects are generated with a certain probability by the Kibble-Zurek mechanism [57, 59–61, 64, 65], as the system is changed from the linear chain, see Fig. 1.2 (c), to the 2D phase. Different kinds of defects can be identified [66, 67], based on their local structure, and this type generally depends on the trapping potentials and the number of ions [66]. While it is possible to choose between matched lattice periods (zigzag crystal without topological defect) and mismatched lattice periods (zigzag crystal with topological defect), the actual value of the lattice mismatch cannot be chosen freely in the presented system. It is given by the Coulomb interaction, ion number and trapping ratios,

---

and cannot be chosen independently from them, unlike in the simulators that implement the FK model directly [44].

The intrinsic mirror symmetry of the topological defect along the transverse crystal center, see Fig. 1.2 (b), is broken when the system enters the pinning regime. This can be understood with the potential for the topological defect, known as the Peierls-Nabarro potential [35, 67]. In the symmetric regime, only a single ground state for the defect exists, while in the pinning regime, multiple ground states are found [54, 67, 68].

In P1 the existence of a soft mode for  $T = 0$  was demonstrated. It is a localized defect normal mode, for which the two ion chains shear against each other in the crystal center. Experimentally, the frequency of this mode is measured using an amplitude modulated cooling laser beam addressing the electronic  ${}^2S_{1/2} \leftrightarrow {}^2P_{1/2}$  dipole transition in  ${}^{172}\text{Yb}^+$ . This represents the first direct frequency measurement of the localized low frequency mode of the topological defect. Besides its importance for the PST, the measured mode might be of interest as a carrier of quantum information in ring traps [69] and for transport properties in ICCs [70]. In the experiment, the expected soft mode behavior is not observed, which is attributed to the finite temperature of the ion Coulomb crystal, cooled near the Doppler limit of  ${}^{172}\text{Yb}^+$ , i.e.  $T_D \approx 0.5\text{ mK}$ .

In the second publication contained in this thesis, P2, the influence of the properties of the topological defect on the PST is discussed [68]. Specifically, the effect of the symmetry, position and type of the topological defect on the normal mode spectrum is investigated. It is shown, how these properties are influenced by external forces, such as anharmonic trapping potentials, axial micromotion [71–73], and differential light forces from the cooling laser. Whenever an external force breaks the intrinsic symmetry of the crystal in the sliding phase, the frequency of the soft mode becomes finite at the transition, even at  $T = 0$ .

The main result of P2 is the connection of the defect's type and position to the soft mode frequency at the expected transition point. Two possible extended defects can exist in an inhomogenous zigzag crystal, which are named the horizontal and vertical defect in P2. These two types show a different charge density per chain, as well as a different local structure. The soft mode near the PST in the unperturbed crystal exists only, if a horizontal defect is present. Interestingly, the two defect types can be locally changed into each other by applying a shear force to the two chains, that moves the defect. Then the two defects periodically transform into each other, and with this the existence of the soft mode periodically vanishes and reappears.

While the structural and normal mode properties of the PST in an ICC are mostly understood for the  $T = 0$  case, the frequency shift due to the finite temperature needs further investigation. Due to the probabilistic nature of the defect generation process and its sensitivity to temperature [60, 67, 68], the symmetry-breaking linear-to-zigzag transition (LZT) was chosen to investigate the finite-temperature spectrum at first. Besides the less complex experimental realization, the LZT in ICCs is well studied experimentally and analytically, see Refs. [56, 74–77]. Both the PST and the LZT are symmetry-breaking transitions with a soft mode at zero temperature and at least two ground states in the symmetry-broken regime [54, 74]. In both cases the barrier between the ground states is on the order of mK near the respective transition [54, 78].

In the third publication P3, the frequency shift of the soft mode of the LZT for finite temperatures is experimentally and theoretically investigated [78]. At this transition the symmetry along the crystal axis of a linear chain is broken, as can be seen by comparing Fig. 1.2 (a) and (c). The

soft mode that drives the transition is the zigzag mode, for which all ions oscillate transversely to the crystal axis, and each ion moves in the opposite direction of its neighbors, i.e., in a up-down-up-down pattern [77]. While the structural effects due to finite temperatures were investigated theoretically for ion crystals [79], and experimentally and numerically in macroscopic charged spheres [80–82], the temperature dependence of the soft-mode frequency was not studied extensively. In P3, a finite soft mode frequency at the transition is measured. In molecular dynamics simulations the increase in the frequency of the soft mode and jumps between the two ground states are observed. Both effects depend on the temperature, similar to the observations for the PST [54, 68]. The main result of P3 is an analytical model that assumes the crystal can still be considered in the linear, i.e., in the symmetric phase even if the trapping potentials indicate a zigzag crystal, as long as more than one jump between the two ground states occurs during the expected period of the soft mode. In this model the fourth-order interactions between the soft mode and higher-frequency modes lead to an average frequency shift of the soft mode, which reproduces the numerical and experimental results within the uncertainties.

The three publications contained in this cumulative thesis are added as individual chapters in their published format:

- P1: Probing nanofriction and Aubry-type signatures in a finite self-organized system
- P2: Nanofriction and motion of topological defects in self-organized ion Coulomb crystals
- P3: Finite-temperature spectrum at the symmetry-breaking linear to zigzag transition

At the beginning of each chapter a short statement of the author contributions and copyright are presented. Afterwards a summary of the combined results and an outlook on future research is given.

## 2 P1: Probing nanofriction and Aubry-type signatures in a finite self-organized system

**Authors:** J. Kiethe, R. Nigmatullin, D. Kalincev, T. Schmirander, and T. E. Mehlstäubler

**Journal:** Nature Communications

**DOI:** 10.1038/ncomms15364

**Author contributions:** The experiment was initiated and led by T.E.M. R.N. developed the numerical codes. R.N., J.K. and T.S. carried out the simulations. D.K. and J.K. designed the experiment with input from T.E.M. D.K. and J.K. carried out the experiments and performed the data analysis. All authors contributed to the discussion of results and participated in the manuscript preparation.

**Copyright:** © The Authors 2017. Published by Springer Nature. This article is licensed under a Creative Commons Attribution 4.0 International License.

ARTICLE

Received 22 Nov 2016 | Accepted 23 Mar 2017 | Published 15 May 2017

DOI: 10.1038/ncomms15364

OPEN

# Probing nanofriction and Aubry-type signatures in a finite self-organized system

J. Kiethe<sup>1</sup>, R. Nigmatullin<sup>2,3</sup>, D. Kalincev<sup>1</sup>, T. Schmirander<sup>1</sup> & T.E. Mehlstäubler<sup>1</sup>

Friction in ordered atomistic layers plays a central role in various nanoscale systems ranging from nanomachines to biological systems. It governs transport properties, wear and dissipation. Defects and incommensurate lattice constants markedly change these properties. Recently, experimental systems have become accessible to probe the dynamics of nanofriction. Here, we present a model system consisting of laser-cooled ions in which nanofriction and transport processes in self-organized systems with back action can be studied with atomic resolution. We show that in a system with local defects resulting in incommensurate layers, there is a transition from sticking to sliding with Aubry-type signatures. We demonstrate spectroscopic measurements of the soft vibrational mode driving this transition and a measurement of the order parameter. We show numerically that both exhibit critical scaling near the transition point. Our studies demonstrate a simple, well-controlled system in which friction in self-organized structures can be studied from classical- to quantum-regimes.

<sup>1</sup>Physikalisch-Technische Bundesanstalt, Bundesallee 100, 38116 Braunschweig, Germany. <sup>2</sup>Complex Systems Research Group, Faculty of Engineering and IT, The University of Sydney, Sydney, New South Wales 2006, Australia. <sup>3</sup>Department of Materials, University of Oxford, Parks Road, Oxford OX1 3PH, UK. Correspondence and requests for materials should be addressed to T.E.M. (email: tanja.mehlstaebler@ptb.de).

**D**ry friction is the resistance to the relative movement of two solid layers. It is responsible for many phenomena such as earthquakes, wear or crack propagation and is of enormous practical and technological impact<sup>1</sup>. According to Amontons and Coulomb, friction between solids is proportional to the normal force but independent of the contact areas. This intriguing result was explained by realizing that macroscopic objects touch at asperities that are deformed<sup>2</sup>. A different signature occurs when atomically flat surfaces slide against each other, as for example encountered in micro- or nanoelectromechanical systems or biological molecular motors<sup>1,3,4</sup>. At this nanoscale level the friction is no longer described by the Amontons-Coulomb law. For this, mathematical models were developed which are simple enough to be analysed analytically and yet should capture the salient features of the friction phenomena. As the sliding atomic layers are in contact with a thermal environment, dry friction phenomena are a problem of non-equilibrium statistical mechanics as well as nonlinear dynamics<sup>5</sup>.

One of the most successful models describing friction phenomena is the Frenkel-Kontorova (FK) model<sup>6</sup>. It consists of a chain of coupled particles sliding over a static periodic potential, which mimics a rigid undeformable substrate. The analysis of this model has revealed highly nontrivial, nonlinear dynamics such as the creation of kinks and anti-kinks, which facilitate the sliding. For an infinite system with incommensurate lattice periodicities, this model displays the celebrated Aubry transition<sup>7</sup>, where the sliding motion becomes frictionless, due to the competition of different interaction energies in the atomic many-body system. In solid-state systems, this superlubric regime has been demonstrated in nanocontacts of graphene and gold surfaces<sup>8–11</sup>. In finite systems a smooth-sliding regime with finite dissipation exists instead of the superlubric phase. An Aubry-type transition with a symmetry breaking signature occurs, when the system changes from the smooth-sliding to stick-slip regime<sup>12,13</sup>.

With the advent of atomic and friction force microscopes and microbalances it became possible to study individual sliding junctions at the atomistic level<sup>14–17</sup>. These techniques have identified many friction phenomena at the nanoscale, but many key aspects of friction dynamics are not yet well understood due to the lack of probes that characterize the contact surfaces directly and *in situ*<sup>1</sup>.

Laser-cooled and trapped ions have been proposed to emulate nanocontacts and to provide insights into the dynamics of friction processes<sup>18–20</sup>. In this scenario, the FK model is emulated by a chain of ions trapped in the harmonic potential of an ion trap, which is overlapped with an optical standing wave mimicking the corrugation potential. Signatures of an Aubry-type transition, that is, fragmentation and symmetry breaking of the periodic configuration of the ion chain, have been predicted, when the optical lattice depth increases above a critical value<sup>19</sup>. Another signature of the Aubry transition is the existence of a soft mode, that is, a vibrational mode whose frequency approaches zero at the critical point and drives the transition from pinned to sliding motion<sup>12</sup>. Such behaviour is also predicted for finite chains of ions in an external optical corrugation potential<sup>21</sup>.

Recently, Bylinskii *et al.*<sup>22</sup> succeeded in cooling up to five ions into an optical lattice and demonstrated the onset of reduced friction and dissipation in a coupled atomic many-body system. In this experiment, the symmetry breaking Aubry-type transition has been observed for the first time with microscopic resolution<sup>23</sup>, together with velocity effects in the stick-slip motion<sup>24</sup>. Another synthetic system, in which the microscopic processes of friction have become accessible, are colloidal monolayers driven across external optical potentials<sup>25</sup>. All these systems aim to emulate the

classical FK model, where a layer of interacting particles slides over a fixed rigid corrugation potential.

Here we report on the microscopic and spectroscopic control of a system without an externally imposed corrugation potential but consisting of two deformable back acting atomic layers, whose relative motion exhibits the phenomena of nanoscale friction. This system has similarities to a refined microscopic model of friction, which replaces the rigid substrate by a deformable substrate monolayer pinned to a solid body<sup>26</sup>. In particular, we investigate static friction under the influence of a structural defect and demonstrate physical properties of the system, which are common to finite incommensurate systems. We use a structural defect (kink) in an ion Coulomb crystal<sup>27</sup> to create a local disturbance in the ion spacing in the upper and lower chain, and demonstrate an Aubry-type transition when the interatomic spacing of the layers is varied. We show, using numerical calculations, that the soft mode frequency exhibits a power law scaling behaviour in the vicinity of the critical point, where the system becomes superlubric. The experimental spectroscopic measurements show a small reduction in the frequency of the soft mode. The non-vanishing frequency of the sliding mode is due to the finite temperature exciting nonlinear dynamics. In addition, the experimentally measured order parameter agrees with numerical results, which also exhibit a power law scaling in the vicinity of the critical point. Our system relates to solid-state phenomena such as charge density waves<sup>28</sup> and dislocations in crystals<sup>6</sup>. In particular, the scenario of two interacting, deformable atomic chains with back action is analogous to friction in fibrous composite materials<sup>29</sup>, sliding of DNA strands<sup>30</sup> and propagation of protein loops<sup>31</sup>. The manuscript is structured as follows: in the first section we introduce our experiment and model system. In the next section, we investigate the structural features of an Aubry-type transition—the symmetry breaking, the order parameter and the hull function. We then study the properties of the soft mode using spectroscopic measurements and numerical calculations. Finally, we discuss our results and prospects of our model system.

## Results

**Experimental system.** Our system consists of a two-dimensional ion Coulomb crystal in a linear rf trap<sup>32,33</sup>. Several tens of  $^{172}\text{Yb}^+$  ions are laser-cooled to temperatures around  $T \approx 1$  mK, so that they crystallize and self-organize into two ordered chains with interatomic distances of ca. 15 to 20  $\mu\text{m}$ , see Methods. The ions are fluoresced by near-resonant laser light and imaged onto an electron multiplying charged coupled device (CCD) camera providing single atom and photon detection, as graphically depicted in Fig. 1a. The axial harmonic confinement of the ion trap leads to an inhomogeneous ion spacing, in particular at the edges of the crystal, while the central part of large-enough crystals exhibits a slowly varying lattice spacing with interatomic distances  $a$  and  $b$  within one layer and in between the layers, respectively, see Fig. 1b.

In the following, we consider the one-dimensional axial motion of the two chains along the  $z$  axis in opposite directions. The friction dynamics depends on the relative interaction energies within each crystal row,  $U_{\text{intra}}$ , and between the rows,  $U_{\text{inter}}$ . To estimate the energy scales of these competing interaction strengths in our system, we relate them to the characteristic length and frequency scales in the Coulomb crystal. For this, it is convenient to view the system as two linear chains of identical particles of mass  $m$  which are joined by interatomic springs of stiffness  $\kappa$ , depending on the inter-ion distance  $a$ . The masses are attached to a rigid support by external springs of stiffness  $D = m \omega_{\text{ax}}^2$  due to the elastic confinement in the ion trap along the

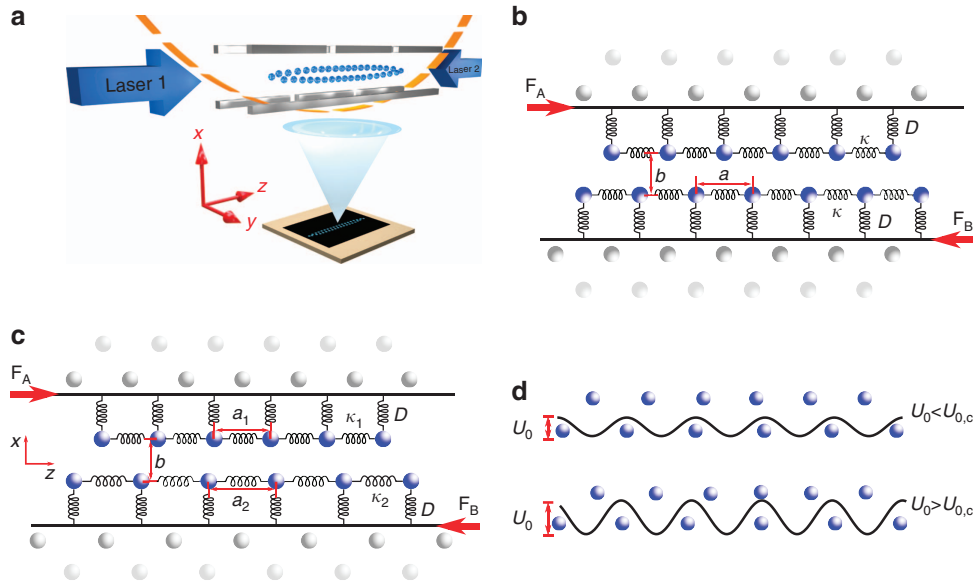


**Figure 1 | Experimental set-up and model system.** (a) Schematic of the experimental set-up. Several tens of ions are trapped inside a linear rf trap. An rf amplitude of around 1,000 V at the four quadrupole electrodes creates a time averaged confining potential in radial direction. The harmonic axial confinement is created via different dc voltages on the segmented electrodes, indicated by the orange dashed line. Typical radial and axial trapping frequencies are  $\omega_{\text{rad}} \approx 2\pi 140$  kHz and  $\omega_{\text{ax}} \approx 2\pi 25$  kHz, leading to inter-ion distances of  $a \approx 20$   $\mu\text{m}$  and  $b \approx 15$   $\mu\text{m}$ . The ions are illuminated with laser 1. Vibrational mode spectroscopy is performed with laser 2. The fluorescence of the ions is imaged onto an electron multiplying CCD camera. (b) The central part of the Coulomb crystal can be pictured as a self-organized interface between two solids. For the axial movement of the two atomic layers we consider the following model. Each chain is connected to the substrate via springs. The next-neighbour interaction between particles in the same row is modelled as spring forces. The deformability leads to identical intra chain spacing  $a$  in upper and low layer. The chains can move relative against each other, using differential laser light forces. (c) A structural defect inside the Coulomb crystal locally breaks the periodicity of the two chains, resulting in different particle distances  $a_1$  and  $a_2$  in the chains. (d) The Coulomb potential of one row of ions acts as the corrugation potential for the other row. The depth of the corrugation  $U_0$  determines the dynamics of the system. Below a critical corrugation depth  $U_0 < U_{0,c}$  the system displays horizontal mirror symmetry. Above the critical value  $U_0 > U_{0,c}$  the symmetry is broken.

axial direction. Here  $\omega_{\text{ax}}/2\pi$  is the frequency of the centre of mass mode along the  $z$  axis. In this setting, the two chains of ions can be moved and distorted by optical forces or light pressure as indicated with  $F_A$  and  $F_B$  in Fig. 1b,c.

For the case of periodically ordered chains as shown in Fig. 1b, stick-slip motion of the two layers of ions with respect to each other is expected to be approximated by the classical Prandtl–Tomlinson model<sup>34</sup>, where a single particle has to overcome the potential energy barriers created by the periodic atomic lattice below. However, when a structural defect is present, the local disturbance in the periodicity of upper and lower chain leads to the nonlinear many-body phenomenon of reduced friction<sup>6,7</sup>. The underlying reason is that atoms in one layer will now locally sense different corrugation potential energies, which then can be stored by the internal springs described by  $\kappa$ . To investigate friction in soft chains of atomically flat layers under the presence of a defect, we create a stable structural defect in the centre of the Coulomb crystal, see Methods. This causes slightly different interatomic distances  $a_1$  and  $a_2$  in the central part of the Coulomb crystal, see Fig. 1c.

A rough estimate of the interaction energy between two ions inside one layer is  $U_{\text{intra}} = \frac{1}{2}\kappa z^2$ . The corrugation potential pinning ions of one chain with respect to the other chain can be locally approximated as  $U_{\text{inter}} = \frac{1}{2}U_0(\cos[\frac{2\pi}{a}z] + 1)$ , as indicated in Fig. 1d. Depending on whether the interaction inside an atomic layer or between the layers is larger, a transition from the sliding to the pinned regime at a critical depth of the corrugation potential  $U_{0,c}$  is expected. The interaction dynamics between the two atomic layers is thus governed by two competing energies. In harmonic approximation, they can be expressed in

terms of frequencies  $\omega_{\text{pinning}} = \sqrt{\frac{U_0 2\pi^2}{m a^2}}$  and  $\omega_{\text{natural}} = \sqrt{\frac{\kappa}{m}}$ , defining the corrugation parameter  $\eta = \frac{\omega_{\text{pinning}}^2}{\omega_{\text{natural}}^2}$ .

To estimate the ratio of the competing energy scales, we have numerically calculated  $\omega_{\text{pinning}}$  and  $\omega_{\text{natural}}$  for the central ions in the zigzag configuration, see Supplementary Note 1 and Supplementary Fig. 1. While  $\omega_{\text{pinning}}$  depends on both interatomic distances  $a$  and  $b$ , the natural frequency of an ion inside a layer can be expressed as  $\omega_{\text{natural}} \sim \sqrt{\frac{e^2}{\pi\epsilon_0 m a^3}}$ , when considering only next-neighbour interaction. As we vary the relative interatomic distances  $a$  and  $b$ , and with this the strength of the interaction potentials, we expect to observe a pinned to sliding transition. Experimentally this can be achieved by varying the ratio  $\alpha = \omega_{\text{rad}}/\omega_{\text{ax}}$  of radial and axial trapping frequencies, that is, the aspect ratio of radial and axial confinement in the ion trap.  $\alpha$  is used as the control parameter in our experiment to cross the transition at the critical point  $\alpha_c$ . For the numerical calculations we also plot  $\eta$ , which scales linearly with  $\alpha$  close to the transition, see Supplementary Fig. 2.

**Symmetry breaking transition.** A general signature of Aubry and Aubry-type transitions, in both infinite and finite systems, is the breaking of analyticity<sup>7</sup>. This refers to the description of the sliding system in terms of a hull function, which parameterizes all possible configurations of the ground state under the presence of a sliding force. This function becomes non-analytic when the Aubry transition is crossed. In our system, as the two ion chains are brought closer together the corrugation depth increases and



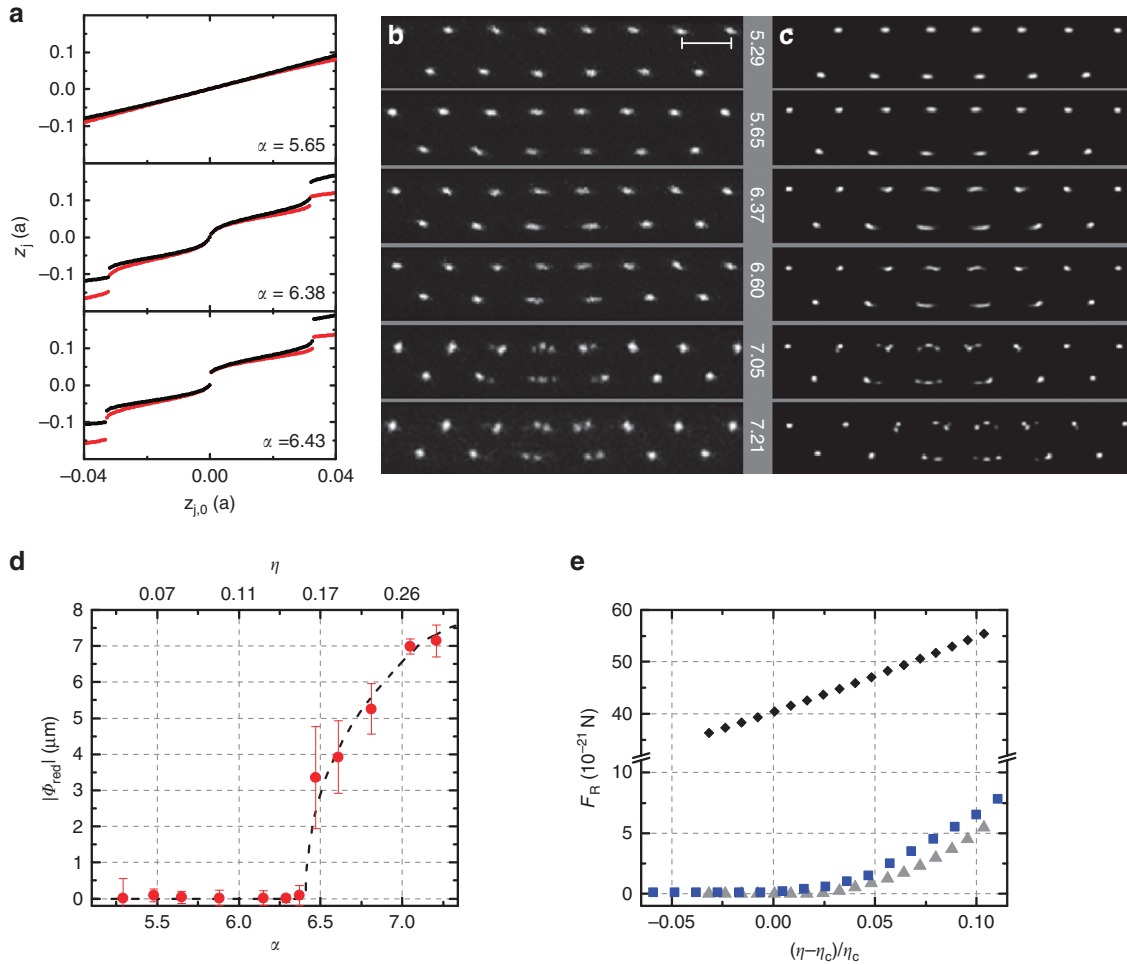


**Figure 2 | Symmetry breaking of the crystal and restoring force.** (a) Numerically calculated hull functions in units of the lattice constant  $a$  for the two central ions, left (red points) and right (black points) to the crystal centre. Below  $\alpha_c = 6.41$  the hull functions are continuous. After the pinning transition is crossed they exhibit a central gap. Slightly below  $\alpha_c$  secondary gaps are observed. The inhomogeneity of the crystal leads to a lower charge density, and thus lower  $\omega_{\text{natural}}$ , further away from the crystal centre. If the defect is not at the centre, the pinning transition occurs for  $\alpha < \alpha_c$ . The secondary gaps of the central ions are the response to the analyticity breaking of the outer ions' hull functions. (b) Photos of experimentally observed 30-ion crystal configurations at different aspect ratios  $\alpha = \frac{\omega_{\text{red}}}{\omega_{\text{ox}}}$  from 5.29 to 7.21, as indicated in the grey bar. Relative errors are less than 1%. The exposure time is 700 ms. Laser 1 continuously cools the ions. No force is applied. The blurring of the ion positions near the sliding transition and the appearance of multiple configurations above it are due to thermal excitations. The scale bar is  $16.5 \mu\text{m}$ . (c) Numerically simulated 30-ion crystal configurations at  $T = 1 \text{ mK}$  integrated over 10 ms of time evolution. (d) The absolute value of the order parameter  $|\Phi_{\text{red}}|$  for 30 ions plotted against  $\alpha$  and  $\eta$ . Experimental data (red circles) are shown in comparison to numerically obtained values for  $T = 0 \text{ K}$  (black dashed line). Experimental values represent a weighted average over 5–26 measurements, with exception of  $\alpha = 7.21$ , where only 2 configurations were observed. Error bars are one standard deviation weighted by fit errors. (e) Numerically calculated restoring force  $F_R$  plotted against  $(\eta - \eta_c)/\eta_c$  for an inhomogeneous crystal (blue squares), a homogeneous crystal (grey triangles) and an ideal zigzag without defect (black diamonds).  $\eta$  refers to the inhomogeneous case. The parameters for the homogeneous and commensurate crystals were chosen to have an identical ratio of inner inter-ion distances  $a, b$ . The friction force needed in the ideal crystal slightly above the pinning transition is roughly an order of magnitude bigger.

eventually reaches a critical point. Above this point the corrugation prevents the ions from assuming all positions during sliding and their trajectories, and thus the hull function, become discontinuous. This is the point where Peierls–Nabarro (PN) barriers are formed<sup>6</sup>.

To study the analyticity breaking in our system, we first conduct numerical simulations of a 30-ion crystal under the presence of differential forces applied to upper and lower ion chain. In the classical FK model, the hull function  $z_j(z_{j,0})$  is defined as the coordinate of a particle  $j$  under the influence of a static corrugation potential in relation to its unperturbed coordinate  $z_{j,0}$  without the underlying lattice. For the self-organized system of two interacting atomic chains, the corrugation potential is given by the Coulomb potential of

the 2nd row of ions and thus cannot be switched off. To calculate the hull function in such a system, we first apply opposite forces  $\pm F/2$  to each row of the crystal to obtain  $z_j$ . Then we apply the force  $F$  to both rows in the same direction, moving the lattice along with the ion to obtain  $z_{j,0}$ , that is, the equilibrium position of the ions in the harmonic trapping potential without any influence of the underlying lattice. We implement this principle in our numerical simulations and show the result in Fig. 2a. A more detailed evolution of the hull function can be found in the Supplementary Movie 1. For the same control parameter  $\alpha$ , where a primary gap opens up in the hull function at  $z_{j,0} = 0$ , we observe a structural symmetry break in the equilibrium positions of the crystal configuration. This is visible in Fig. 2b, which shows photos of experimental realizations of 30-ion crystals at

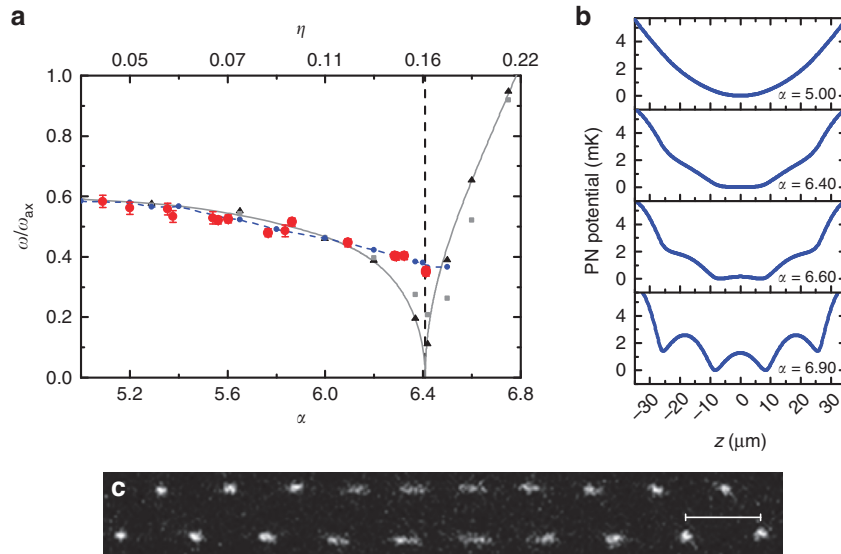


**Figure 3 | Vibrational soft mode and PN barriers.** (a) Frequency of the soft mode in a 30-ion crystal. The experimental data is shown in red circles and the error bars are given by uncertainties of the measured soft mode and common mode frequencies. The solid line displays the numerically calculated dispersion relation at  $T=0 \text{ K}$ . Frequencies extracted via a Fourier transformation from molecular dynamics simulation are given by black triangles at  $T=5 \mu\text{K}$ , grey squares at  $T=50 \mu\text{K}$  and blue circles at  $T=1 \text{ mK}$ . The dashed blue line acts as a guide for the eye. All frequencies are plotted in units of the axial secular frequency  $\omega_{ax}=2\pi(25.6 \pm 0.2) \text{ kHz}$ . The pinning transition is marked with a vertical line. (b) Numerically calculated PN potentials showing the onset of barriers above  $\alpha_c$ . At temperatures of  $T=1 \text{ mK}$  the thermal fluctuations sample the multiple minima of the PN potential and consequently no harmonic motion with a single distinct frequency can exist for  $\alpha > \alpha_c$ . (c) A CCD image of an ion Coulomb crystal in our experiment in which the localized vibrational mode is resonantly excited by a focused laser beam. It is taken at  $\alpha=5.77$  with an exposure time of 100 ms and 300  $\mu\text{W}$  of power in the cooling laser. The focused laser beam is modulated between 0 and 35  $\mu\text{W}$  with a frequency of  $12.1 \pm 0.3 \text{ kHz}$ . Scale bar, 20.5  $\mu\text{m}$ .

different  $\alpha$ . They are compared to images obtained from numerical simulations at  $T=1 \text{ mK}$ , shown in Fig. 2c. In both the experiment and the simulations no driving force is applied to the crystals. The motional excitation of the ions is due to the finite temperature.

The collective dynamics in a discrete nonlinear system is typically described by the PN potential<sup>6</sup>. It corresponds to the energy needed to move the charge density. For temperatures close to  $T=0 \text{ K}$  the system would choose one stable configuration in one of the minima of the PN potential, shown in Fig. 3b. For finite temperatures close to the height of the PN barriers, the different choices of the system become visible. In Fig. 2b,c for  $\alpha < \alpha_c$  the crystal shows horizontal mirror symmetry around its centre. As  $\alpha$  approaches  $\alpha_c$  the thermal oscillation amplitude of the inner ions becomes larger, indicating that the ions are less pinned close to criticality. At  $\alpha_c=6.41$  the pinning transition is crossed. At this point the PN potential develops multiple minima, as can be seen in Fig. 3b at  $\alpha > 6.4$ , causing the symmetry breaking of the crystal. A high-resolution video of the emergence of PN barriers is provided in the Supplementary Movie 2. Slightly above  $\alpha_c$  we do not resolve the symmetry broken configuration, as thermal fluctuations mask the local minima. However, a larger spread in the central ion positions is observed. As  $\alpha$  is increased over 7.00, multiple stable crystal configurations become visible, indicating the existence of multiple minima in the PN potentials.

From the crystal configurations we can extract a structural order parameter that quantifies the symmetry breaking at the transition from pinned to sliding. For our scenario, that is, the sliding of two deformable chains, we choose to define an order parameter  $\Phi$  as the relative axial distance between ions of different layers, in the following labelled Chain A and B. It characterizes the horizontal mirror symmetry of the system,

$$\Phi = \sum_{i \in \text{Chain A}} \text{sgn}(z_i) \cdot \min_{j \in \text{Chain B}} |z_i - z_j|, \quad (1)$$

where  $z_i$  is the axial coordinate of the ion  $i$  and  $z=0$  is the axial symmetry axis below the transition point. In the sliding regime  $\Phi=0$ . Crystal configurations obtained from numerical simulations at  $T=0 \text{ K}$ , show that at the critical point around  $\alpha_c \approx 6.41$ , the order parameter shows a cusp where the system chooses a state of broken symmetry, a typical signature of a second-order phase transition, see dashed line in Fig. 2d. When evaluating the experimental data, to reduce the accumulated error of fitted ion positions and to avoid errors due to aberrations of our imaging system at large distances from the optical axis, we measure and plot a reduced version  $\Phi_{\text{red}} = \Phi_{i=N/2} + \Phi_{i=N/2+1}$ , which includes only the central terms with the largest contribution to the overall sum. The experimental data in Fig. 2d (red circles) are extracted from CCD images, some of which are shown in Fig. 2b. The experimentally and numerically observed critical corrugation parameter  $\eta_c \approx 0.16$  is smaller than 1, because for simplicity the interaction energies were calculated only for the zigzag. The difference between the interatomic distances  $a$  and  $a_{1,2}$  explain the smaller critical corrugation parameter.

At last, following Benassi *et al.*<sup>19</sup> and using the data from numerical simulations, we calculate the restoring force  $F_R$ , which is needed to restore symmetry in our system, above the transition point.  $F_R$  can be identified with the static friction force  $F_S$  in an infinite and thus homogeneous chain.  $F_S$  is needed to overcome the PN barriers and translate the localized defect by one lattice site. In Fig. 2e,  $F_R$  is shown for a homogeneous and inhomogeneous crystal with defect, as well as an ideal zigzag. The restoring forces are similar, indicating that our model system, consisting of finite and inhomogeneous Coulomb crystals, is a good approximation to large scale systems, with homogeneous particle spacing. Comparing the axial inter-ion distances near the defect, we find that distances between the innermost ions differ by less than 1%. For next-neighbour ions the difference increases to a few per cent. Compared to the force  $F_S \approx 5 \times 10^{-20} \text{ N}$  needed to move two perfectly matched chains (a zigzag configuration

without defect) against each other, the static friction force is reduced by more than an order of magnitude slightly above the pinning transition. The derivation of  $F_S$  for the scenario of unperturbed crystals, analogous to the Prandtl–Tomlinson model, is detailed in the Supplementary Note 2.

**Soft mode and critical scaling.** The sliding of two atomic chains is driven by the vibrational axial shear mode of the crystal, where the two rows move in opposite directions. Its frequency being zero signifies it costs no energy to translate the layers relative to one another. For finite systems, the frequency of the lowest vibrational mode approaches zero but remains finite both above and below the pinning transition and thus the system is only superlubric at the critical point<sup>12</sup>. In an ideal zigzag however no such soft mode exists, as the system is commensurate. Only when a structural defect is present in the lattice disturbing the regular ordering of particles a soft mode is present. It is localized at the position of the defect<sup>35</sup> and kink dynamics governs the sliding of the two atomic layers.

We first calculate the dispersion relation of the vibrational modes in our two-dimensional ion Coulomb crystal for different interatomic distances  $b$  between the layers, see Methods. The solid grey line in Fig. 3a shows the dependence of the localized soft mode on the control parameter  $\alpha$  and the corrugation parameter  $\eta$ . For  $\alpha < 6.8$  this mode is the lowest frequency mode in the crystal. Its frequency reaches zero at the transition point, indicated by a vertical dashed line, and assumes finite values in the sliding regime. In the experiment we use differential laser light forces to resonantly excite the vibrational modes of the ion Coulomb crystal by sinusoidal intensity modulation. An experimental photo in which the soft mode is excited is shown in Fig. 3c. Further details are found in the Methods. The measurement results are depicted as red circles in Fig. 3a. Below the sliding-to-pinning transition, our measurements agree with the calculated frequencies of the dispersion relation. Close to the transition the experimental measurements deviate from theory. Above the critical point no excitation of the soft mode was possible. To understand this behaviour, we conducted molecular dynamics simulations of the unperturbed crystal, that is without laser excitation, at finite temperatures (for details see Methods). From the ion trajectories the vibrational spectrum of the crystal was extracted using a Fourier transformation. To benchmark our analysis, we first perform simulations at  $T = 5 \mu\text{K}$  and find the results to be in good agreement with our calculations. At an increased temperature of  $T = 50 \mu\text{K}$  the Fourier spectrum of the ion vibrations deviates from the dispersion relation. For  $T = 1 \text{ mK}$  and  $\alpha > \alpha_c$  we observe a broad range of frequencies in the Fourier

transform with no clear resonance. For  $\alpha < \alpha_c$  the soft mode frequencies extracted from these simulations agree with the experimentally observed resonances. We attribute the deviation of the observed frequencies near the transition point to the increasing contribution of the nonlinearities of the PN potential, which is shown in Fig. 3b. Above the symmetry breaking transition the thermal amplitude of the kink motion overcomes the barriers between potential minima, and no single distinct mode frequency exists. For consistency, we compare the experimentally observed thermal amplitudes of the central ions to numerical simulations similar to Fig. 2b. From this we obtain an estimate for the temperature of the crystal, which is found to be  $T = 0.5 \pm 0.4 \text{ mK}$ .

The finite size of ion Coulomb crystals in a harmonic trap and thus the inhomogeneous charge density results in a global curvature of the PN potential, as can be seen in Fig. 3b. This is in stark contrast to the vanishing PN potential for infinite systems below criticality. Not only is the crystal finite, but we expect the sliding dynamics to be governed by the local distortion of the structural defect. To discern whether critical scaling exists in this system, we numerically calculate the soft mode frequency and the order parameter in the vicinity of the sliding-to-pinning transition with high resolution. Results for different crystal sizes are shown in Fig. 4. We fit the order parameter as  $\Phi \propto (\eta - \eta_c)^\sigma$  and the soft mode frequencies above and below critical point as  $\omega^\pm \propto (\eta - \eta_c)^{\chi^\pm}$ . We find that independent of the ion number and the crystal size  $\sigma \approx \chi^\pm \approx 0.5$ , similar to what has been observed for an Aubry-type transition in finite systems<sup>12</sup>. In the Supplementary Fig. 3 we show a linear presentation of the soft mode for 30 and 60 ions.

## Discussion

In this work, we use an ion Coulomb crystal with a structural defect to experimentally and numerically study static friction in a self-organized system. In the scenario emulated by our model system two deformable chains slide on top of each other. Such situations frequently arise in nature, in particular in biomolecules<sup>30,31</sup>. We experimentally observe the symmetry breaking at the sliding-to-pinning transition and we spectroscopically resolve the frequency of the localized vibrational mode, which is responsible for charge transport in our system. The strength of trapped and laser-cooled ions is that they are a readily accessible model system, in which many-body physics can be observed with single atom resolution. With high quality imaging optics, a spatial resolution of a few nm can be achieved<sup>136</sup>. Single atom resolution also allows studies of kinetic friction<sup>20,37</sup> and the spectroscopic access to internal degrees of freedom enables

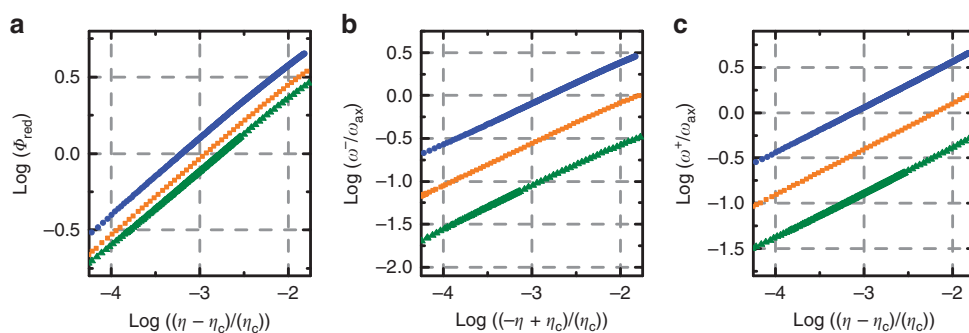


**Figure 4 | Critical scaling.** All graphs show numerical results. **(a)** Double logarithmic plot of the order parameter for  $N = 30$  (blue points),  $60$  (orange points) and  $90$  (green points) ions. The fitted critical exponents are  $\sigma_{30} = 0.50$ ,  $\sigma_{60} = 0.50$  and  $\sigma_{90} = 0.49$ . **(b)** Double logarithmic plot of the soft mode frequency for  $\eta < \eta_c$ . The colour code is identical. The plots for  $N = 30$  and  $60$  are shifted by  $1$  and  $1/2$  for clarity. Fitted critical exponents are  $\chi_{30}^- = 0.486$ ,  $\chi_{60}^- = 0.491$  and  $\chi_{90}^- = 0.504$ . **(c)** Double logarithmic plot of the soft mode frequency for  $\eta > \eta_c$ . The same offsets apply. The fitted critical exponents are  $\chi_{30}^+ = 0.498$ ,  $\chi_{60}^+ = 0.501$  and  $\chi_{90}^+ = 0.490$ .

investigations of non-equilibrium dynamics and transport processes with ns and  $\mu\text{s}$  time resolution<sup>38</sup>. Typically, trapped ions are confined in harmonic potentials which lead to an inhomogeneous ion spacing. Our results show that the inhomogeneity due to the boundary conditions and the system size influence our model system only slightly. This is due to the fact, that we focus on the phenomena of the onset of sliding, which is dictated by the localized lattice defect. However, given the controllability of Coulomb crystals it is possible to extend our model to versatile geometries, e.g., equally spaced crystals in anharmonic potentials or ring traps<sup>39</sup>. Moreover, the ideas presented in this work may be used to investigate the currently poorly understood Aubry transition in two-dimensional systems<sup>40</sup>, since ion traps can trap large three-dimensional Coulomb crystals composed of regular two-dimensional layers<sup>41</sup>. Furthermore, by investigating the soft mode of the sticking to sliding transition, we demonstrate the spectroscopic observation of the highly nonlinear vibrational mode of the structural defect. These localized modes have also been proposed for the implementation of quantum information protocols<sup>35</sup>. Recently, the high energy gap mode and its coupling to the low frequency mode of the localized defect were observed (T. Schaetz, personal communication).

In the future, the experiments can be improved by further cooling to the  $\mu\text{K}$  regime using narrow transitions<sup>32</sup> or dark resonances<sup>42,43</sup>, making quantum effects of friction accessible. This can provide a new platform for studying the physics of Wigner crystals<sup>18,44</sup>.

## Methods

**Coulomb crystals and structural defect creation.** Coulomb crystals form, when ions are cooled to kinetic energies lower than the potential energy of the Coulomb system. This is achieved by laser cooling the  $^{172}\text{Yb}^+$  ions on the broad, dipole allowed atomic transition  $^2S_{1/2}$  to  $^2P_{1/2}$  at 370 nm with a natural linewidth of  $\gamma = 20$  MHz. The frequency of the cooling laser is detuned from resonance by  $\delta = -\gamma/2$  resulting in a crystal temperature close to the Doppler cooling limit of  $T = 0.5$  mK. The cooling laser illuminates the ions with a power between 200 and 300  $\mu\text{W}$ . The waist is 2.56 mm in axial direction and 80  $\mu\text{m}$  in radial direction. One to three-dimensional crystal configurations can be chosen, depending on the relative strength of the harmonic trapping potentials  $U(r) = \frac{1}{2}\omega_{\text{rad}}^2 mr^2$  in radial direction and  $U(z) = \frac{1}{2}\omega_{\text{ax}}^2 mz^2$  in axial direction<sup>45,46</sup>, where  $m$  is the ion mass and  $r = \sqrt{x^2 + y^2}$ . When the structural transition from the linear chain to the two-dimensional zigzag is crossed non-adiabatically, defects can be created<sup>27,47–49</sup>. In our experiment, we create and stabilize a structural defect in the centre of the Coulomb crystal by fast ramps of the radially confining rf potential<sup>27</sup>. Typical radial and axial trapping frequencies are  $\omega_{\text{rad},x} \approx 2\pi 140$  kHz and  $\omega_{\text{ax}} \approx 2\pi 25$  kHz, leading to inter-ion distances of  $a \approx 20$   $\mu\text{m}$  and  $b \approx 15$   $\mu\text{m}$ . The anisotropy of the radial confinement with  $\frac{\omega_{\text{rad},x}}{\omega_{\text{rad},y}} \approx 1.3$  creates a two-dimensional setting for the frictional dynamics. The trap frequencies are typically determined within 100 Hz, amounting to an error of  $\pm 0.02$  in the control parameter  $\alpha = \frac{\omega_{\text{rad}}}{\omega_{\text{ax}}}$ . The ions are imaged onto an electron multiplying CCD camera using a self-built detection lens with an  $NA = 0.2$  and a magnification of 24. In a regular zigzag configuration, we can resolve the ion positions within 40 nm at exposure times of 700 ms by fitting a Gaussian profile to the images. The resolution is limited by the magnification of our imaging system and the pixel size of the CCD chip. Fitting multiple ion positions in the symmetry broken regime runs into a limit close to the transition where the intensity maxima are separated by less than a pixel.

**Spectroscopy.** For the spectroscopy of the vibrational modes, we use a second laser beam under an angle of  $25^\circ$  to the crystal axis, which is focused to a waist of ca. 80  $\mu\text{m}$ . The laser is amplitude modulated with a frequency  $\nu$ , exerting a periodically oscillating force  $F = F_0 \cos[2\pi \cdot \nu t]$  onto the ions. To efficiently excite the shear mode, we centre the laser beam axially and slightly misalign it along the radial direction to obtain a differential light force in axial direction between the two chains. If  $\nu$  is near-resonant with a vibrational mode, a broadening of the ion positions is observed. To determine the resonance, we sweep  $\nu$  with a speed between 1 and 2 kHz  $\text{s}^{-1}$ . The full-width at half maximum of the resonances is about 1 kHz and its centre frequency is determined within 300–400 Hz.

**Numerical simulations.** For simulations with  $T = 0$  K, we determine the dispersion relation by diagonalising the Hessian matrix  $H_{ij} = \left. \frac{\partial^2 V}{\partial q_i \partial q_j} \right|_{\mathbf{q}(0)}$ , where  $V$  is the

potential energy;  $q_i$  are the degrees of freedom with  $i$  ranging from 1 to  $2N$ , with  $N$  being the number of ions;  $\mathbf{q}(0)$  represents the equilibrium configuration. The eigenvectors  $H_{ij}$  are the vibrational normal modes and the corresponding eigenvalues are squares of the normal frequencies. The equilibrium positions  $\mathbf{q}(0)$  are found by solving the equations of motions numerically using gradient descent methods. For the calculation of the hull function and the restoring force  $F_R$  we use the same method, but add axial differential forces between the two chains to the equations of motion.

For simulations at non-zero temperature we are solving the Langevin equation, which includes the harmonic motion of the ions in a ponderomotive trapping potential under the presence of a stochastic force  $\varepsilon(t)$ . The fluctuation-dissipation relation  $\langle \varepsilon_{\alpha j}(t) \varepsilon_{\beta i}(t') \rangle = 2\eta k_B T \delta_{\alpha\beta} \delta_{ij} \delta(t-t')$ , with  $\alpha, \beta = x, y, z$  and  $\eta$  the friction coefficient, connects the stochastic force to the temperature  $T$  of the system<sup>27</sup>.

The PN potential is calculated by finding the adiabatic trajectory of the defect and extracting the potential energy. Finding the trajectory is an optimization problem, which is solved using the method of Lagrange multipliers<sup>50</sup>.

**Data availability.** The data that support the findings of this study are available from the corresponding author upon reasonable request.

## References

- Vanossi, A., Manini, N., Urbakh, M., Zapperi, S. & Tosatti, E. Colloquium: Modeling friction: From nanoscale to mesoscale. *Rev. Mod. Phys.* **85**, 529 (2013).
- Bowden, F. P. & Tabor, D. *The Friction and Lubrication of Solids* (Oxford Univ. Press, 1950).
- Mo, Y., Turner, K. T. & Szlufarska, I. Friction laws at the nanoscale. *Nature* **457**, 1116–1119 (2009).
- Bormuth, V., Varga, V., Howard, J. & Schäffer, E. Protein friction limits diffusive and directed movements of kinesin motors on microtubules. *Science* **325**, 870–873 (2009).
- Seifert, U. Stochastic thermodynamics, fluctuation theorems and molecular machines. *Rep. Prog. Phys.* **75**, 126001 (2012).
- Braun, O. M. & Kivshar, Y. *The Frenkel-Kontorova Model: Concepts, Methods, and Applications* (Springer Science & Business Media, 2013).
- Aubry, S. The twist map, the extended Frenkel-Kontorova model and the devil's staircase. *Phys. D* **7**, 240–258 (1983).
- Lancon, F. *et al.* Superlubricity at an Internal Incommensurate Boundary. *Nano Lett.* **10**, 695–700 (2010).
- Dienwiebel, M. *et al.* Superlubricity of graphite. *Phys. Rev. Lett.* **92**, 126101 (2004).
- Hirano, M., Shinjo, K., Kaneko, R. & Murata, Y. Observation of Superlubricity by Scanning Tunneling Microscopy. *Phys. Rev. Lett.* **78**, 1448 (1997).
- Kawai, S. *et al.* Superlubricity of graphene nanoribbons on gold surfaces. *Science* **351**, 957–961 (2016).
- Braiman, Y., Baumgarten, J., Jortner, J. & Klafter, J. Symmetry-breaking transition in finite Frenkel-Kontorova chains. *Phys. Rev. Lett.* **65**, 2398 (1990).
- Sharma, S. R., Bergersen, B. & Joos, B. Aubry transition in a finite modulated chain. *Phys. Rev. B* **29**, 6335 (1984).
- Carpick, R. W. & Salmeron, M. Scratching the Surface: Fundamental Investigations of Tribology with Atomic Force Microscopy. *Chem. Rev.* **97**, 1163–1194 (1997).
- Urbakh, M. & Meyer, E. Nanotribology: The renaissance of friction. *Nat. Mater.* **9**, 8–10 (2010).
- Socoliuc, A., Bennowitz, R., Gnecco, E. & Meyer, E. Transition from Stick-Slip to Continuous Sliding in Atomic Friction: Entering a New Regime of Ultralow Friction. *Phys. Rev. Lett.* **92**, 134301 (2004).
- Pierno, M. *et al.* Frictional transition from superlubric islands to pinned monolayers. *Nat. Nanotechnol.* **10**, 714–718 (2015).
- García-Mata, I., Zhurov, O. V. & Shepelyansky, D. L. Frenkel-Kontorova model with cold trapped ions. *Eur. Phys. J. D* **41**, 325–330 (2007).
- Benassi, A., Vanossi, A. & Tosatti, E. Nanofriction in cold ion traps. *Nat. Commun.* **2**, 236 (2011).
- Mandelli, A., Vanossi, A. & Tosatti, E. Stick-slip nanofriction in trapped cold ion chains. *Phys. Rev. B* **87**, 195418 (2013).
- Pruttivarasin, T., Ramm, M., Talukdar, I., Kreuter, A. & Häffner, H. Trapped ions in optical lattices for probing oscillator chain models. *New J. Phys.* **13**, 075012 (2011).
- Bylinskii, A., Gangloff, D. & Vuletić, V. Tuning friction atom-by-atom in an ion-crystal simulator. *Science* **348**, 1115–1118 (2015).
- Bylinskii, A., Gangloff, D., Counts, I. & Vuletić, V. Observation of Aubry-type transition in finite atom chains via friction. *Nat. Mater.* **15**, 717–721 (2016).
- Gangloff, D., Bylinskii, A., Counts, I., Jhe, W. & Vuletić, V. Velocity tuning of friction with two trapped atoms. *Nat. Phys.* **11**, 915–919 (2015).
- Bohle, T., Mikhael, J. & Bechinger, C. Observation of kinks and antikinks in colloidal monolayers driven across ordered surfaces. *Nat. Mater.* **11**, 126–130 (2011).
- Matsukawa, H. & Fukuyama, H. Theoretical study of friction: One-dimensional clean surfaces. *Phys. Rev. B* **49**, 17286 (1994).

27. Pyka, K. *et al.* Topological defect formation and spontaneous symmetry breaking in ion Coulomb crystals. *Nat. Commun.* **4**, 2291 (2013).
28. Monceau, P. Electronic crystals: an experimental overview. *Adv. Phys.* **61**, 325–581 (2012).
29. Ward, A. *et al.* Solid friction between soft filaments. *Nat. Mater.* **14**, 583–588 (2015).
30. Kumar, S. & Li, M. S. Biomolecules under mechanical force. *Phys. Rep.* **486**, 1–74 (2010).
31. Sieradzan, A. K., Niemi, A. & Peng, X. Peierls-Nabarro barrier and protein loop propagation. *Phys. Rev. E* **90**, 062717 (2014).
32. Pyka, K., Herschbach, N., Keller, J. & Mehlstäubler, T. E. A high-precision segmented Paul trap with minimized micromotion for an optical multiple-ion clock. *Appl. Phys. B* **114**, 231–241 (2014).
33. Partner, H. L. *et al.* Structural phase transitions and topological defects in ion Coulomb crystals. *Physica B* **460**, 114–118 (2015).
34. Prandtl, L. Ein Gedankenmodell zur kinetischen Theorie der festen Körper. *Z. Angew. Math. Mech.* **8**, 85–106 (1928).
35. Landa, H., Marcovitch, S., Retzker, A., Plenio, M. B. & Reznik, B. Quantum Coherence of Discrete Kink Solitons in Ion Traps. *Phys. Rev. Lett.* **104**, 043004 (2010).
36. Wong-Campos, J. D., Johnson, K. G., Neyenhuis, B., Mizrahi, J. & Monroe, C. High-resolution adaptive imaging of a single atom. *Nat. Photonics* **10**, 606–610 (2016).
37. Vanossi, A., Manini, N. & Tosatti, E. Static and dynamic friction in sliding colloidal monolayers. *Proc. Natl Acad. Sci. USA* **109**, 16429–16433 (2012).
38. Roßnagel, J., Tolazzi, K. N., Schmidt-Kaler, F. & Singer, K. Fast thermometry for trapped ions using dark resonances. *New J. Phys.* **17**, 045004 (2015).
39. Li, H.-K. *et al.* Realization of translational symmetry in trapped cold ion rings. *Phys. Rev. Lett.* **118**, 053001 (2017).
40. Mandelli, D. *et al.* Superlubric-pinned transition in sliding incommensurate colloidal monolayers. *Phys. Rev. B* **92**, 134306 (2015).
41. Mitchell, T. B. *et al.* Direct observations of structural phase transitions in planar crystallized ion plasmas. *Science* **282**, 1290–1293 (1998).
42. Morigi, G., Eschner, J. & Keitel, C. H. Ground state laser cooling using electromagnetically induced transparency. *Phys. Rev. Lett.* **85**, 4458 (2000).
43. Lechner, R. *et al.* Electromagnetically-induced-transparency ground-state cooling of long ion strings. *Phys. Rev. A* **93**, 053401 (2016).
44. Meyer, J. S., Matveev, K. A. & Larkin, A. I. Transition from a one-dimensional to a quasi-one-dimensional state in interacting quantum wires. *Phys. Rev. Lett.* **98**, 126404 (2007).
45. Thompson, R. C. Ion Coulomb crystals. *Contemp. Phys.* **56**, 63–79 (2015).
46. Dubin, D. H. E. & O’Neil, T. M. Trapped nonneutral plasmas, liquids, and crystals (the thermal equilibrium states). *Rev. Mod. Phys.* **71**, 87 (1999).
47. Ulm, S. *et al.* Observation of the Kibble-Zurek scaling law for defect formation in ion crystals. *Nat. Commun.* **4**, 2290 (2013).
48. Mielenz, M. *et al.* Trapping of topological-structural defects in coulomb crystals. *Phys. Rev. Lett.* **110**, 133004 (2013).
49. Ejtemaee, S. & Haljan, P. C. Spontaneous nucleation and dynamics of kink defects in zigzag arrays of trapped ions. *Phys. Rev. A* **87**, 051401 (2013).
50. Partner, H. L. *et al.* Dynamics of topological defects in ion Coulomb crystals. *New J. Phys.* **15**, 103013 (2013).

### Acknowledgements

We thank Jonas Keller for valuable help with the experiment control and many useful discussions, and Lars Timm for supporting numerical simulations. We thank Erio Tosatti and Andrey Surzhykov for reading of the manuscript. This work was supported by EPSRC National Quantum Technology Hub in Networked Quantum Information Processing (R.N.) and by DFG through grant ME 3648/1-1.

### Author contributions

The experiment was initiated and led by T.E.M. R.N. developed the numerical codes. R.N., J.K. and T.S. carried out the simulations. D.K. and J.K. designed the experiment with input from T.E.M. D.K. and J.K. carried out the experiments and performed the data analysis. All authors contributed to the discussion of results and participated in the manuscript preparation.

### Additional information

**Supplementary Information** accompanies this paper at <http://www.nature.com/naturecommunications>

**Competing interests:** The authors declare no competing financial interests.

**Reprints and permission** information is available online at <http://npg.nature.com/reprintsandpermissions/>

**How to cite this article:** Kiethe, J. *et al.* Probing nanofriction and Aubry-type signatures in a finite self-organized system. *Nat. Commun.* **8**, 15364 doi: 10.1038/ncomms15364 (2017).

**Publisher’s note:** Springer Nature remains neutral with regard to jurisdictional claims in published maps and institutional affiliations.



This work is licensed under a Creative Commons Attribution 4.0 International License. The images or other third party material in this article are included in the article’s Creative Commons license, unless indicated otherwise in the credit line; if the material is not included under the Creative Commons license, users will need to obtain permission from the license holder to reproduce the material. To view a copy of this license, visit <http://creativecommons.org/licenses/by/4.0/>

© The Author(s) 2017



# 3 P2: Nanofriction and motion of topological defects in self-organized ion Coulomb crystals

**Authors:** J. Kiethe, R. Nigmatullin, T. Schmirander, D. Kalincev, and T. E. Mehlstäubler

**Journal:** New Journal of Physics

**DOI:** 10.1088/1367-2630/aaf3d5

**Author contributions:** The experiment was initiated and led by T.E.M. R.N., T. S. and J. K. developed the numerical codes. J.K. and T.S. carried out and evaluated the simulations. D.K. and J.K. designed the experiment with input from T.E.M. D.K. and J.K. carried out the experiments and performed the data analysis. All authors contributed to the discussion of results and participated in the manuscript preparation.

**Copyright:** © 2018 The Authors. Published by IOP Publishing Ltd. on behalf of Deutsche Physikalische Gesellschaft. This article is licensed under a Creative Commons Attribution 3.0 licence.

PAPER • OPEN ACCESS

## Nanofriction and motion of topological defects in self-organized ion Coulomb crystals

To cite this article: J Kiethe *et al* 2018 *New J. Phys.* **20** 123017

View the [article online](#) for updates and enhancements.



**IOP** | ebooks™

Bringing you innovative digital publishing with leading voices to create your essential collection of books in STEM research.

Start exploring the collection - download the first chapter of every title for free.





## PAPER

## Nanofriction and motion of topological defects in self-organized ion Coulomb crystals

## OPEN ACCESS

## RECEIVED

20 June 2018

## REVISED

23 October 2018

## ACCEPTED FOR PUBLICATION

26 November 2018

## PUBLISHED

18 December 2018

Original content from this work may be used under the terms of the [Creative Commons Attribution 3.0 licence](#).

Any further distribution of this work must maintain attribution to the author(s) and the title of the work, journal citation and DOI.

J Kiethe<sup>1</sup>, R Nigmatullin<sup>2</sup>, T Schmirander<sup>1</sup>, D Kalincev<sup>1</sup> and T E Mehlstäubler<sup>1</sup> <sup>1</sup> Physikalisch-Technische Bundesanstalt, Bundesallee 100, D-38116 Braunschweig, Germany<sup>2</sup> Complex Systems Research Group, Faculty of Engineering and IT, The University of Sydney, Sydney, New South Wales 2006, AustraliaE-mail: [tanja.mehlstaebler@ptb.de](mailto:tanja.mehlstaebler@ptb.de)**Keywords:** nanofriction, topological defects, trapped ions, Coulomb crystals, discrete solitons

### Abstract

We study nanofriction in an ion Coulomb crystal under the presence of a topological defect. We have previously observed signatures of the pinning to sliding transition i.e. the symmetry breaking at the critical point and the existence of a vibrational soft mode. Here we discuss how they depend on the position of the topological defect and how external potentials, such as anharmonic trapping potentials or differential light pressure, can be used to change the defect position. The resulting forces tend to break the intrinsic crystal symmetry, thereby reducing mode softening near the transition. We show that the topological defect mode is sensitive to differential forces at the  $10^{-24}$  N level. We find that the local structure and position of the topological defect is essential for the presence of the soft mode and illustrate how the defect changes its properties, when it moves through the crystal.

### 1. Introduction

Friction influences many natural phenomena over several orders of magnitude of relevant length scales, from earthquakes to biological molecules [1]. Especially nanofriction processes on the atomic scale are nowadays of technical importance, due to advances made in such fields as nanofabrication [2] and biotechnology [3, 4]. To gain insights into the *in situ* dynamics of nanofriction processes, an emulation via laser-cooled and trapped ions was proposed [5–9]. These works suggested emulating one of the most fundamental models of nanofriction, i.e. the Frenkel–Kontorova (FK) model [10], using ion chains in an optical lattice [11–13]. Following the proposals, Bylinskii *et al* were able to trap 5 ions in an optical lattice, demonstrating the onset of reduced friction [14], the velocity dependence of the stick-slip motion [15], as well as single ion multi-slip behavior [16]. Furthermore, they observed structural symmetry-breaking at the pinning to sliding transition [17], an Aubry-type (AT) transition.

In actual nanocontacts, two layers of atoms are interacting with each other. The corrugation is then no longer given by a rigid potential, but rather by a deformable layer [18]. Recently, we presented a self-organized system, consisting of two deformable back-acting ion chains, without a fixed corrugation potential [19]. We showed that two-dimensional ion Coulomb systems under the presence of a topological defect [20–23] exhibit features of an AT transition, namely the breaking of analyticity of a hull function and a soft phonon mode. We also observed the symmetry breaking inside the crystal, which is a typical signature of finite systems [12, 13]. Our system shows similarities to other self-organized sliding systems, such as fibrous composite materials [4], sliding DNA strands [24] and propagation of protein loops [25]. While the investigation of nanofriction with the help of discrete topological defects, also known as kink solitons, is a new approach, these defects have been extensively studied with respect to the Kibble–Zurek mechanism [20–23, 26–28] and to quantum information [29, 30]. Also, the directed transport of topological defects via a ratchet mechanism has been recently reported [31].

In this paper, we take first steps towards the investigation of dynamic friction of the tribological system introduced above. We numerically investigate how several external forces influence the crystal structure, which subsequently change the position of the topological defect and the frequency of the vibrational soft mode. Forces under investigation result from effects, such as anharmonicities of the axial trapping potential, axial

micromotion and laser light pressure. We compare the results obtained for the anharmonic potentials with crystal positions observed in a prototype trap. All of these forces break the local crystal symmetry, which leads to a less pronounced soft mode. We show that the frequency of the kink mode is sensitive to differential forces at the level of  $10^{-24}$  N. We numerically investigate the motion of extended topological defects through the crystal induced by differential light forces, and discuss the associated periodic change in their physical properties, such as local structure and mode frequency. It should be emphasized that the paper focuses on the quasi-static sliding regime since it is implicitly assumed that the configuration of the Coulomb crystal immediately adjusts to the changes in the applied external forces.

This paper is structured in the following way. In section 2 we review the tribological system and the results of [19]. We discuss, previously not described, secondary gaps in the hull functions due to the crystal inhomogeneity and present the analysis of the Fourier spectrum obtained from molecular dynamics simulations to determine the temperature influence. The spectroscopic method to experimentally measure the defect mode, as well as numerical techniques to determine mode frequencies are explained. In section 3, we discuss how external forces influence the defect position and the vibrational soft mode, starting with anharmonic potentials, followed by axial micromotion and lastly differential light pressure. Building on these results, in section 4 we present the behavior of the topological defect, as it is moved through the crystal by differential light pressure. Finally, in section 5, we discuss our results and give an outlook to future experiments and theoretical investigations.

## 2. Pinning to sliding transition in a self-organized system

Our system consists of a two-dimensional ion Coulomb crystal in the zigzag phase with an extended topological defect in the center. The frictional process of interest is the sliding of the two chains against each other. In the following, we focus on the axial vector components of the motion, reducing the system to a one-dimensional problem. The interaction energies within the chains,  $U_{\text{intra}}$ , and between the chains,  $U_{\text{inter}}$ , characterize the regime of friction. To determine the critical point, we can estimate these energies from the characteristic distances in the Coulomb crystals. To do so, we model the two linear chains as classical particles of mass  $m$ , which interact within each chain via springs with constant  $\kappa_i$ , where  $i$  is 1 or 2, identifying the chains as illustrated in figure 1(a). The spring constants of the chains are different, due to the topological defect introducing a small mismatch between the inter-ion distances  $a_i$ . The chains are separated by a distance  $b$  and all masses are connected to a rigid support by springs of stiffness  $D = m\omega_z^2$ , which corresponds to the axial confinement of the ion trap  $\omega_z$ . Moving the chains against each other can be done via light forces acting on each chain independently, which we name  $F_i$ . Given this simplified model we can employ a harmonic approximation to roughly estimate the interaction energy of ions within the top chain as  $U_{\text{intra}} \approx \frac{1}{2}\kappa_1 z^2$ . The energy scale of the corrugation by the other chain can locally be approximated as  $U_{\text{inter}} \approx \frac{1}{2}U_0[\cos(2\pi a_2^{-1}z) + 1]$ , where  $U_0$  is the strength of the corrugation, which depends on  $b$ . If the chains are brought closer together  $U_0$  increases, changing the relative strength of the interactions. At a certain distance a critical depth of the corrugation potential  $U_c$  is crossed and the system changes from the sliding to pinning regime. At this point we expect a symmetry breaking of the crystal structure as illustrated in figure 1(b). The transition should happen when the competing energies are in balance. Representing these energies as angular frequencies in the harmonic approximation:

$\omega_{\text{pinning}} = \sqrt{2\pi^2 U_0 (ma_2^2)^{-1}}$  and  $\omega_{\text{natural}} = \sqrt{\kappa_1 m^{-1}}$  we can define a dimensionless corrugation parameter

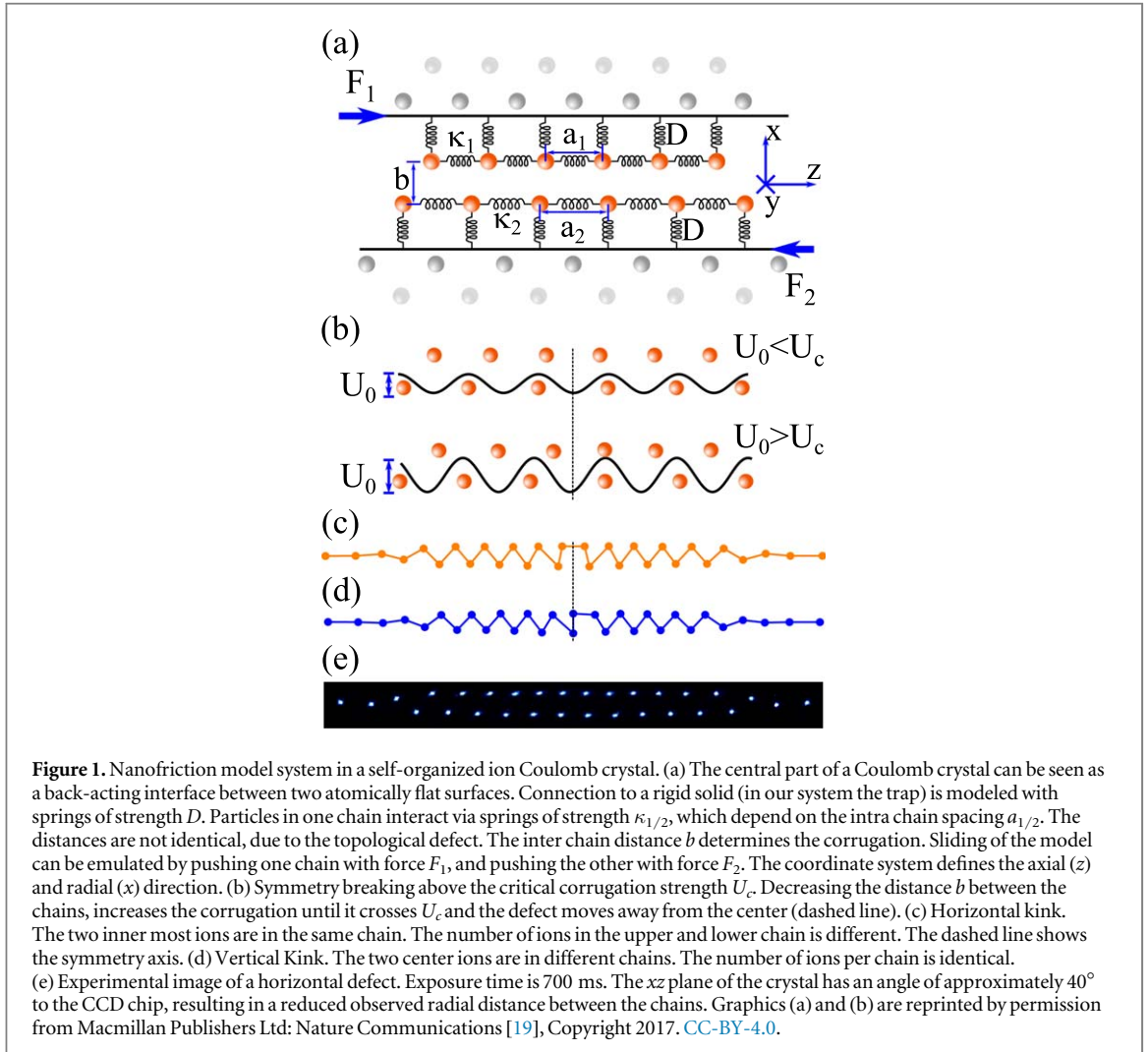
$$\eta = \frac{\omega_{\text{pinning}}^2}{\omega_{\text{natural}}^2}. \quad (1)$$

At the transition, we expect an  $\eta$  of order 1.

In order to estimate  $\eta$ , we approximate the frequencies  $\omega_{\text{pinning}}$  and  $\omega_{\text{natural}}$ , which describe a many-body interaction, with the help of the potentials, seen by one of the central ions. In a two-dimensional Coulomb crystal with a topological defect shown in figure 1(b), both central ions are located on the slope of  $U_{\text{inter}}$ . As a harmonic approximation is not valid there, we use the interaction energies  $\tilde{U}_{\text{inter}}$  and  $\tilde{U}_{\text{intra}}$  of a zigzag without defect as a further approximation. In such a crystal, all ions of one chain are located in the potential minimum of  $\tilde{U}_{\text{inter}}$ . The second-order Taylor expansion of  $\tilde{U}_{\text{inter}}$  and  $\tilde{U}_{\text{intra}}$  are then proportional to the approximate frequencies  $\tilde{\omega}_{\text{pinning}}$  and  $\tilde{\omega}_{\text{natural}}$ , respectively. This will result in an approximate corrugation parameter  $\tilde{\eta}$ , which has a critical value  $\tilde{\eta}_c$  different from 1.

### 2.1. Experimental system

In this section, we detail the experimental parameters necessary for implementing the above model system. We trap an ion Coulomb crystal with 30  $^{172}\text{Yb}^+$  ions in a high-precision linear Paul trap [32]. The ion trap chips are laser-machined with low tolerances and carefully aligned to reduce symmetry breaking of the electrode configuration. This reduces unwanted odd numbered anharmonic terms in the axial potential seen by the ions.



The ions are laser-cooled on the strong  $^2S_{1/2} \rightarrow ^2P_{1/2}$  dipole transition to temperatures in the low mK regime. The laser has a central wavelength of 369.5 nm and a beam diameter of 2.56 mm in axial ( $z$ ) and  $80 \mu\text{m}$  in radial ( $\approx \sqrt{x^2 + y^2}$ ) direction. Typical laser powers are 200–300  $\mu\text{W}$ . The fluorescence of the ions is imaged onto an electron multiplying  $512 \times 512$  pixel CCD camera via a lens system with  $\text{NA} = 0.2$  and magnification 24. The crystal's  $xz$  plane has an angle of roughly  $40^\circ$  to the CCD chip. This reduces the observed radial distance between the ions. On the camera, we can resolve individual ions and for an exposure time of 700 ms an ion position in a pure zigzag configuration can be resolved to 40 nm by fitting a Gaussian profile to the image. If the system is close to the AT transition, the resolution for the central ions, which are part of the topological defect, worsens.

In order to confine the crystal to the two-dimensional  $xz$  plane, we lift the degeneracy between the two radial potentials with the help of the dc potentials [32, 33], achieving a radial anisotropy of  $\omega_x/\omega_y = 1.3$ . In a two-dimensional crystal, the observed structural phase depends only on the relative magnitude of the transverse and axial confinement, quantified by the ratio of the respective secular frequencies  $\alpha \equiv \omega_x/\omega_z$ . This parameter is used in our calculations and experiments as a control to change the distance  $b$  and subsequently the corrugation  $\eta$ . For  $4.81 < \alpha < 13.6$  a crystal with 30 ions will be in the two-dimensional zigzag phase [34].

For a fixed axial secular frequency  $\omega_z \approx 2\pi \times 25$  kHz, topological defects can be created by rapidly quenching the rf amplitude of the radial confinement [21]. In terms of radial secular frequencies, this quench changes the confinement from  $\omega_x \approx 2\pi \times 500$  kHz to values ranging from  $2\pi \times 140$  kHz to  $2\pi \times 200$  kHz in 58  $\mu\text{s}$ . During this quench, several types of topological defects can be created in a finite ion Coulomb crystal in the two-dimensional phase [34]. The defect type is determined by the control parameter  $\alpha$ . For an ion number  $N = 30$  and the trap ratio in the range of  $4.81 < \alpha < 7.76$ , extended kinks are observed. For  $\alpha > 7.76$ , the defects are of the odd type [34, 35] and for  $\alpha < 4.81$  the crystal exhibits a three-dimensional helix configuration [36]. In the extended defect regime, which is relevant to the current paper, two kinds of defects can be observed. We refer to these defects as horizontal (H) kink and vertical (V) kink. The two kinks are depicted in figures 1(c) and (d). The most prominent difference between them is the position of the two inner most ions. In the horizontal case these ions are in the same chain and occupy the same minimum of the Coulomb potential

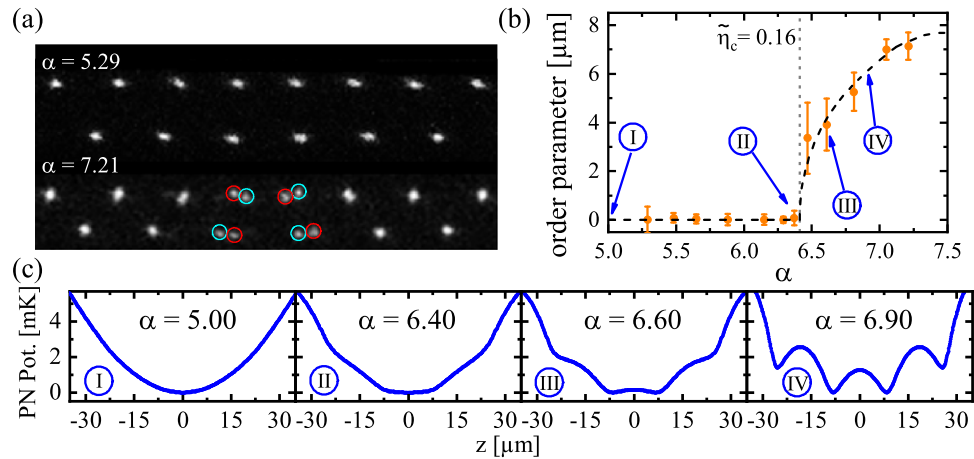


**Figure 2.** Symmetry breaking at the pinning to sliding transition. (a) Experimentally observed crystal configurations below the Aubry-type transition, at  $\alpha = 5.29$ , and above, at  $\alpha = 7.21$ . The images are taken with 700 ms exposure time. The crystal is at a finite temperature in the mK regime, which leads to multiple fluorescence spots above  $\alpha_c = 6.41$ , as the topological defect moves between the different stable positions. An angle of  $40^\circ$  between the crystals  $xz$  plane and the CCD chip, results in apparent smaller radial distances. (b) Absolute order parameter  $|\Phi_{\text{ced}}|$  against the trapping ratio  $\alpha$ . Experimental data (orange circles) and numerically obtained values for  $T = 0$  K (black dashed line) are shown. Experimental data represents a weighted average over 5–26 measurements per point, with exception of  $\alpha = 7.21$ , where only 2 configurations were observed. Error bars are given as one standard deviation weighted by fit errors. The critical point is  $\alpha_c \approx 6.41$  (approximate critical corrugation parameter  $\tilde{\eta}_c \approx 0.16$ ). (c) Peierls–Nabarro potential for different trapping ratios  $\alpha$ . The increasing PN barriers lead to the symmetry breaking of the system. Barriers for  $\alpha > \alpha_c$  are on the order of the temperature in the system, leading to multiple observed ion positions as the defect can move between different minima. Graphic (a) is reprinted by permission from Macmillan Publishers Ltd: Nature Communications [19], Copyright 2017. CC-BY-4.0

produced by the opposite chain. In the vertical case these ions are in different chains and the ion of the upper chain lies on the potential maximum created by of the lower chain. Another difference is the number of ions in each chain. Ignoring the first 4 ions on the left and right side of a crystal, as they are still close to the linear chain, a crystal with a V kink displays equal ion numbers for both chains. A crystal with an H kink exhibits a two ion difference between the chains. The kink is found in the center of the crystal, due its inhomogeneity [35]. In our experiments, both defects are created in a rf quench and are initially of odd type. They change to the extended type when the rf amplitude is lowered further [35, 37]. The overall probability to create a defect is around 30%, but only the H defect is used in the experiments, because only this defect shows a soft mode, if it is unperturbed, as we will show in section 2.4. Therefore, roughly 15% of all quenches result in a crystal with the necessary extended defect. An experimental image is shown in figure 1(e). The observed crystal configurations are highly symmetric due to the well controlled environment provided by the ion trap.

## 2.2. Structural symmetry breaking

For a finite system a symmetry breaking is expected at the AT transition [12, 13]. In the experiment, we observed several fluorescence spots in the symmetry broken regime, as can be seen in figure 2(a) for  $\alpha = 7.21$ , where fluorescence spots belonging to the same configuration are indicated by circles. The symmetry breaking is a direct result of the emerging barriers in the Peierls–Nabarro (PN) potential [10] at the critical value of the control parameter,  $\alpha_c$ . This potential describes the collective dynamics of a discrete nonlinear system. In our case, a PN barrier rises in the center of the crystal, see figure 2(c). As a result, the extended defect destabilizes and slips into the adjacent minimum of the PN potential, which alters the ion positions and breaks the axial mirror symmetry of the crystal. The finite temperature of the ions results in switching between stable configurations, and hence multiple spots per ion are observed during a finite exposure time of a few tens of ms. The barrier between the minima in the PN potential are on the order of 1–2 mK, comparable to the temperature of the crystal, which we estimate to be in the low mK regime [37]. We quantify the symmetry breaking with an order parameter  $\Phi$ , defined as the sum of the relative axial differences between next-neighbor ions from different chains

$$\Phi = \sum_{i \in \text{Chain1}} \text{sgn}(z_i) \cdot \min_{j \in \text{Chain2}} |z_i - z_j|, \quad (2)$$

where  $z_i$  is the axial coordinate of the  $i$ th ion and  $z = 0$  is the axis of symmetry for  $\alpha < \alpha_c$ . Below the transition the order parameter is 0. From numerical simulations, which are described in detail in section 2.4.2, we extract stable crystal configurations, which yield the order parameter shown in the dashed line of figure 2(b). The critical point is  $\alpha_c \approx 6.41$ , at which  $\Phi$  exhibits a sudden cusp. The corresponding approximate critical corrugation parameter  $\tilde{\eta}_c$  is 0.16, which is different from 1, since it is only a rough estimate. Taking fluorescence images of crystals at various  $\omega_x$ , we extract the ion positions via fitting the fluorescence profile of the individual ions to a

Gaussian function. To avoid errors due to optical aberrations far away from the optical axis and to reduce accumulated fitting errors, we do not use the full version of (2). The reduced order parameter  $\Phi_{\text{red}} = \Phi_{i=N/2} + \Phi_{i=N/2+1}$  only includes the two central terms, which have the largest contribution to  $\Phi$ . The value of  $\alpha_c$  is not influenced by the choice of  $\Phi$ . The experimental results are plotted as orange circles in figure 2(b), and they agree well with the numerical calculations. The error bars are one standard deviation weighted by the fit errors. Measuring  $\Phi$  for  $\alpha > \alpha_c$  close to the critical point is limited by the resolution of the EMCCD camera, as the fluorescence spots of two configurations need to be at least 2 pixel apart in order to be identified as distinct configurations.

### 2.3. Derivation of the hull function in a self-organized system

The symmetry breaking in finite systems is also accompanied by the more general breaking of analyticity of the hull functions [12]. In the following paragraphs, we will discuss the hull function and its numerical calculation in our model system in more detail.

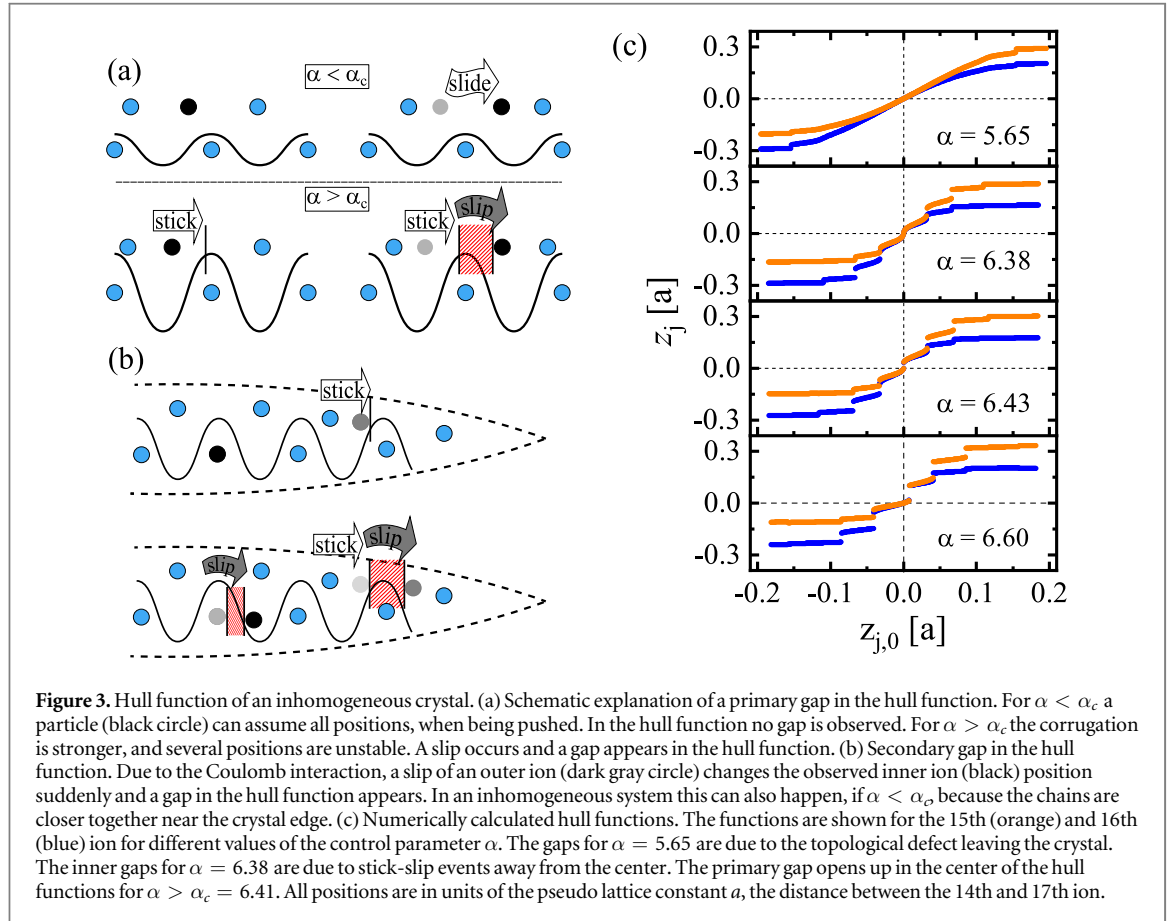
In the FK model the hull function parameterizes the reachable ground state configurations of an incommensurate system [10, 11]. If the system is below the Aubry or AT transition, i.e. free sliding, this function is continuous and analytic. Intuitively this means that during a sliding process of the chain over the potential, all individual particle positions are a realization of a ground state of the system. This changes when the Aubry transition is crossed, and the system start to exhibit stick-slip motion. Certain positions are unstable and not part of the set of ground state solutions, resulting in a discontinuous hull function with broken analyticity [11]. This property of incommensurate sliding systems exists in both infinite and finite systems, though the two cases are not identical.

In the classical FK model the corrugation potential is not influenced by the particle chain residing above it, which leads to a straightforward representation of the hull function. It is defined as an implicit function  $z_j(z_{j,0})$ , where  $z_j$  is the position of  $j$ th ion in the presence of the corrugation potential and  $z_{j,0}$  is the position of the  $j$ th ion in the absence of the corrugation potential [10]. The particle positions can be calculated with the help of a force  $F$  that pushes the chain along the axial direction. Doing this calculation with and without a corrugation potential yields  $z_j$  and  $z_{j,0}$ , which determine the implicit relation  $z_j(z_{j,0})$ . Such a procedure is possible, because the corrugation strength  $U_0$  can be set to zero without altering the interaction between chain particles. For a self-organized system, like a two-dimensional ion Coulomb crystal, this approach does not work, because the corrugation potential is part of a back-acting system. Removing it without changing the dynamics of the interaction between particles of the same chain is impossible.

However, in a harmonically trapped system, one can push the complete crystal with a force  $F$ , leaving the local ion interactions unchanged, to obtain a relation between the force and the unperturbed coordinates,  $z_{j,0}(F)$ . Applying an axial shear force  $\Delta F$  onto the chains, slides the particles over the corrugation potential, leading to perturbed positions  $z_j(F)$ . The shear force is such that one chain is pushed by  $+F/2$ , while the other chain is pushed by  $-F/2$ . Then the relative force between the chains is equal to  $F$ , which was used to push the whole crystal. The unperturbed and perturbed coordinates are related via the applied force  $F$ , providing a representation of the hull function  $z_j(z_{j,0})$ . The hull functions for the two ions at the center of the crystal, ion 15 and 16, are shown in figure 3(c).

In the hull function, various gaps open up above the transition due to stick-slip events. These events result from the emergence of the PN barriers above the AT transition, which destabilize crystal configurations, as can be seen in figure 2(c). The central gap seen in figure 3(c) for  $\alpha > 6.41$  is a direct result of a slip event of the 15th or 16th ion, see figure 3(a). If the slip event takes place at the position of the defect, the opening in the hull functions is called the primary gap. The non-central gaps in the hull functions of the 15th and 16th ions are either remnants of a slip event of other ions or the defect leaving the crystal, which we previously did not discuss. If the defect leaves the crystal, a part of the crystal will reorient itself affecting the positions of the central ions. This is observed, for instance, far below the transition at  $\alpha = 5.65$  and  $z_{j,0} \approx 0.15a$ , where  $a$  is the axial spacing between the 14th and 17th ion, which we consider as a pseudo lattice constant for the crystal center. As the pure zigzag has mostly matched chains, no further information about the AT transition can be gained for bigger forces. Here we note that, even though the individual ions moved less than a third of a lattice period ( $\Delta z < 3 \mu\text{m}$ ), they have rearranged in a way such that the defect already left the crystal, which means it moved more than  $100 \mu\text{m}$ . This illustrates why charge transport is facilitated by topological defects [38].

For  $\alpha = 6.38$ , still below  $\alpha_c$ , more than one gap can be seen in the hull function. One in each function is due to the defect leaving the crystal. The others are secondary gaps due to stick-slip events, even though the system is globally in the sliding regime. The stick-slip events occur, because of the inhomogeneity of a harmonically trapped crystal, which reduces the charge density towards the edge of the crystal, as illustrated in figure 3(b). This increases the corrugation depth between the ion chains, as the axial distance between ions grows, while the radial distance between the chains decreases. Therefore, the critical point is locally already crossed, if the local ordering is disturbed by a topological defect. The slip events from these ions are seen by the central ions 15 and 16, which



gain gaps in their hull functions as a result. In a crystal with equidistant ions, the secondary gaps will only exist above  $\alpha_c$ , as only in this regime stick-slip motion is present.

## 2.4. Motional mode frequency of the topological defect

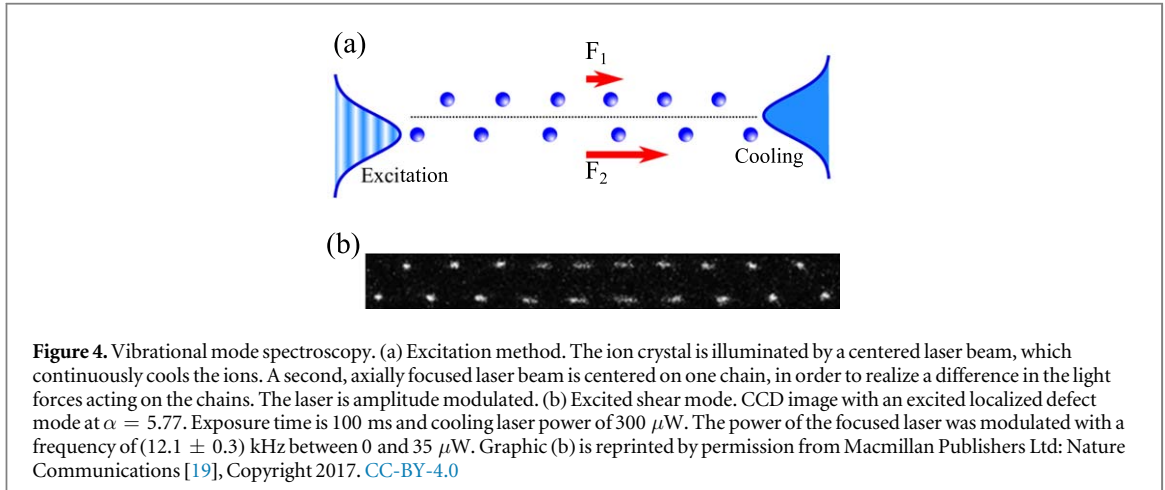
The localized vibrational mode of the topological defect drives the AT transition [19]. The lower its frequency, the lower the energy required, to move the chains against each other. This defect mode is one of the gapped modes, previously considered for quantum information [29]. Excitation of the high energy gapped mode was shown in [31]. Here, we summarize our results on the spectroscopy of the low energy gapped mode in dependence of the corrugation strength and give detailed information on experimental and numerical techniques we employed. Also, the dependence of the kink mode frequency on the ion number is measured and simulated.

### 2.4.1. Spectroscopy

Experimentally, we measure the vibrational mode frequency via amplitude modulation  $P(t) = P_0/2[\cos(2\pi \cdot \nu t) + 1]$  of a laser addressing the  $^2S_{1/2} \rightarrow ^2P_{1/2}$  transition, where  $P_0$  is the power without modulation and  $\nu$  is the modulation frequency. This exerts a periodic force

$$F_p = \frac{F_0}{2}[\cos(2\pi \cdot \nu t) + 1] \quad (3)$$

on the crystal, where  $F_0/2$  is the amplitude of the modulation, which depends on  $P_0$  and the detuning from the atomic resonance  $\delta$ , which is typically  $-\Gamma/2$ , with  $\Gamma \approx 2\pi \times 19.6$  MHz, the natural line width of the atomic transition.  $F_p$  can excite a motional mode  $k$ , if  $\nu$  is close to a mode frequency  $\nu_k = \omega_k/(2\pi)$ . Additionally, the intensity distribution of the laser  $\mathbf{A}$  must overlap with the mode vector  $\boldsymbol{\mu}_k$ . This means that the scalar product  $\boldsymbol{\mu}_k \cdot \mathbf{A}$  has to be non-zero. The laser used in our experiments has an angle of  $25^\circ$  to the crystal axis and an approximate angle of  $50^\circ$  to the  $xz$  plane of the crystal. The beam has a Gaussian beam profile with waist  $w$  of roughly  $80 \mu\text{m}$  in both directions. A typical zigzag configuration in our setup has a radial separation of the ion chains of approximately  $15 \mu\text{m}$ . Together with the angle to the beam wavefront, this leads to an apparent separation of  $10.6 \mu\text{m}$ , which is not much smaller than  $w$ . If the beam is centered on the crystal, the intensity distribution will be identical for both chains. This would result in a zero overlap with the localized defect mode of the crystal, as both chains are excited with the same force and in the same direction. If the intensity maximum



is focused radially on one of the chains, see figure 4(a), then an intensity difference between the chains exist, which results in a non-zero scalar product,  $\boldsymbol{\mu}_k \cdot \mathbf{A}$ , enabling the excitation of the localized defect mode. The intensity difference leads to a differential force  $\Delta F = F_1 - F_2 \neq 0$  along the axial direction, where  $F_{1,2}$  is the force along  $z$  acting on chain 1 and chain 2, respectively. For the excitation of the topological defect mode, this  $\Delta F$  is the periodic force exciting the motion. To determine the resonance frequency,  $\nu$  is scanned at a rate of 1–2 kHz  $\text{s}^{-1}$  and the spread of the fluorescence of the central ions is recorded with the EMCCD camera. An example image of the excited defect mode is shown in figure 4(b). Only the central ions move with a significant amplitude, illustrating that the excitation is localized on the defect. The resonance is measured with an uncertainty of 300–400 Hz, which can be improved by a slower frequency scan rate and recording more images per scan. The applied amplitude  $F_0/2$  on the crystal needs to be big enough to actually excite observable motion but also has to be small enough, to limit nonlinear excitations. In our experiment we found that an amplitude  $F_0/2$  corresponding to  $P_0 = 20 \mu\text{W}$  and  $\delta = -\Gamma/2$  is enough to excite motion near the phase transition. We calculate the average force,  $F_0/2 \propto P_0/2$ , acting on the ions in the intensity maximum of the laser to be  $24.5 \times 10^{-21}$  N. The ions of the other chain experience on average a force of  $23.9 \times 10^{-21}$  N. The differential force  $\Delta F$ , used to excite the motion of the topological defect mode, is then  $0.6 \times 10^{-21}$  N. The influence of this force on the crystal is discussed further in section 3.3. While exciting the motion with the focused laser beam, the ions were still illuminated with a spatially extended cooling beam. This beam damps the dynamics introduced via the amplitude modulation. Typical powers of the cooling beam, while conducting spectroscopy, are 200–300  $\mu\text{W}$ .

#### 2.4.2. Numerical calculations

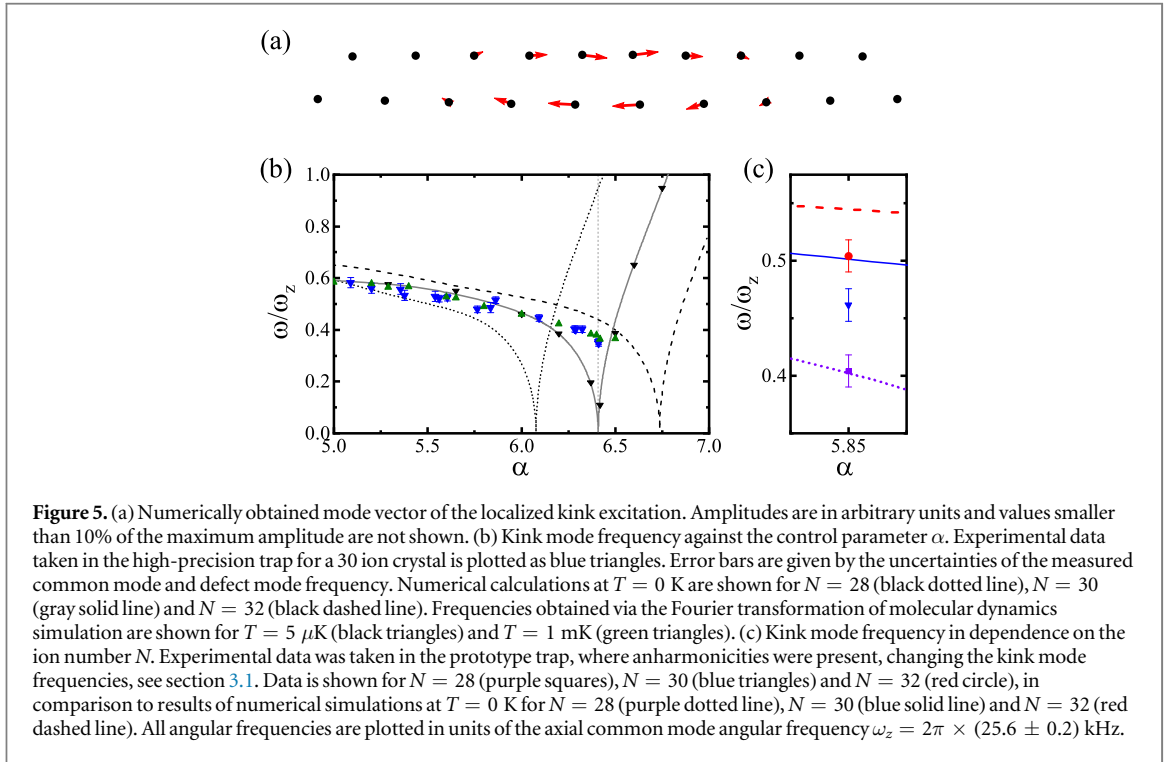
Firstly, we look at the expected mode frequency in dependence on the control parameter  $\alpha$ . For this, we analyze the total potential energy of  $N$  harmonically trapped ions in two-dimensions:

$$V = \sum_{i=1}^N \frac{m}{2} (\omega_x^2 x_i^2 + \omega_z^2 z_i^2) + \frac{e^2}{4\pi\epsilon_0} \sum_{i=1}^N \sum_{j<i} |\mathbf{r}_i - \mathbf{r}_j|^{-1}, \quad (4)$$

where  $x_i$  and  $z_i$  are the coordinates of  $i$ th ion in the coordinate systems defined in figure 1(a);  $\omega_x$  and  $\omega_z$  are the harmonic trapping frequencies; and  $\mathbf{r}_i \equiv \{x_i, z_i\}$ . The third-dimension is neglected, due to the anisotropy of the radial secular frequencies. We obtain the frequency of the topological defect mode (and any other mode) by numerically diagonalizing the Hessian matrix

$$H_{i,j} = \left. \frac{\partial^2 V}{\partial q_i \partial q_j} \right|_{\mathbf{q}(0)}, \quad (5)$$

where  $V$  is the total potential energy given by (4),  $q_i$  are the degrees of freedom and  $\mathbf{q}(0)$  is a given equilibrium configuration. The stable equilibrium configuration,  $\mathbf{q}(0)$ , is obtained by numerically solving the equations of motions under high damping. There are  $2N$  vibrational normal modes in a two-dimensional ion crystal with  $N$  ions. The  $k$ th eigenvector of  $H_{ij}$  is the  $k$ th normal mode of the crystal  $\boldsymbol{\mu}_k$ , and the corresponding eigenvalue  $\lambda_k$  determines the mode frequency via the relation  $\omega_k = \sqrt{\lambda_k/m}$ . The localized defect mode has the lowest frequency for  $\alpha < 7$ , and it drives the symmetry breaking transition. We show the crystal configuration and the defect mode vector in figure 5(a). Figure 5(b) shows the shear mode frequency as a function of  $\alpha$  for different



numbers of ions  $N$ . The frequency tends to zero near the critical point  $\alpha_c \approx 6.41(6.08, 6.74)$  for  $N = 30(28, 32)$ , while increasing both above and below  $\alpha_c$ , because of the finite size of the system. The critical point  $\alpha_c$  depends on the ion number  $N$  due to the increase in charge density with more  $N$ . The more ions are present, the stronger is the repulsive Coulomb force, and therefore the more radial confinement, and subsequently higher  $\alpha$ , is necessary to bring the chains close enough together to observe the AT transition. In a previously installed prototype trap [39], we observed the dependence of the defect mode frequency on  $N$ , see figure 5(c), but typically with lower frequencies, than the calculations predict. This disagreement comes most likely from anharmonicities in the axial potential, see section 3.1. The apparent agreement for  $N = 28$  is due to the fact that simulated frequency decrease towards 0 around  $\alpha \approx 5.75$ , while the experimentally observed frequencies show a much smaller decrease, when  $\alpha$  is increased towards  $\alpha_c$ . At some  $\alpha$  the lines will cross, which is coincidentally near the  $\alpha$  value we chose to measure. Near the AT transition we observe a difference between the measured and calculated frequencies in both the high-precision and the prototype trap. This discrepancy stems mainly from the missing temperature effects in the numerical calculations.

In order to investigate the effect of a finite crystal temperature, we conduct three-dimensional molecular dynamics simulations of an unperturbed crystal (i.e. without laser excitation, but with cooling). These simulations solve the Langevin equations, utilizing an impulse integrator algorithm [40]. The total potential energy of a three-dimensional  $N$  ion system is

$$V = \sum_{i=1}^N \frac{m}{2} (\omega_x^2 x_i^2 + \omega_y^2 y_i^2 + \omega_z^2 z_i^2) + \frac{e^2}{4\pi\epsilon_0} \sum_{i=1}^N \sum_{j<i}^N |\mathbf{r}_i - \mathbf{r}_j|^{-1}, \quad (6)$$

where  $x_i, y_i$  and  $z_i$  are the coordinates of  $i$ th ion  $\omega_x, \omega_y, \omega_z$  are the harmonic trapping frequencies; and  $\mathbf{r}_i \equiv \{x_i, y_i, z_i\}$ . The equation of motion for the  $j$ th ion in one-dimension is

$$m\ddot{\chi}_j + \nabla_{\chi} V + \eta\dot{\chi}_j = \xi_{\chi j}(t), \quad (7)$$

where  $\xi_{\chi j}(t)$  is a stochastic force,  $\chi$  is  $x, y$  or  $z$ ,  $\eta$  is a damping term from laser cooling and  $V$  is the total potential energy from (6). The stochastic force fulfills the following two conditions:

$$\langle \xi_{\chi j}(t) \rangle = 0, \quad (8)$$

$$\langle \xi_{\chi j}(t) \xi_{\gamma k}(t') \rangle = 2\eta k_B T \delta_{\chi\gamma} \delta(t - t'), \quad (9)$$

where  $\gamma$  is  $x, y$  or  $z$ ,  $j$  and  $k$  are ion indices and  $\langle \dots \rangle$  indicates time averaging. Equation (9) is the fluctuation–dissipation relation that ensures that the system undergoing the stochastic dynamics equilibrates at temperature  $T$  [21]. In these simulations we look at crystals with topological defects for different temperatures  $T$ , each time



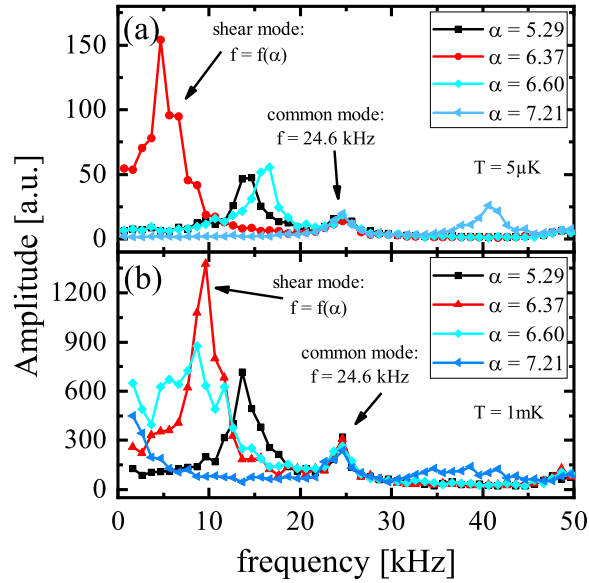


**Figure 6.** Spectra obtained via Fourier transformation of molecular dynamics simulations. (a) Spectrum for  $T = 5 \mu\text{K}$  for different  $\alpha$ . Common mode, independent of  $\alpha$ , visible at 24.6 kHz. The frequency of the defect mode depends on  $\alpha$ . (b) Spectrum for  $T = 1 \text{ mK}$ . The frequency spread of the defect mode becomes broader the closer the system is to  $\alpha_c$ . Above the transition ( $\alpha = 6.6$  and  $\alpha = 7.21$ ) a range of several kHz with comparable amplitude is observed. Therefore, no single harmonic oscillation has an observable amplitude.

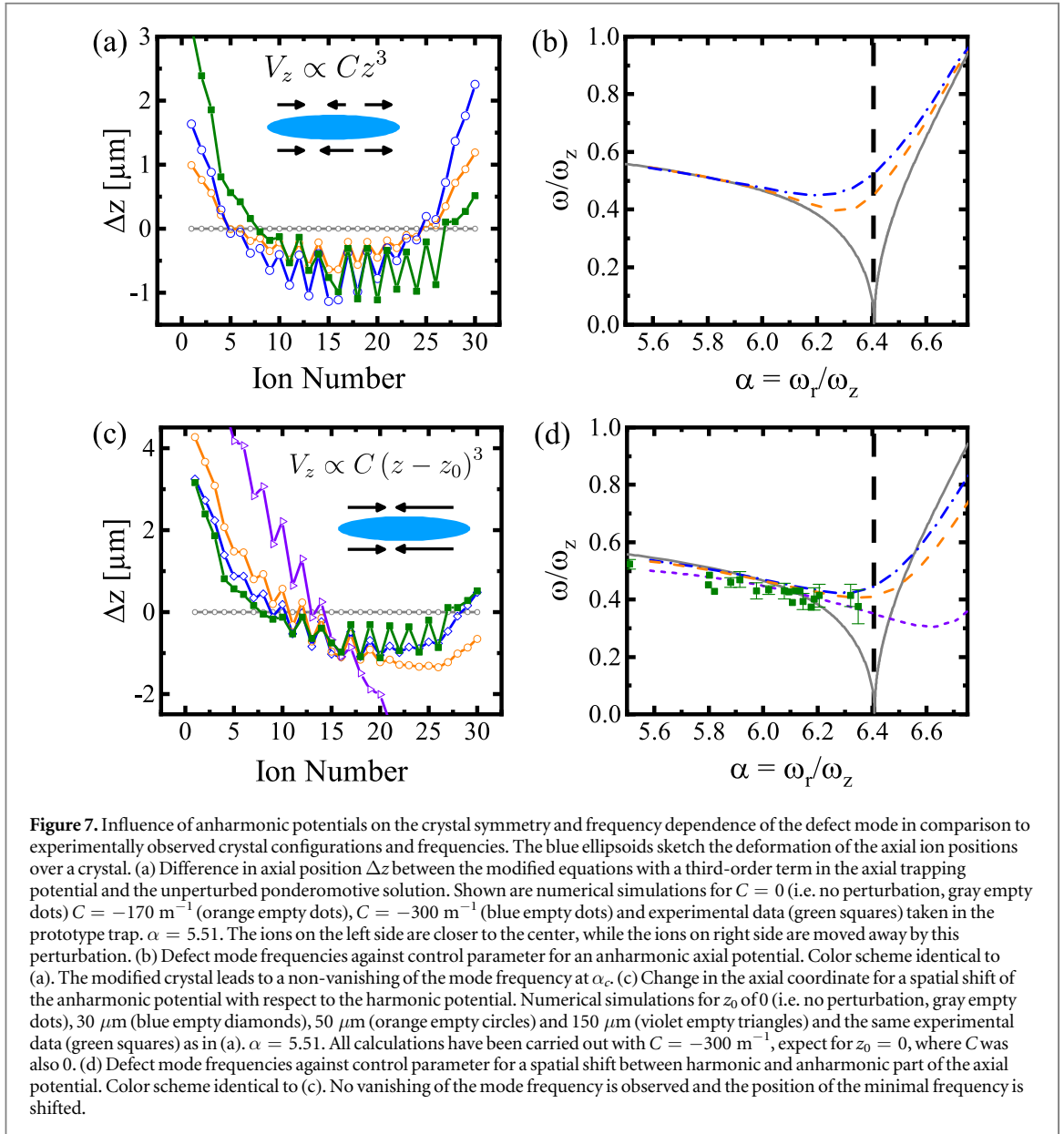
letting the system evolve freely for 10 ms. We then analyze the resulting axial trajectory of the 15th ion,  $z_{15}(t)$ , because this ion has one of the highest mode amplitudes for the localized defect mode in axial direction. Taking the Fourier transform of this trajectory

$$\hat{z}_{15}(\nu) = \mathcal{F}(z_{15}(t)) \quad (10)$$

yields the spectrum of the harmonic motions excited in the crystal dynamics. Figure 6(a) shows the spectrum for a crystal at  $T = 5 \mu\text{K}$  for different trapping ratios  $\alpha$ . The amplitude peak at a frequency of 24.6 kHz is due to the excitation of the axial common mode, for which all ions oscillate in phase, and the other amplitude peaks are due to excitation of the topological defect mode at different corrugations. The dependence of the mode frequency on  $\alpha$  at  $5 \mu\text{K}$  is shown with black triangles in figure 5(b). These results agree with the frequencies obtained from the diagonalization of the Hessian matrix. The observed Fourier spectrum changes, when  $T$  is increased. At experimentally realistic temperatures of 1 mK the Fourier spectrum close to, and above, the transition changes, as can be seen in figure 6(b). The common mode can still be resolved independently of the trapping ratio, but only below  $\alpha_c$  we observe distinct peaks for the defect mode in the spectrum. Additionally, these peaks are visible at different frequencies in comparison to the results for  $T = 5 \mu\text{K}$ . For  $\alpha > \alpha_c$  a broad range of frequencies with nearly identical amplitudes is seen (for  $\alpha = 6.6$  near 10 kHz and for  $\alpha = 7.21$  near 40 kHz), indicating that no single harmonic oscillation is present. This can be explained by the PN potential barriers, which are in the mK range, see figure 2(c), and small enough for the defect to overcome. During the movement between the minima, the nonlinear parts of the PN potential are sampled and many frequency components are part of the dynamics, explaining why the mode of the defect could not be excited with an observable amplitude in the experiment for  $\alpha > \alpha_c$ . Furthermore, we find that the frequencies extracted from the Fourier analysis for  $T = 1 \text{ mK}$  agree with the experimentally observed frequencies, see figure 5(b). This indicates that the frequency measurements were limited by the finite Doppler cooling temperature of the  $^2\text{S}_{1/2} \rightarrow ^2\text{P}_{1/2}$  transition.

### 3. Symmetry breaking by external forces

In this section, we investigate several external forces on ion Coulomb crystals, how they change the crystal structure and subsequently the mode frequencies. This is of interest for directed transport of kink solitons [31] and the frictional properties, as a change in the soliton mode frequency implies different interaction energies between the chains. In a previously used prototype trap [39], we observed asymmetric crystal configurations and measured lower frequencies of the localized defect mode, than the calculations predict. Therefore, we investigate here trap related forces, such as those stemming from higher order terms in the axial trapping potential and axial micromotion, as well as forces due to laser illumination of the ions. While all effects change the crystal and hence the position of the topological defect, the latter effect offers the possibility to move the defect at will through the crystal.



### 3.1. Anharmonicities of the trapping potential

As the manufacturing process of an ion trap is limited by its tolerances, the trap potential will contain non-quadratic contributions [41].

Here, we investigate the influence of a third-order term in the axial trapping potential on the crystal structure, position of the topological defect and the frequency dependence on the corrugation. This is done numerically by changing the potential term for the  $z$  direction:

$$m\omega_z^2 z^2 \rightarrow m\omega_z^2 (z^2 + C \cdot z^3),$$

where  $C$  determines the relative strength of the third-order term. The addition of the anharmonic term to the potential perturbs the equilibrium positions of the ions. We define the difference of the axial positions of a modified crystal  $z_{j,\text{mod}}$  and the axial positions of an unperturbed crystal  $z_{j,\text{pond}}$  as  $\Delta z_j = z_{j,\text{anharmonic}} - z_{j,\text{pond}}$  where  $j$  is the ion index. We plot the difference in figure 7(a). The order of magnitude for the  $C$  was chosen such that the resulting distortion is in the  $\mu\text{m}$  regime, similar to the observed distortion in the prototype trap. The modified confining potential has a higher curvature on one side of the crystal, while the other side has a lower curvature in comparison to the ideal case. One side of the crystal is therefore pushed closer to the center, while the other side is shifted away from it. This change in the axial positions influences the interaction between the ions and thus modifies the dependence of the localized defect mode frequency on  $\alpha$ , see figure 7(b). In particular, in the presence of the third-order term in the axial potential, the mode softening is less pronounced or not present at all, depending on the strength of  $C$ .

Up to now we have assumed that the minimum of the second-order term and the saddle point of the third-order term are at the same axial position. As far as we know, there is no reason that this is necessary. To match the experimental crystal configuration to the simulation, we include a differential shift  $z_0$  in the position of  $z^2$  and  $z^3$  terms in regard to the crystal structure and the mode frequency, with results shown in figures 7(c), (d). Shifting the  $z^3$  term by only  $30 \mu\text{m}$  relative to the  $z^2$  term yields a significantly distorted crystal configuration, in which the left side is pushed towards the center by a few  $\mu\text{m}$ , while the right side is only slightly perturbed. In figure 7(c) we fit the simulation to the experimentally observed difference  $\Delta z_{j,\text{exp}}$  by minimizing  $\sum_j |\Delta z_j - \Delta z_{j,\text{exp}}|$ . We find a good overall agreement of the distortions for  $C = -300 \text{ m}^{-1}$  and  $z_0 = 30 \mu\text{m}$ . In the frequency dependence we observe not only a less pronounced soft mode, but also a shift of the minimum of the localized mode frequency towards higher values of the control parameter  $\alpha$ . As it is possible to fit the simulations with anharmonic terms closely to observed crystals in the prototype trap, it is plausible that the potential of the prototype trap included significant higher order terms. This is most likely due to the manufacturing process, as the prototype trap was milled, resulting in slightly asymmetric trap segments.

Both the anharmonic potential itself and the shift from the harmonic part lead to an intrinsic symmetry breaking and a change of the defect mode frequency near the transition. It is therefore necessary to suppress anharmonic potential terms in an ion trap, for experiments that require high symmetry of the crystal. Higher order odd exponent terms can be minimized by the design and careful construction of the trap. Depending on the trap geometry and the strength of the observed anharmonic contribution, it might also be possible to compensate for higher order terms with carefully chosen axial DC potentials. This can in principle also be used to move the defect through the crystal, but will most likely result in an overall distorted crystal shape.

### 3.2. Micromotion

As all investigations take place in a 2D crystal, where most ions are situated in a non-zero rf field, the micromotion induced by the oscillating trapping field changes the structure and the dynamics of the ion crystal in comparison with the ponderomotive approximation [42]. Furthermore, due to the finite size of the segmented linear Paul trap there are electric field gradients from the rf fields along the axial direction. This additional gradient induces axial micromotion, which might also influence the crystal.

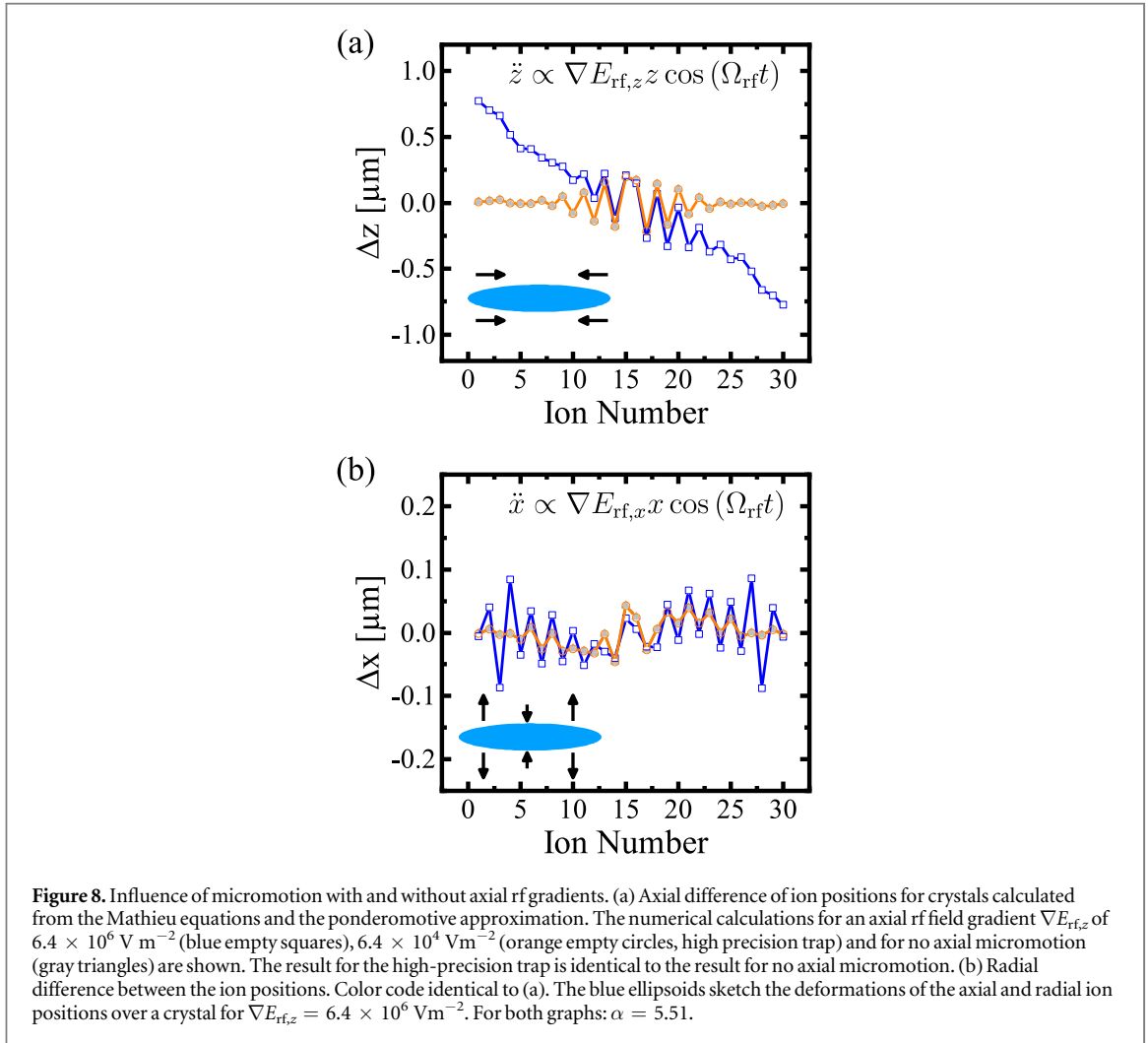
The dynamics of ions trapped in a rf field are described by the Mathieu equations [43]. Solving these equations for a 30 ion crystal containing a defect at a radial trapping frequency  $\omega_x = 2\pi \times 132 \text{ kHz}$  and comparing it to the ponderomotive approximation, reveals differences  $\Delta z_j = z_{j,\text{Mathieu}} - z_{j,\text{pond}}$  of less than  $200 \text{ nm}$  in the  $z$  coordinates of the ions. If axial micromotion with an electric field gradient  $|\nabla E_{\text{rf},z}|$  of 2% of the radial electric field gradient  $|\nabla E_{\text{rf},r}| = 3.2 \times 10^8 \text{ Vm}^{-2}$  is also present, then the crystal is axially compressed, see figure 8(a). The further away an ion is from the center of the trap, the further its position is changed by the micromotion. Because the rf gradient changes sign in the center of the trapping region it acts like an additional axial potential, as long as the crystal is in the center of the trapping region. In the prototype trap the axial micromotion has an electric field gradient of  $|\nabla E_{\text{rf},z}| = 1.9 \times 10^6 \text{ V m}^{-2}$ , which is roughly 0.6% of the radial electric field gradient  $|\nabla E_{\text{rf},r}|$  [39] and in the precision trap we observe only an electric field gradient of  $|\nabla E_{\text{rf},z}| \approx 6.4 \times 10^4 \text{ Vm}^{-2} \approx 2 \times 10^{-4} \cdot |\nabla E_{\text{rf},r}|$  along the axial direction [44]. For both traps, the calculated differences  $\Delta z_j$  are nearly identical to the simulations without any axial micromotion, making the effect negligible. In the radial direction the effect of axial micromotion is small in comparison. In figure 8(b) we plot the difference in the  $x$  coordinate. For a high axial micromotion of  $2\% \cdot |\nabla E_{\text{rf},r}|$  the difference in radial coordinates  $\Delta x_j$  due to the axial micromotion are less than  $100 \text{ nm}$ . Using the axial electric field gradients from both traps, we again do not observe a difference to the simulations without any axial micromotion.

The mode frequencies were not calculated for this effect, as the simulation using the full Mathieu equations does not yield a static solution needed for the Hessian matrix approach. It is possible to calculate the normal mode spectrum using the Floquet–Lyapunov approach [42, 45], but this is outside of the scope of this paper. The influence of micromotion is only relevant for traps with an axial rf field gradient higher than 0.6% of the radial rf field gradient. This gradient can only be suppressed by the design and careful manufacturing of the trap [33].

### 3.3. Differential light forces

Illuminating ions with near resonant light will lead to an average force acting on them. These light forces will in general modify the crystal structure, but as long as the illumination is uniform on the crystal, they will only shift the center of mass. However, a small differential force  $\Delta F$  between the ion chains was needed to excite the topological defect mode, see section 2.4. In this section we investigate how such a force influences the topological defect.

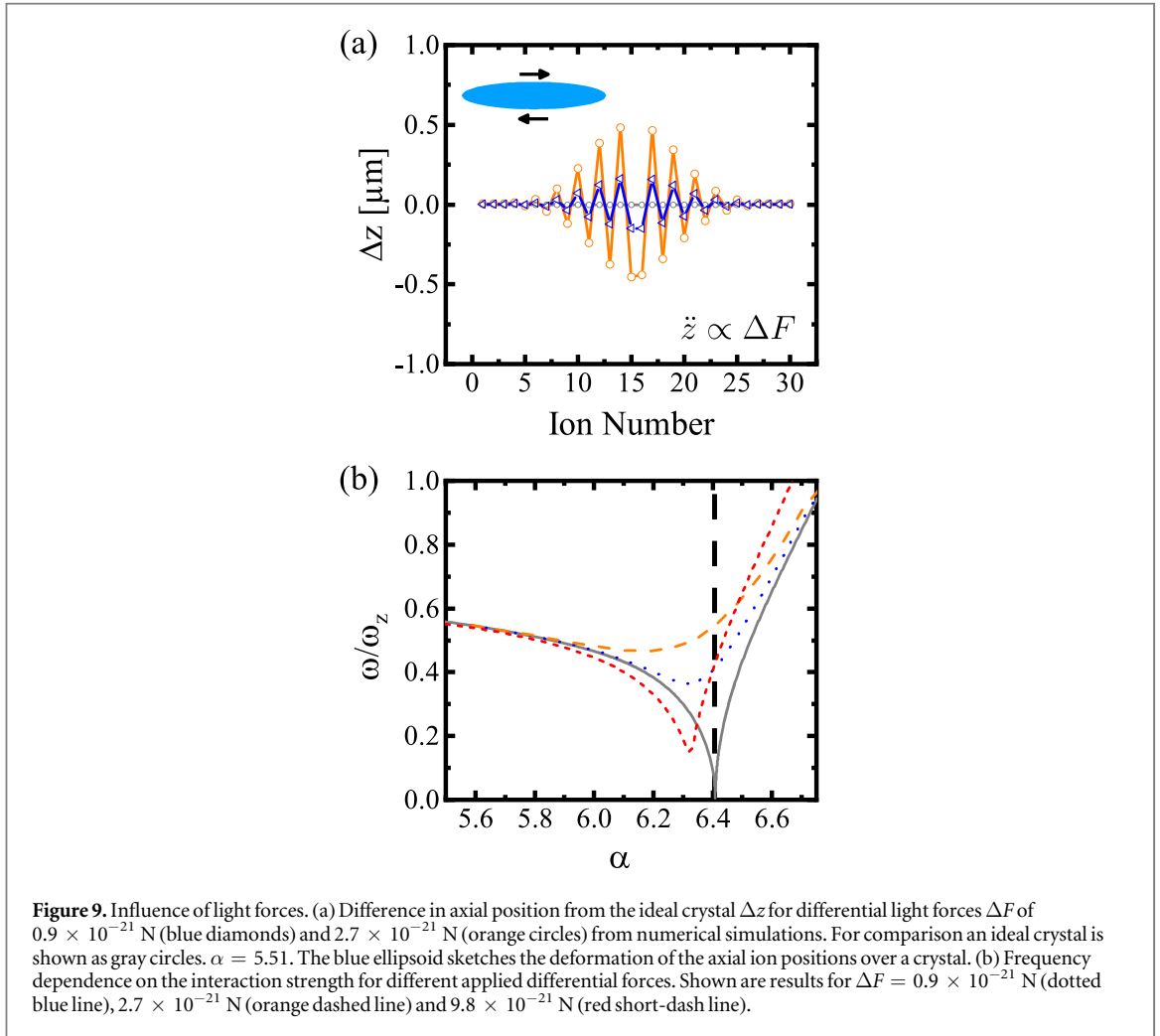
For this we introduce an additional force  $\Delta F$  in the equations of motion of each ion  $j$ , which depends on the radial ion position. The sign of  $\Delta F$  is positive for  $x_j > 0$  and negative for  $x_j < 0$ . From numerical simulations we find that such a differential force will move the topological defect inside the crystal, see figure 9(a), in which we



plot the change in the axial crystal structure. This effect can be actively used, to investigate charge or information transport in ion Coulomb crystals [29], as well as further investigations into nanofriction of two sliding chains. In section 4 we investigate in detail, what such a movement entails.

When applying differential forces to the crystal, the localized kink mode frequency near the phase transition will change. For different  $\Delta F$ , we plot the expected frequency dependence on  $\alpha$  in figure 9(b). The frequency change can be understood by examining the PN potential, shown in figure 2(c). The potential is overall confining due to the inhomogeneity of the crystal, and it contains PN barriers above the AT transition. The overall positive curvature of the PN potential explains why a finite frequency below the AT transition exists. This positive curvature is balanced by the negative curvature of the emerging PN barrier at  $z = 0$  when the system is near the phase transition, resulting in near zero frequency of the localized mode. However, when differential forces are applied, the kink soliton is shifted away from the point, where a PN barrier is formed. This leads to the observed non-zero harmonic frequency. Increasing  $\Delta F$  further, results again in a soft mode behavior of the defect frequency, see figure 9(b) for  $\Delta F = 9.8 \times 10^{-21} \text{ N}$ .

In order to compare this result with our experiments, we calculate realistic differential forces for the setup. The maximum  $\Delta F$  due to a single laser beam on a zigzag crystal is achieved, if the radial crystal center is situated near the maximum slope i.e. at  $z \approx \pm w/2$  of the Gaussian intensity distribution  $I(z) = I_0 \exp(-2z^2/w^2)$ , where  $I_0$  is the intensity in the center and  $w$  is the beam waist. Using the experimental parameters of section 2.4, we find that with this configuration a  $\Delta F$  around  $2.1 \times 10^{-21} \text{ N}$  can be reached with an effective power  $P_e = P_0/2$  of  $10 \mu\text{W}$ . From the numerical simulations we gather that such forces result in a finite minimum of the mode frequency. For the frequency measurement we needed to have a slight differential light force in the laser beam, so that it can excite the axial shear mode. For this we adjusted the intensity maximum of the laser beam to one of the chains, resulting in roughly 6% intensity difference between the rows. The calculated force difference is then approximately  $0.6 \times 10^{-21} \text{ N}$ , from which we expect an increase of the minimal frequency to  $0.32\omega_z$ . This is currently below the measured frequency and is not yet limiting the experiments. Since a lower



mode frequency needs smaller  $\Delta F$  to excite the motion, this future limitation can be prevented by reducing laser power or reducing the intensity difference between the chains.

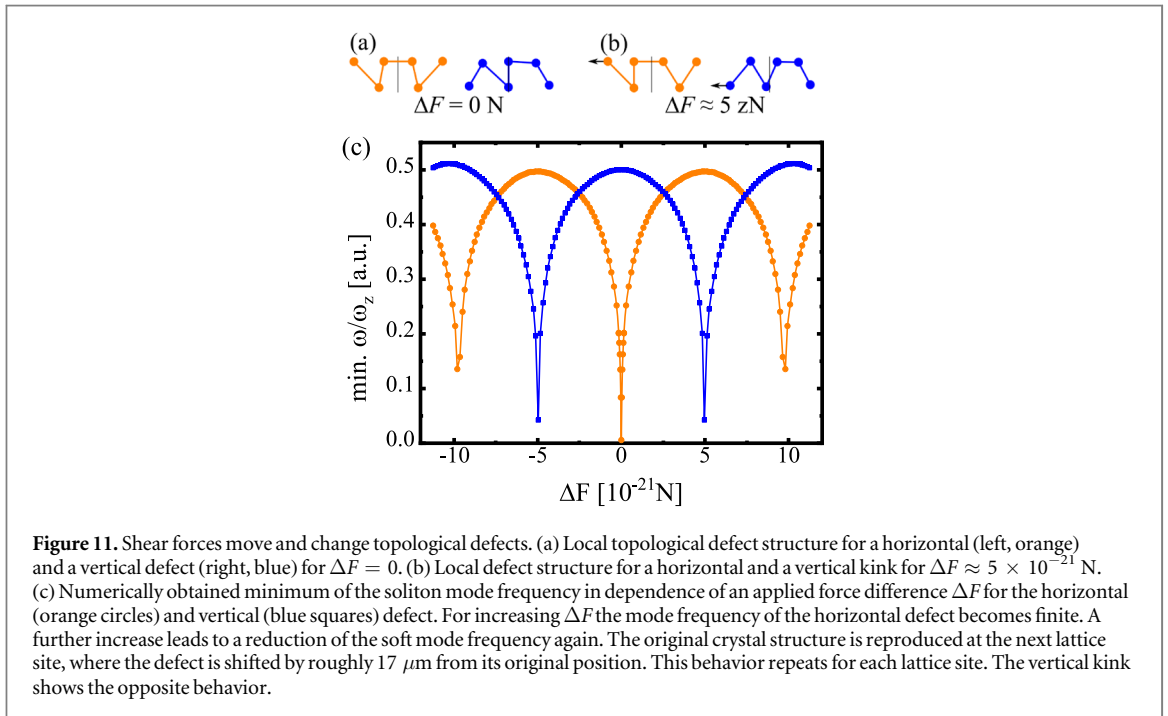
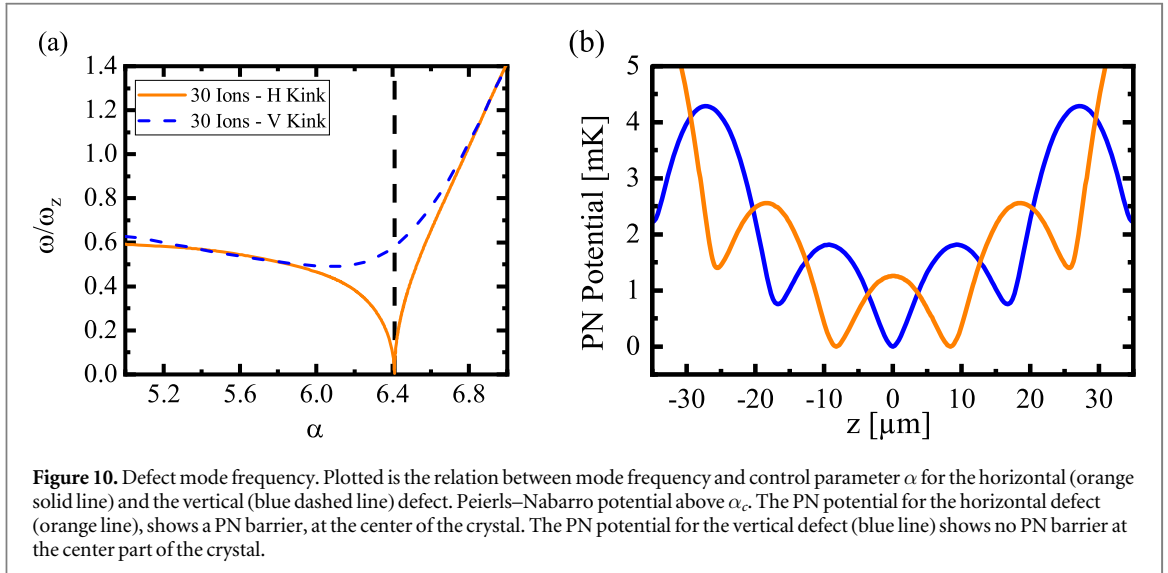
For experiments that require a symmetric crystal, or a low vibrational frequency, it is therefore necessary to symmetrically center the beam onto the ions, minimizing differential light forces.

#### 4. Motion of the topological defect

In this section, we discuss the motion of the topological defect, when the chains are pushed deterministically by differential forces introduced in the previous section. We will look at the motion for both the horizontal and vertical kink, and compare their behavior.

Starting with the frequency of the vibrational defect mode for the vertical kink we find that in contrast to the horizontal topological defect, it does not exhibit a soft mode tending to zero, see figure 10(a). Also, no structural symmetry breaking at the critical point is observed. This can be explained by examining the PN potentials shown in figure 10(b). For  $\alpha > \alpha_c$  the PN potential of the vertical kink has a minimum in the center of the trap, whereas the horizontal kink has a maximum. When the transition is crossed, the vertical kink does not move spontaneously, because the global minimum before the transition is still the global minimum after the transition.

By varying the force difference  $\Delta F$  we push the kink through the crystal; the higher the  $|\Delta F|$  the larger is the displacement of the kink from the center. We find that the local structure of a stable kink configuration changes periodically as a function of  $\Delta F$ , as is shown in figures 11(a) and (b). If  $\Delta F$  is around  $5 \times 10^{-21}$  N, the local structure of a vertical defect looks like a horizontal defect. If the force is increased further to roughly  $10 \times 10^{-21}$  N, the defect moved by roughly  $17 \mu\text{m}$  and the initial local structure is reproduced, but one lattice period away from the initial position. Shown in figure 11(c) is the soft mode frequency, i.e. the lowest frequency of the localized defect mode, against an applied  $\Delta F$ . In this relation a similar periodic behavior is observed.



We find that the minimum mode frequency is low (tending towards zero), whenever the local structure looks like a H defect. The minimum is high (around  $0.5\omega_z$ ), when the defect is locally similar to the V defect. By starting with an H defect we observe the opposite behavior. This explains, why a differential force  $\Delta F$  ‘destroys’ the soft mode. The local structure changes from an H defect to a V defect, which does not exhibit a soft mode.

Even though these calculations are done for static configurations, in a slow dynamic process, the ions will move along the same trajectory. Therefore, we conclude that the motion of the extended kink in an ion Coulomb crystal is accompanied by a change in the nature of the defect, which can be seen both in its local structure and in the frequency of the vibrational defect mode. Note that the vertical and horizontal defect are still distinguishable by their number of ions per chain. Only locally they shift into each other.

## 5. Discussion and conclusion

In this work, we investigated atomic friction in self-organized ion Coulomb crystals with topological defects, with special attention given to the position of the defect and how it can be changed. The findings are of direct relevance to research that aims to exploit topological defects for quantum information processing [29]. The spectroscopic method, introduced in [19] and explained in detail in this publication, for probing the vibrational

mode of the topological defect with the help of amplitude modulated laser light is an alternative to typical excitation methods, such as parametric excitation via rf modulation [31, 46]. It offers the advantage of being mode sensitive as the laser intensity distribution can be matched to fit a specific motional mode vector, providing a tool for investigating mode mixing in ion Coulomb crystals.

We numerically investigated the influence of symmetry breaking forces, anharmonicities and micromotion, present in ion trapping experiments, on the crystal structure, which in turn changes the kink soliton position and the kink soliton frequency. The sensitivity of the kink to these effects, can be used to characterize even small disturbances in ion trap experiments. In the case of differential forces across the Coulomb crystal, with typical length scale of approximately  $20 \mu\text{m}$ , a frequency shift  $\Delta\nu$  near  $\Delta F = 0$  has a sensitivity of  $\Delta F/\Delta\nu \approx 1.4 \times 10^{-26} \text{ N Hz}^{-1}$ . Even with the current frequency measurement uncertainty of around 400 Hz differential forces of just  $6 \times 10^{-24} \text{ N}$  could be measured, if the crystal can be cooled to sufficient temperatures. This is another signature how sensitive ion Coulomb crystals are with respect to external forces [47].

We were able to fit the experimental results, obtained in a previously used milled prototype trap [39], closely to simulations which include an additional third-order term in the axial potential. The additional nonlinear term is most likely due to the fabrication method. In the new high-precision, laser-cut ion trap [44], an influence of a similar higher order term was not observed. We also investigated the influence of axial micromotion on the crystal configuration and found that, for experimentally observed values of micromotion, the ion positions are not changed in comparison to simulations using no axial micromotion. It is known that mode frequencies obtained from the ponderomotive approximation deviate by a few percent to frequencies obtained from the full dynamics [45]. However, as the relative experimental resolution of our method is currently around 4%, it is unlikely that we could resolve this frequency difference. In future experiments, the resolution can be improved, in which case using the Floquet–Lyapunov approach to calculate the mode frequencies might be necessary.

With the help of laser light forces the topological defect can be moved through the crystal deterministically. This effect is similar to force gradients due to anharmonic potentials, when probabilistic directed transport was observed [31]. We observed a periodic change in the local structure of the kink as a function of the applied external force, demonstrating that, as the kink moves through the chain, it alternates between two types of stable kinks, one with a gapped vibrational mode (vertical kink) and the other with a soft vibrational mode (horizontal kink). As the movement of the defect constitutes the sliding of both ion chains in this system, this represents a first step towards dynamic friction investigations of the presented tribological system.

In future experiments, the crystal temperature can be lowered to the  $\mu\text{K}$  regime, using dark resonances [48–50], Sisyphus cooling [51] via polarization gradients or narrow transitions [39, 44] in other ion species implanted into the crystal. Lower temperatures might enable friction experiments in the quantum regime [52]. Furthermore, investigations of crystals of higher dimensions or homogeneously spaced crystals can help in translating the results from our model system to solid state sliding systems. Here the versatility of ion traps can help, as either designed anharmonic potentials or ring traps [53] could be used to create such scenarios.

## Acknowledgments

We thank Jonas Keller for many useful discussions and valuable help with the experiment control. We thank Lars Timm for carrying out numerical calculations and for comments on the manuscript. This work was supported by the DFG through grant ME 3648/1-1.

## Appendix

### A.1. Offset of the primary gap in the hull function

In figure 3(c) for  $\alpha = 6.6$ , the central gap is offset from  $z_{j,0} = 0$  and  $z_j = 0$ . This is due to broken mirror symmetry of the system. The topological defect is already in one of the central PN potential wells, see figure 2(c). The defect is not situated at the position of the PN barrier, and neither are the ions, for which we calculate the hull function. Before a slip can occur, the ions first need to move in either axial direction, which is the reason why the primary gap is not at  $z_{j,0} = 0$ . Due to the inhomogeneity the localized defect moves towards one central minimum (towards the right in the figures), instead of the other, were the PN potential becomes steeper. This explains why the gap is not symmetric around  $z_j = 0$ .

### A.2. Simulation overview

Throughout this paper we used different numerical calculations depending on the issue at hand. The following list and table A1 gives a short description of each method and where it was used.

**Table A1.** Overview showing in which figure each type of numerical calculation is used. EOM: equations of motion.

| Dimensions | EOM solved for              | Temperature | Used in figures                |
|------------|-----------------------------|-------------|--------------------------------|
| 2          | Time-averaged rf potential  | 0 K         | 2(b), 3(b), 5(b), 7, 9, 10, 11 |
| 3          | Time-averaged rf potential  | >0 K        | 5(b), 6                        |
| 3          | Time-dependent rf potential | 0 K         | 8                              |

- Two-dimensional calculation using time-averaged rf potentials without temperature. This code solves the equations of motion of all ions in the ponderomotive approximation of the rf field under high damping to get the equilibrium positions  $\mathbf{q}(0)$ .  $T = 0$  K. It also allows for the diagonalization of Hessian matrix for a given  $\mathbf{q}(0)$ , resulting in the mode spectrum of the crystal, and the calculation of the hull functions.
- Three-dimensional calculation using time-averaged rf potentials with temperature. This code solves the Langevin equations for all ions in the ponderomotive approximation for the rf field in three dimensions under experimentally realistic damping. The temperature is introduced with a stochastic force. Vibrational mode frequencies are obtained with Fourier transformation of the resulting ion trajectories.
- Three-dimensional calculation of time-dependent rf potentials without temperature. This code solves the Mathieu equations [43] for all ions in three-dimensions under damping. The average positions of the ions are taken as the equilibrium positions for comparison with the ponderomotive approximation.

## ORCID iDs

T E Mehlstäubler  <https://orcid.org/0000-0003-3430-4689>

## References

- [1] Vanossi A, Manini N, Urbakh M, Zapperi S and Tosatti E 2013 *Mod. Phys. Rev.* **85** 529
- [2] Kudernac T, Ruangsapichat N, Parschau M, Maciá B, Katsonis N, Harutyunyan S R, Ernst K H and Feringa B L 2011 *Nature* **479** 208
- [3] Kühner F, Morfill J, Neher R A, Blank K and Gaub H E 2007 *Biophys. J.* **92** 2491–7
- [4] Ward A, Hilitski F, Schwenger W, Welch D, Lau A, Vitelli V, Mahadevan L and Dogic Z 2015 *Nat. Mater.* **14** 583–8
- [5] García-Mata I, Zhirov O and Shepelyansky D 2007 *Eur. Phys. J. D* **41** 325–30
- [6] Benassi A, Vanossi A and Tosatti E 2011 *Nat. Commun.* **2** 236
- [7] Pruttivarasin T, Ramm M, Talukdar I, Kreuter A and Häffner H 2011 *New J. Phys.* **13** 075012
- [8] Mandelli A, Vanossi A and Tosatti E 2013 *Phys. Rev. B* **87** 195418
- [9] Fogarty T, Cormick C, Landa H, Stojanović V M, Demler E and Morigi G 2015 *Phys. Rev. Lett.* **115** 233602
- [10] Braun O M and Kivshar Y S 2004 *The Frenkel–Kontorova Model: Concepts, Methods, and Applications* (Berlin: Springer)
- [11] Aubry S 1983 *Physica D* **7** 240–58
- [12] Sharma S, Bergersen B and Joos B 1984 *Phys. Rev. B* **29** 6335–40
- [13] Braiman Y, Baumgarten J, Jortner J and Klafter J 1990 *Phys. Rev. Lett.* **65** 2398
- [14] Bylinskii A, Gangloff D and Vuletić V 2015 *Science* **348** 1115–8
- [15] Gangloff D, Bylinskii A, Counts I, Jhe W and Vuletić V 2015 *Nat. Phys.* **11** 915–9
- [16] Counts I, Gangloff D, Bylinskii A, Hur J, Islam R and Vuletić V 2017 *Phys. Rev. Lett.* **119** 043601
- [17] Bylinskii A, Gangloff D, Counts I and Vuletić V 2016 *Nat. Mater.* **15** 717–21
- [18] Matsukawa H and Fukuyama H 1994 *Phys. Rev. B* **49** 17286
- [19] Kiethe J, Nigmatullin R, Kalincev D, Schmirander T and Mehlstäubler T 2017 *Nat. Commun.* **8** 15364
- [20] Mielenz M, Brox J, Kahra S, Leschhorn G, Albert M, Schätz T, Landa H and Reznik B 2013 *Phys. Rev. Lett.* **110** 133004
- [21] Pyka K et al 2013 *Nat. Commun.* **4** 2291
- [22] Ulm S et al 2013 *Nat. Commun.* **4** 2290
- [23] Ejtemaee S and Haljan P 2013 *Phys. Rev. A* **87** 051401
- [24] Kumar S and Li M S 2010 *Phys. Rep.* **486** 1–74
- [25] Sieradzan A K, Niemi A and Peng X 2014 *Phys. Rev. E* **90** 062717
- [26] del Campo A, De Chiara G, Morigi G, Plenio M and Retzker A 2010 *Phys. Rev. Lett.* **105** 075701
- [27] Silvi P, Morigi G, Calarco T and Montangero S 2016 *Phys. Rev. Lett.* **116** 225701
- [28] De Chiara G, del Campo A, Morigi G, Plenio M B and Retzker A 2010 *New J. Phys.* **12** 115003
- [29] Landa H, Marcovitch S, Retzker A, Plenio M and Reznik B 2010 *Phys. Rev. Lett.* **104** 043004
- [30] Landa H, Retzker A, Schätz T and Reznik B 2014 *Phys. Rev. Lett.* **113** 053001
- [31] Brox J, Kiefer P, Bujak M, Schätz T and Landa H 2017 *Phys. Rev. Lett.* **119** 153602
- [32] Keller J, Burgermeister T, Kalincev D, Didier A, Kulosa A, Nordmann T, Kiethe J and Mehlstäubler T 2018 arXiv:1803.08248
- [33] Herschbach N, Pyka K, Keller J and Mehlstäubler T E 2012 *Appl. Phys. B* **107** 891–906
- [34] Landa H, Reznik B, Brox J, Mielenz M and Schätz T 2013 *New J. Phys.* **15** 093003
- [35] Partner H L, Nigmatullin R, Burgermeister T, Pyka K, Keller J, Retzker A, Plenio M B and Mehlstäubler T E 2013 *New J. Phys.* **15** 103013
- [36] Nigmatullin R, del Campo A, De Chiara G, Morigi G, Plenio M B and Retzker A 2016 *Phys. Rev. B* **93** 014106
- [37] Partner H L, Nigmatullin R, Burgermeister T, Keller J, Pyka K, Plenio M B, Retzker A, Zurek W H, del Campo A and Mehlstäubler T E 2015 *Physica B* **460** 114–8



- [38] Vanossi A, Röder J, Bishop A and Bortolani V 2003 *Phys. Rev. E* **67** 016605
- [39] Pyka K, Herschbach N, Keller J and Mehlstäubler T E 2014 *Appl. Phys. B* **114** 231–41
- [40] Skeel R D and Izaguirre J A 2002 *Mol. Phys.* **100** 3885–91
- [41] Gudjons T, Seibert P and Werth G 1997 *Appl. Phys. B* **65** 57–62
- [42] Landa H, Drewsen M, Reznik B and Retzker A 2012 *New J. Phys.* **14** 093023
- [43] Ghosh P 1995 *Ion Traps* (Oxford: Clarendon)
- [44] Keller J, Kalincev D, Burgermeister T, Kulosa A, Didier A, Nordmann T, Kiethe J and Mehlstäubler T 2017 arXiv:1712.02335
- [45] Kaufmann H, Ulm S, Jacob G, Poschinger U, Landa H, Retzker A, Plenio M and Schmidt-Kaler F 2012 *Phys. Rev. Lett.* **109** 263003
- [46] Ibaraki Y, Tanaka U and Urabe S 2011 *Appl. Phys. B* **105** 219–23
- [47] Biercuk M J, Uys H, Britton J W, VanDevender A P and Bollinger J J 2010 *Nat. Nanotechnol.* **5** 646–50
- [48] Morigi G, Eschner J and Keitel C H 2000 *Phys. Rev. Lett.* **85** 4458
- [49] Lechner R, Maier C, Hempel C, Jurcevic P, Lanyon B P, Monz T, Brownnutt M, Blatt R and Roos C F 2016 *Phys. Rev. A* **93** 053401
- [50] Scharnhorst N, Cerrillo J, Kramer J, Leroux I D, Wübbena J B, Retzker A and Schmidt P O 2018 *Phys. Rev. A* **98** 023424
- [51] Ejtemaee S and Haljan P 2017 *Phys. Rev. Lett.* **119** 043001
- [52] Zanca T, Pellegrini F, Santoro G E and Tosatti E 2018 *Proc. Natl Acad. Sci.* **115** 3547–50
- [53] Li H K et al 2017 *Phys. Rev. Lett.* **118** 053001



## 4 P3: Finite-temperature spectrum at the symmetry-breaking linear to zigzag transition

**Authors:** J. Kiethe, L. Timm, H. Landa, D. Kalincev, G. Morigi, and T. E. Mehlstäubler

**Journal:** Physical Review B

**DOI:** 10.1103/PhysRevB.103.104106

**Author contributions:** The experiment was initiated and led by T.E.M. D.K. and J.K. designed the experiment with input from T.E.M. D.K. and J.K. carried out the experiments and performed the data analysis. J.K. and L.T. carried out the simulations. H.L. devised the analytical model. J.K. carried out the calculations. All authors contributed to the discussion of results and participated in the manuscript preparation.

**Copyright:** © The Authors 2021. Published by American Physical Society. This article is licensed under a Creative Commons Attribution 4.0 International License.

**Finite-temperature spectrum at the symmetry-breaking linear to zigzag transition**Jan Kiethel,<sup>1</sup> Lars Timm,<sup>2</sup> Haggai Landa,<sup>3,4</sup> Dimitri Kalincev<sup>5</sup>,<sup>1</sup> Giovanna Morigi<sup>5</sup>, and Tanja E. Mehlstäubler<sup>1,6,\*</sup><sup>1</sup>*Physikalisch-Technische Bundesanstalt, Bundesallee 100, 38116 Braunschweig, Germany*<sup>2</sup>*Institut für Theoretische Physik, Leibniz Universität Hannover, Appelstr. 2, 30167 Hannover, Germany*<sup>3</sup>*Institut de Physique Théorique, Université Paris-Saclay, CEA, CNRS, 91191 Gif-sur-Yvette, France*<sup>4</sup>*IBM Quantum, IBM Research Haifa, Haifa University Campus, Mount Carmel, Haifa 31905, Israel*<sup>5</sup>*Theoretische Physik, Saarland University, Campus E26, 66123 Saarbrücken, Germany*<sup>6</sup>*Institut für Quantenoptik, Leibniz Universität Hannover, Welfengarten 1, 30167 Hannover, Germany*

(Received 21 December 2020; revised 18 February 2021; accepted 18 February 2021; published 19 March 2021)

We investigate the normal-mode spectrum of a trapped ion chain at the symmetry-breaking linear to zigzag transition and at finite temperatures. For this purpose, we modulate the amplitude of the Doppler cooling laser to excite and measure mode oscillations. The expected mode softening at the critical point, a signature of the second-order transition, is not observed. Numerical simulations show that this is mainly due to the finite temperature of the chain. Inspection of the trajectories suggest that the thermal shifts of the normal-mode spectrum can be understood by the ions collectively jumping between the two ground-state configurations of the symmetry-broken phase. We develop an effective analytical model, which allows us to reproduce the low-frequency spectrum as a function of the temperature and close to the transition point. In this model, the frequency shift of the soft mode is due to the anharmonic coupling with the high-frequency modes of the spectrum, acting as an averaged effective thermal environment. Our study could prove important for implementing ground-state laser cooling close to the critical point.

DOI: [10.1103/PhysRevB.103.104106](https://doi.org/10.1103/PhysRevB.103.104106)**I. INTRODUCTION**

Ion Coulomb crystals are an unusual form of condensed matter, where crystalline order emerges from the interplay between Coulomb repulsion and the external trapping potential, while the temperature is controlled by means of lasers [1]. These properties make them versatile and controllable systems [1,2], which are among the most prominent platforms for quantum computation [3–10] and for the simulation of the equilibrium and out-of-equilibrium dynamics of many-body systems [11–23].

Amongst others, the Kibble-Zurek mechanism [24–26] and creation of topological defects have been demonstrated [27–30]. Two widely discussed transitions are the linear to zigzag [31–34] and the pinning to sliding (Aubry) transition [35–37]. These were shown to be second-order phase transitions [33,38] that exhibit a soft mode with vanishing frequency at a critical point. The system, however, is critical solely at zero temperature. Therefore, the observation of critical behavior requires one to characterize and understand finite temperature effects at the transition, such as the size

of the crossover region due to temperature and how thermal excitations modify the normal mode spectrum.

The frequency spectrum at zero temperature is well described by the harmonic crystal approximation. Deviations to this analytical solution and, in particular, finite frequencies close to the critical point have been observed for the soft mode of the Aubry-type transition in trapped ion chains, at a temperature of around 1 mK [12]. Here, we focus on the experimentally more accessible linear to zigzag transition and investigate the coupling of the soft mode to the thermal phonon environment. We develop a theoretical model that allows one to reproduce the presented spectroscopic measurements by means of a harmonic chain, whose normal-mode spectrum at low frequencies results from the temperature-dependent coupling with vibrational modes at high frequencies. In this sense, the high-frequency modes can be considered a thermal phonon environment. We discuss this result in connection to earlier works [39,40] that described finite temperature effects in terms of an effective shift of the transition point. Our findings deepen the understanding of the complex dynamics of ion Coulomb crystals. They could prove important, for instance, for laser cooling the linear ion chain to the ground state in the vicinity of the transition.

This paper is organized as follows: In Sec. II, we briefly review the linear to zigzag transition. In Sec. III, we present our experimental methods and results of vibrational mode measurements, using resonant light force modulation. Subsequently, in Sec. IV we compare our findings to molecular dynamics simulations. In Sec. V, we discuss a simplified analytical model which allows one to gain insight into the

\*Corresponding author: [tanja.mehlstaebler@ptb.de](mailto:tanja.mehlstaebler@ptb.de)

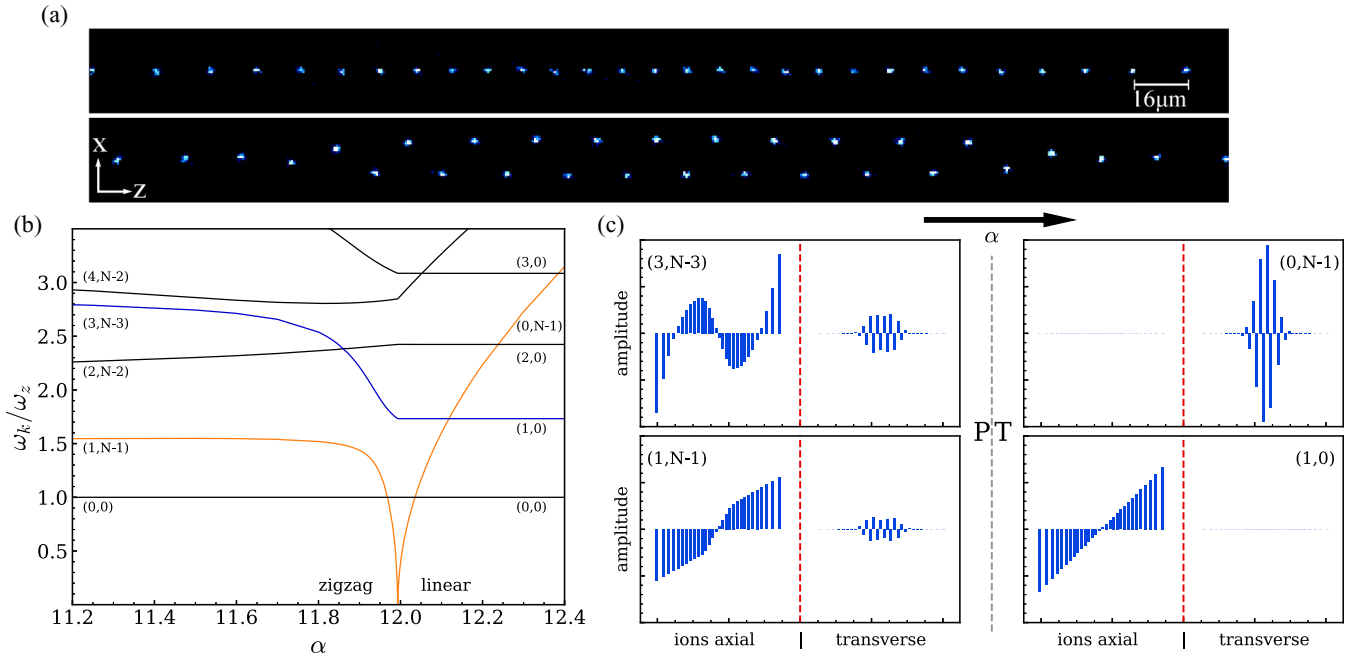


FIG. 1. (a) Experimental pictures of the linear chain (top) and of the zigzag configuration (bottom). The crystals are formed by 30 laser-cooled  $\text{Yb}^+$  ions in a linear Paul trap. The images were taken under an angle of  $45^\circ$  to the crystal plane and focused on the bottom row of the zigzag crystal. The rightmost ion for the linear chain is out of view. (b) Normal modes as a function of the aspect ratio  $\alpha$  and in the vicinity of the linear to zigzag transition at  $\alpha_c \approx 12.0$  for  $N = 30$ . The modes are evaluated in the theoretical limit  $T = 0$ . For  $\alpha < \alpha_c$ , the ions form a zigzag structure, for  $\alpha > \alpha_c$  a linear chain. The vanishing of the zigzag mode frequency at  $\alpha_c$  signals the phase transition (PT) point. The notation  $(n, p)$  indicates the number of axial and transverse nodal points of the corresponding mode vector. (c) Normal-mode vector for the breathing and the zigzag mode below [above] the phase transition with nodal points  $(3, N-3)$  [(1,0)] and  $(1, N-1)$  [(0, N-1)], respectively. PT indicates the phase transition. The third direction  $y$  is not shown, as it has zero amplitudes for all ions in these modes. Here, the axial trapping frequency is in the range of  $\omega_z \approx 2\pi \times (20 - 35)$  kHz. The transverse trapping frequency is chosen such that  $\alpha$  varies in the interval [11.0, 12.5].

temperature dependence of the spectroscopic measurements. In Sec. VI, the conclusions are drawn. The Appendices provide supplementary material to the studies presented in Secs. IV and V.

## II. THE LINEAR-ZIGZAG TRANSITION

We consider  $N$  ions with charge  $e$  and mass  $m$ , which are confined by a linear Paul trap. The trap potential is described in ponderomotive approximation by three trapping frequencies  $\omega_z$ ,  $\omega_x$ , and  $\omega_y$ . The total potential energy  $V$  is the sum of the trap confinement and of the unscreened Coulomb interaction between the ions,

$$V = \sum_{i=1}^N \frac{m}{2} (\omega_x^2 x_i^2 + \omega_y^2 y_i^2 + \omega_z^2 z_i^2) + \frac{e^2}{4\pi\epsilon_0} \sum_{i=1}^N \sum_{j<i}^N |\mathbf{r}_i - \mathbf{r}_j|^{-1}, \quad (1)$$

where  $\mathbf{r}_i = (x_i, y_i, z_i)^T$  denotes the position of the ion  $i$  ( $i = 1, \dots, N$ ) and  $\epsilon_0$  is the vacuum permittivity. For later convenience, we introduce the vector  $\mathbf{u} = (x_1, x_2, \dots, x_N, y_1, y_2, \dots, y_N, z_1, z_2, \dots, z_N)^T$ , which gives the configuration of the crystal.

At sufficiently low temperature, the ions localize at the equilibrium positions  $\mathbf{u}(0)$  of the potential  $V$ , for which the

equations  $\partial V / \partial u_j = 0 \forall j$  hold. In this configuration, the dynamics of the chain is characterized by the matrix  $K'$ , with elements

$$K'_{ij} = \left. \frac{\partial^2 V}{\partial u_i \partial u_j} \right|_{\mathbf{u}(0)}. \quad (2)$$

For stable equilibrium,  $K'$  has finite and positive eigenvalues. In the rest of this paper, we choose  $\omega_z < \omega_x < \omega_y$ , focusing particularly on the aspect ratio  $\alpha = \omega_x / \omega_z$  for which the ions can either form a one-dimensional crystal along the  $z$  axis, the linear chain, or form a two-dimensional crystal in the form of a zigzag configuration on the  $x - z$  plane with two degenerate ground states [41,42].

Figure 1(a) displays an experimental photo of a linear and of a zigzag chain of 30 ions. The two structures are separated by the critical value of the aspect ratio  $\alpha_c \approx 12$ . A numerical estimate of the scaling of the transition point with the number of ions gives  $\alpha_c(N) \sim 0.556N^{0.915}$ , see Refs. [32,43,44], which gives an approximate location of the transition point [31]. The shift of the transition point due to quantum fluctuations has been determined in Refs. [45,46].

The linear to zigzag instability is a continuous phase transition in the thermodynamic limit, corresponding to letting  $N \rightarrow \infty$  and to rescaling the trap frequencies with  $N$  to keep the critical aspect ratio  $\alpha_c$  constant [33,47]. It is associated with breaking of reflection symmetry about the  $z$  axis (for

$\omega_x = \omega_y$ , the broken symmetry is rotational and the transition is characterized by a Goldstone mode) [33]. As for ferromagnetism in one dimension, these properties are strictly valid in the limit of  $T = 0$ , while at finite temperature the transition becomes a crossover. Let us now make our statement more precise. In our case, where laser cooling of the chain can be modeled by an effective thermal reservoir [48], one can use a canonical ensemble to model the properties at the steady state. A phase transition, like the linear-zigzag structural instability, is then identified in the thermodynamic limit by discontinuities in the derivatives of the free energy. The linear-zigzag instability can be mapped to the Ising model for ferromagnetism, where the phase transition is present only at zero temperature and is a quantum phase transition [33,49,50]. At finite but low temperatures, when  $k_B T$  is smaller than the gap between the ground and the first excited state of the quantum model, the properties are universal [49]. At higher temperatures, such as the ones we consider in this paper, the transition becomes nonuniversal and abrupt changes and power-law scaling characteristics of a phase transition are replaced by a smooth behavior which we here denote by crossover (and shall not be confused with the crossover due to finite-size effects) [50].

To understand the effect of temperatures on the vibrational spectrum across the linear to zigzag transition and in a finite chain, we first discuss the normal-mode spectrum at  $T = 0$ . The normal-mode spectrum is determined by assuming that the ion displacements due to thermal noise are small in comparison to the equilibrium ion distances. The normal-mode frequencies are related to the eigenvalues  $\lambda_j$  of the matrix  $K'$  by the relation  $\omega_j = \sqrt{\lambda_j/m}$  ( $j = 1, \dots, 3N$ ). The corresponding mode vectors are given by the columns of the dynamical matrix  $\lambda_{ij}$  that diagonalizes  $K'$  and the mode amplitudes are denoted as  $\Theta_j$ . We use the notation  $(n, p)$  to identify the mode vectors by the number of nodal points (phase flips between ions) along the axial ( $n$ ) and transverse direction ( $p$ ).<sup>1</sup> For example, the three lowest axial modes in the linear chain are denoted by  $(0,0)$ ,  $(1,0)$ , and  $(2,0)$ , while the lowest three transverse modes are  $(0, N-1)$ ,  $(0, N-2)$ ,  $(0, N-3)$ . The lowest normal mode frequencies for  $N = 30$  are displayed in Fig. 1(b) as a function of the aspect ratio  $\alpha$  across the linear to zigzag transition.

At the transition point, the frequency of one normal mode vanishes. In the linear chain, this mode is the zigzag mode and has a purely transverse oscillation with  $(0, N-1)$  nodal points, see Fig. 1(c). In the thermodynamic limit, the zigzag mode of the linear chain is the soft mode of the phase transition [33]. It is interesting to analyze the property of the eigenmode at lowest frequency as a function of the aspect ratio  $\alpha$ . While in the linear chain ( $\alpha > \alpha_c$ ) it corresponds to the zigzag mode, in the symmetry-broken (zigzag) phase at  $\alpha < \alpha_c$ , the eigenmode at lowest frequency gains an axial nodal point and becomes the new breathing mode  $(1, N-1)$  of the zigzag configuration. The axial breathing mode  $(1,0)$  of the linear chain, instead,

gains two axial nodes, as well as a transverse zigzag pattern to become the  $(3, N-3)$  mode.

In the following sections, we will denote the linear chain by 1D phase and the zigzag crystal by 2D phase. We remark that the term zigzag mode refers to the mode with  $(0, N-1)$  nodal points in the 1D phase and  $(1, N-1)$  nodal points in the symmetry-broken, 2D phase. Moreover, the breathing mode is the mode with  $(1,0)$  nodal points in the 1D phase and  $(3, N-3)$  nodal points in the 2D phase.

In the rest of this paper, we analyze how the normal mode spectroscopy at the structural transition is modified at finite temperatures.

### III. MEASUREMENT OF VIBRATIONAL MODES

In this section, we describe our experimental method for measuring vibrational mode frequencies that makes use of a single laser beam with frequency near resonant to the Doppler cooling transition. We then present and discuss our measurements of the lowest axial modes near the linear to zigzag transition. This method was originally introduced in Ref. [12].

#### A. Setup

To have a well-defined ordered structure, we trap  $N = 30$   $^{172}\text{Yb}^+$  ions in a linear Paul trap with high control of the electrical fields [51,52]. The axial trapping frequency is in the range of  $\omega_z \approx 2\pi \times (20 - 35)$  kHz. The transverse trapping frequency is in the range of  $\omega_x \approx 2\pi \times (220 - 440)$  kHz, depending on the chosen trapping ratio  $\alpha$ . All ions are illuminated by a linearly polarized laser with a central wavelength of 369.5 nm addressing the  $^2S_{1/2} \leftrightarrow ^2P_{1/2}$  transition in  $\text{Yb}^+$  and cooling the ions close to the Doppler cooling temperature of  $T_D = 0.5$  mK. As shown in Fig. 2, the laser beam forms an angle of about  $\theta = 25^\circ$  with the axial direction of the ion crystal and an angle of about  $\varphi = 45^\circ$  with the transverse direction. We denote its wave vector as  $\mathbf{k}_1$ , which we use in the subsequent text to identify the laser beam itself. The beam has an elliptic shape with waists of approximately 2.6 mm in the horizontal and 80  $\mu\text{m}$  in the vertical direction, resulting in an almost uniform illumination of a 400  $\mu\text{m}$  times 20  $\mu\text{m}$  ion crystal in the  $z$ - $x$  plane. Typical laser powers in the subsequent measurements are  $P_1 = 1$  mW, corresponding to a saturation of  $s_1 \approx 1.75$  at the beam center (saturation power of  $\mathbf{k}_1$  is  $P_{1,s} \approx 570$   $\mu\text{W}$ ).

We also employ a second laser beam at the same wavelength and with the same angles to the crystal that is focused to a beam waist of about 80  $\mu\text{m}$  in both vertical and horizontal directions, addressing a smaller region of the crystal. Its wave vector is denoted by  $\mathbf{k}_2$ . The beam is amplitude modulated to excite the crystal's normal modes. The amplitude modulation is added by applying a sine wave with frequency  $\omega_e$  to the rf amplitude of an acousto-optic modulator used as a fast shutter. The modulation of the power is given by

$$P_2 = \frac{P_m}{2}[1 + \cos(\omega_e t)],$$

where  $P_m$  is the maximum power in the beam. The saturation of  $\mathbf{k}_2$  at the beam center is then

$$s_2 = s_m[1 + \cos(\omega_e t)],$$

<sup>1</sup>This is not a unique identification. In fact, due to the finite size some modes have the same number of nodal points. A unique identification is achieved, for instance, by also specifying the mode frequency.

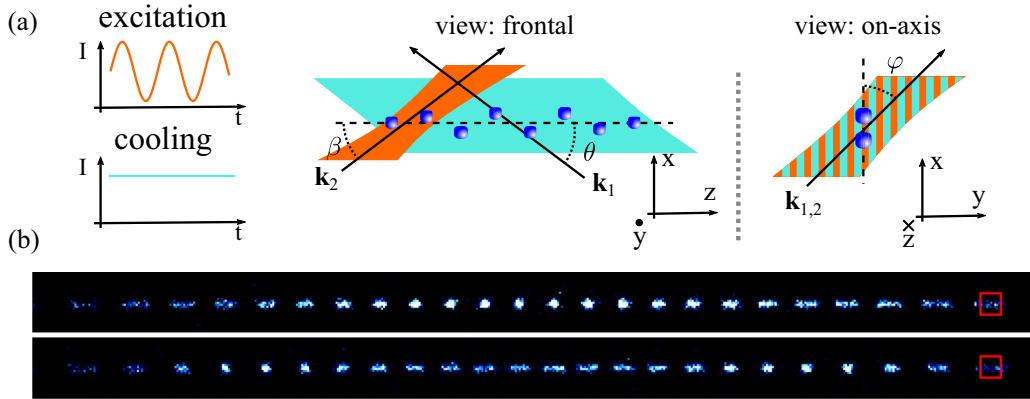


FIG. 2. Resonant light force modulation. (a) Schematic laser beam setup. The ion crystal is almost uniformly illuminated by a cooling beam  $\mathbf{k}_1$  (cyan). The laser beam illuminates the crystals axial extent ( $z$ ) under an angle of  $\theta \approx 25^\circ$  and the transverse extent ( $x$ ) under an angle of  $\varphi \approx 45^\circ$ . An excitation beam  $\mathbf{k}_2$  (orange) is focused down to only a fraction of the crystal. It hits the crystal  $z$  axis under an angle  $\beta \approx 25^\circ$  and the  $x$  axis under the same angle  $\varphi$  as the cooling beam. The excitation beam is amplitude modulated, resulting in a sinusoidal force. The beam sizes are not to scale. (b) Example crystal photos with excited normal modes. Images taken with an EMCCD camera when the modulation frequency of the excitation laser is resonant with a normal mode. Exposure time: 100 ms;  $P_m \approx 20 \mu\text{W}$ . Top: Breathing mode/(1,0). Bottom: (2,0). Red squares represent possible regions of interest to record fluorescence of single ions.

where

$$s_m = \frac{P_m/2}{P_{2,s}},$$

with saturation power  $P_{2,s} \approx 38 \mu\text{W}$  of  $\mathbf{k}_2$ . The total saturation of an ion at the center of the beams is then  $s = s_1 + s_m + s_m \cos(\omega_e t)$ . The ion fluorescence is imaged via a lens system of  $N/A = 0.2$  and recorded by an electron-multiplying (EM) CCD camera, which can resolve individual ions.

### B. Method

We excite the crystal's collective motion with the help of the amplitude modulated cooling laser. Both cooling lasers  $\mathbf{k}_1$  and  $\mathbf{k}_2$  are continuously incident on the ions during the measurement and both exert a constant light force on the crystal, that shifts the minimum of the trap potential. The amplitude modulated laser adds an oscillating force  $F_m$  with excitation frequency  $\omega_e$ . This oscillating force is roughly linear, if  $s_m$  is smaller than  $s_1$ . For multiple ions, the saturations  $s_2$  and  $s_1$  will depend on the ion positions with respect to the laser beam center. Specifically, the saturation power  $P_s(\mathbf{r}_i)$  will depend on the position of the  $i$ th ion.

In principle, all normal modes can be excited by means of this technique. In the measurements we present below, the waist of laser  $\mathbf{k}_2$  was focused to only  $80 \mu\text{m}$ . It illuminates several ions at the same time, as illustrated in Fig. 2(a). This prevented the excitation of modes with a higher number of nodal points due to the small overlap of their mode vector with the laser intensity profile, such as the zigzag mode in the 1D phase, which has  $N-1$  nodal points. We note that the excitation of an arbitrarily chosen mode can be realized by implementing single ion addressing.

On resonance, the amplitude of the driven mode increases linearly with  $F_m$  for small oscillations around the equilibrium positions. In combination with a constant linear damping  $\gamma$  due to laser cooling of  $\mathbf{k}_1$ , a steady state with a constant, frequency-dependent mode amplitude  $\Theta_j(\omega_e)$  can be reached

after several oscillations. To detect an excitation, we record the ions fluorescence with an EMCCD over an exposure time of typically 100 ms. This is long compared to the normal-mode oscillation periods, which are on the order of the center-of-mass oscillation period of about  $40 \mu\text{s}$ . Therefore, light from all possible ion positions during the oscillations is recorded, leading to an apparent increase of the ions' size at the resonance  $\omega_e \approx \omega_j$ . The imaged spatial extent of each ion  $i$  is proportional to the amplitude of the driven normal mode and the ion vector element of the corresponding mode vector  $\lambda_{ij}$ . The resonance frequency is found by identifying the frequency at the maximum amplitude of the ion oscillation. An experimental photo of the excited (1,0) mode and (2,0) mode in the 1D phase is shown in Fig. 2(b), for which we used  $P_m \approx 20 \mu\text{W}$  ( $s_m \approx 0.53$  for an ion at the beam center). Similar to the ion amplitude, the velocity of the ions increases on resonance, leading to a drop in fluorescence due to the Doppler shift. For a single ion, this decrease in fluorescence can be measured with a photomultiplier tube and enables one to identify the motional resonance. The described method is similar to what has been employed in dusty plasmas to measure acoustic waves [53,54].

### C. Experimental results

We measured several mode frequencies near the linear to zigzag transition in two experiment series, with two different modulation powers:  $P_m^{(A)} = 20 \mu\text{W}$  (A) and  $P_m^{(B)} = 6 \mu\text{W}$  (B).

For measurement run (A), we determined the center frequency  $\omega_j$  of any resonance by scanning the excitation frequency  $\omega_e$  manually and searching for the maximum amplitude of the ions for the excited mode. The uncertainties were estimated by finding a region in which the amplitude of the excitation was still maximal. The width of this region was taken as the error of the measurement, with typical values of about 100 Hz to 300 Hz for each resonance. The power of the excitation laser was set to  $P_m^{(A)} = 20 \mu\text{W}$ , chosen such

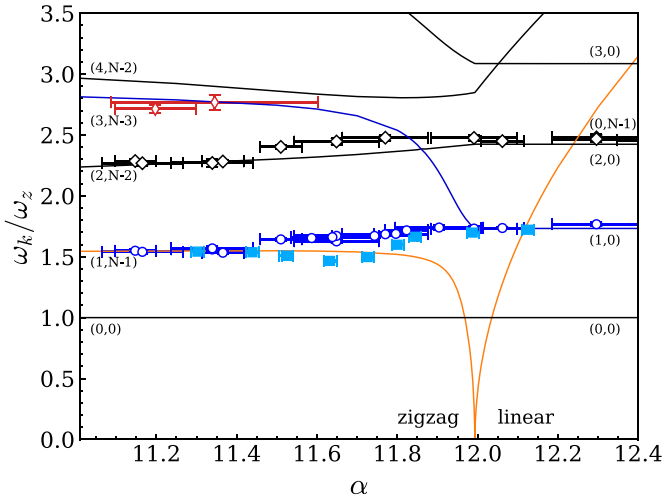


FIG. 3. Low-frequency spectrum as a function of the aspect ratio  $\alpha$ . The solid lines are the modes of the harmonic crystal at  $T = 0$ , the symbols refer to the experimental measurements. Experimental data from series (A) as empty symbols (blue circles, black diamonds, red thin diamonds) with  $P_m^{(A)} = 20 \mu\text{W}$  and series (B) as filled symbols (light blue squares) with  $P_m^{(B)} = 6 \mu\text{W}$ . For (A), the error bars represent estimated uncertainties in measured frequencies. For (B), the error bars represent fit uncertainties. The ions are laser cooled close to the Doppler limit. From comparison to simulations in Sec. IV C, we find  $T \approx 3.5 \text{ mK}$ .

that a resonance of the three to four lowest modes could be observed.

At first, the trapping ratio  $\alpha$  is determined by measuring the axial and transverse center-of-mass mode frequencies, i.e., the trapping frequencies. This is followed by searching for the low-lying modes with 1, 2, and 3 axial nodal points. In Fig. 3, we show the measured vibrational-mode frequencies in comparison to the normal-mode frequencies expected from the second-order approximation. Away from the phase transition, the experimental results agree with the theoretical predictions. However, close to the phase transition, the frequency of the zigzag mode does not vanish. The measured frequency of mode  $(1, N-1)$  (blue empty circles) increases when  $\alpha$  approaches  $\alpha_c$  until it reaches the expected frequency of the breathing mode of the 1D phase. The purely radial zigzag mode in the 1D phase could not be excited by this measurement, due to the missing overlap between the laser beam profile and the normal-mode vector, see Sec. III B. While the  $(2, 0)$  mode frequency (black empty diamonds) was observed over the complete phase transition, close to transition the breathing mode in the 2D phase (red empty thin diamonds) was not detected.

In measurement series (B), a single ions fluorescence was recorded with a region of interest (ROI) on the EMCCD, while sweeping the excitation frequency. Near resonance, a decrease in fluorescence in the ROI is observed, because the excited ion moves partially out of the ROI during exposure and it gains a Doppler shift due to its increased velocity. We fit the fluorescence drop to a Lorentzian line shape in order to determine the resonance frequencies of the axial center of mass and the normal mode with one axial nodal line.

To obtain a finer resolution in series (B), the maximum power of the amplitude modulated laser was about  $P_m^{(B)} = 6 \mu\text{W}$ , sufficient to excite the center of mass and breathing mode. A smaller amplitude of the forced oscillation reduces sampling of higher order terms of the Coulomb potential, which leads to asymmetric line shapes and line broadening. In Fig. 3, we show the results of these measurements as cyan squares. The results agree qualitatively with the measurements from series (A). We verify an increased vibrational mode frequency of the zigzag mode in the 2D phase close to  $\alpha_c$ . In the range of  $\alpha = 11.5$  to  $11.85$ , a quantitative difference of the measured frequencies is observed, up to a difference of approximately  $0.2\omega_z$ .

The quantitative difference between (A) and (B) is due to the smaller power of the amplitude modulated laser used for measurement run (B). A larger driving force increases the mode amplitudes in the steady state and therefore enhances nonlinear frequency shifts due to the Coulomb interaction. Increased power leads to a higher observed frequency at maximum excitation. Additionally, the line shape becomes increasingly asymmetric with increased power. We refer the interested reader to Appendix C, where we discuss the influence of  $P_m$  on the frequency of the  $(1, N-1)$  mode, see Fig. 10.

#### IV. MOLECULAR DYNAMICS SIMULATIONS

As seen in the last section, close to the phase transition the measured excitation frequencies significantly deviate from the vibrational spectrum in the harmonic approximation. We identify two possible sources for this deviation, either the damping due to laser cooling or the interaction with higher order terms in the expansion of the Coulomb potential could be responsible. As the damping,  $\gamma = 8.75 \times 10^3 \text{ s}^{-1}$ , is orders of magnitude smaller than the lowest axial frequencies, approx.  $1.6 \times 10^5 \text{ s}^{-1}$ , its influence is negligible. Therefore, the higher order terms are the most likely cause for the observed deviations. In the experiment, there are two excitation sources that lead to increased amplitudes: the thermal noise from laser cooling and the sinusoidal driving force. To gain deeper insight into the impact of the mode populations on the measurable frequencies, we carry out molecular dynamics simulations of the crystal under a stochastic force.

We simulate the dynamics of the ion crystal by numerically solving the classical equations of motion of the ions in the presence of damping and of the Langevin force describing thermal noise [28]. This approach is complementary to the Fokker-Planck equation for Doppler cooling of an ion crystal [55]. The equation of motion for the  $i$ th degree of freedom takes the form

$$m\ddot{u}_i + \frac{\partial V}{\partial u_i} + m\gamma\dot{u}_i = \xi_i(t), \quad (3)$$

where  $\gamma$  is a damping term from laser cooling and  $V$  is the total potential energy, see Eq. (1), and  $\xi_i(t)$  is the stochastic force, with moments

$$\langle \xi_i(t) \rangle = 0, \quad (4)$$

$$\langle \xi_i(t)\xi_j(t') \rangle = 2D\delta_{ij}\delta(t-t'). \quad (5)$$



Here,  $\langle \dots \rangle$  indicates ensemble averaging. The diffusion coefficient  $D$  of the second equation links the amplitude of the stochastic force with temperature and damping coefficients according to the fluctuation-dissipation theorem,  $D = m\gamma k_B T$  [56]. In the simulations, laser cooling is treated as isotropic for all degrees of freedom. This is a simplification with respect to the experiment. There, the damping between the transverse and axial direction is slightly different due to the projection of the cooling laser beams on the crystal axes, with projections on  $x$  and  $y$  being  $\cos(45^\circ) \approx 0.71$  and  $z$  being  $\cos(25^\circ) \approx 0.91$ .

We first detail the simulation procedure and the spectral analysis. The results of the molecular dynamics simulation are then reported and discussed in Sec. IV C.

### A. Simulation procedure

The ground-state configuration for each trapping ratio  $\alpha$  is found by simulating a crystal with  $N = 30$  ions choosing strong damping  $m\gamma = 2.5 \times 10^{-19} \text{ kg s}^{-1}$  ( $\gamma = 8.75 \times 10^5 \text{ s}^{-1}$ ) and with  $T = 0$ . The resulting equilibrium positions so obtained are the initial configuration for the simulation at finite temperature  $T$ . The simulation is run with lower damping  $m\gamma = 2.5 \times 10^{-21} \text{ kg s}^{-1}$  ( $\gamma = 8.75 \times 10^3 \text{ s}^{-1}$ ), comparable to experimental conditions [28], and over a time of  $100 \mu\text{s}$  to thermalize the system. The system is in a thermal state after this, which we checked via the equipartition theorem.

This result is used as a starting point for the final simulations, which run for 10 ms in total to achieve a fine resolution in the Fourier frequencies. All simulations have an integration time step of 19 ns, which is much smaller than the expected period of the vibrational mode with the largest frequency, which here is the transverse vibration of the center-of-mass mode at about  $3 \mu\text{s}$ . Every 100th value is saved, resulting in time resolution of the ions evolution of  $1.9 \mu\text{s}$ .

### B. Spectral analysis

To extract the normal-mode spectrum of the ion crystal, we carry out the Fourier transform (FT) of the trajectories of the ions' axial and transverse degrees of freedom. Due to the simulation length and time resolution, the FT has a frequency resolution of 100 Hz and a maximum observable frequency of about 263 kHz, which covers the frequency range of interest. For our analysis, the simulation procedure described above is repeated five times, due to the stochastic nature of the thermal noise, and the FTs are averaged over all simulations with identical parameters. Then the absolute value  $A(\omega)_{\chi,i} = |\bar{F}(x_{\chi,i})|$  of the averaged FTs  $\bar{F}$  is calculated, where  $i$  is the ion index and  $\chi$  is either  $x$  or  $z$ . We are interested in collective motions of the crystal, i.e., the normal modes, but we do not make any assumptions on possible mode vectors. Therefore, the  $A(\omega_{\chi,i})$  for all ions are added together to get a signal  $S(\omega)_{\chi}$ ,

$$S(\omega)_{\chi} = \sum_{i=1}^N A(\omega)_{\chi,i}, \quad (6)$$

where the degrees of freedom along  $x$  and  $z$  are treated separately. An example of such a signal is shown in Fig. 4. The width of the resonances depends on the damping  $\gamma$ , which is

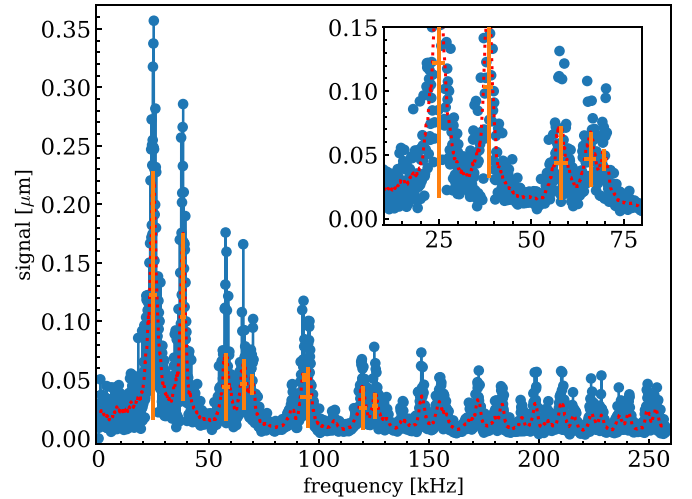


FIG. 4. Example of a FFT signal  $S_z$ , Eq. (6). The signal is extracted from the trajectory of the  $z$  coordinates of five molecular dynamics simulations at  $\alpha = 11.7$  and  $T = 0.1 \text{ mK}$ . The blue dots show the FFT, the dotted red line is the running mean of the signal over 30 points, the orange lines indicate automatically estimated center and widths of the peaks. The inset shows a zoom up of the first five peaks. See text for further details on the simulation.

here fixed to the value  $m\gamma = 2.5 \times 10^{-21} \text{ kg s}^{-1}$  to compare the data to our experiment.

We extract the resonances and the peaks' widths from  $S(\omega)$ . Without prior knowledge of the complete model of the peak functions, we estimate the positions based on a peak search algorithm. It searches for local maxima that fulfill certain conditions with respect to their width, absolute height, and relative height to the closest base line. This method cannot treat noisy signals well. Therefore,  $S$  is smoothed before starting a peak search, using a running mean over  $n$  values  $S_{\text{rm}}(k) = \sum_{i=0}^n S_{k+i}/n$ . For  $T = 0.1 \text{ mK}$ , an average over 20 points ( $\approx 2 \text{ kHz}$ ) and, for the other shown temperatures, an average over 30 points ( $\approx 3 \text{ kHz}$ ) is used. The running mean of the signal is plotted as a function of the respective running mean frequency  $f_{\text{rm}}(k) = \sum_{i=0}^n f_{k+i}/n$ . In Fig. 4, the smoothed signal  $S_{\text{rm}}$  is shown as a red dotted line. The orange line shows the peak positions and estimated half-maximum widths which we identified. Not all peaks are captured by the algorithm, especially for  $\omega > 2\pi \times 130 \text{ kHz}$ , due to the choice of selection parameters, that favor the prominent peaks at lower frequencies. However, the high-frequency peaks are outside the frequency range that we are interested in. Due to the noisy data, additional small peaks might be found close to strong resonances, e.g., the axial center of mass mode. These false positives have to be removed manually.

### C. Numerical results

We evaluate the simulations for temperatures  $T = [0.1, 0.5, 2.0, 3.5] \text{ mK}$  and for several trapping ratios  $\alpha$ . Figure 5 displays the estimated peak positions. The expected normal-mode frequencies at  $T = 0$  are also shown for comparison. We observe good agreement between the numerical results and the harmonic spectrum at low temperatures. For higher temperatures, deviations appear near the phase

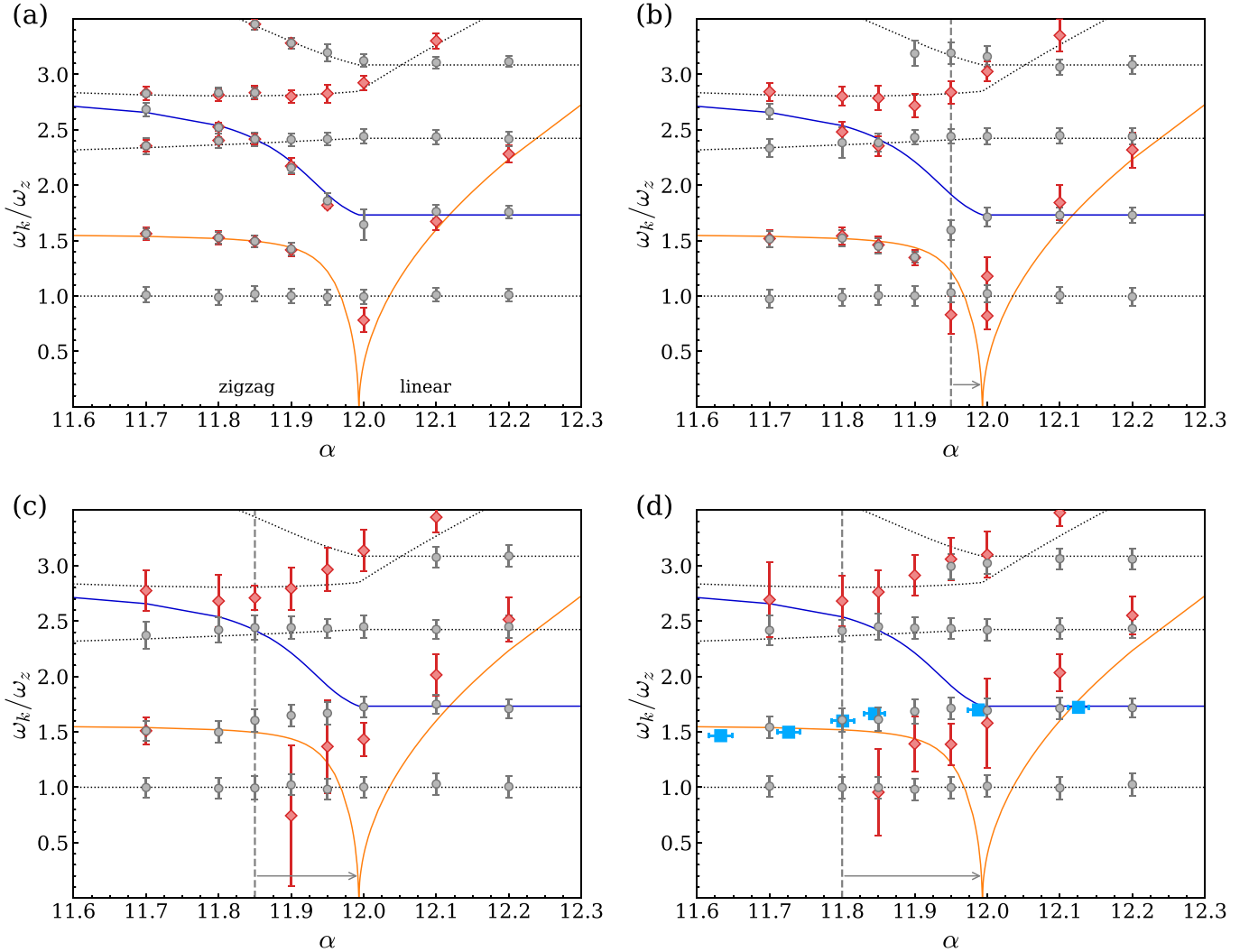


FIG. 5. Spectrum of the ion crystal vibrations as a function of  $\alpha$  and for different simulation temperatures: (a) 0.1 mK, (b) 0.5 mK, (c) 2.0 mK, (d) 3.5 mK. Lines represent the spectrum in the absence of thermal excitations: the color code is solid orange (dark blue) for zigzag (breathing) mode and dotted black for other modes. The symbols are results obtained from a peak search in the sum of Fourier-transform amplitudes of the axial (gray dots) and transverse (red diamond) trajectories. The error bars indicate the estimated FWHM of the peak. Light blue squares are experimental results for measurement series (B). The gray dashed vertical line and the gray arrow mark the range of  $\alpha$  at which we observe one or more jumps between the ground states per zigzag mode oscillation period  $T_{zz}$ .

transition for the (1,0) and (0,  $N-1$ ) modes that qualitatively agree with the experimental measurement, meaning that the expected increase in the breathing mode frequency, when transitioning from the 1D phase into the 2D phase, is not observed, and that the zigzag mode frequency in the 2D phase seems to increase, when  $\alpha$  approaches  $\alpha_c$  from lower values. The simulations for  $T = 3.5$  mK match best to the measurement series (B), which are shown in Fig. 5(d) for comparison. Here, we point out, that the frequency of the zigzag mode remains finite at  $\alpha_c$  and increases with the temperature, which can be seen in Figs. 5(b) to 5(d) in the radial points (red diamonds) around  $\alpha \approx 12.0$ .

In the simulations, we do not observe a deviation of the (2,0) mode from the harmonic approximation as we did in the experiments. This is most likely due to the high excitation power  $P_m^{(A)}$  used in series (A), as we described in Sec. III C. The additional increase in mode amplitude leads to nonlinear mode coupling on top of temperature effects.

The simulations reveal that in the 2D phase, thermal effects give rise to collective jumps of the ions between the two degenerate zigzag configurations. In Appendix B, we discuss how these jumps are observed in the time evolution of the central ion, see Fig. 8. We illustrate the mechanism as thermal switching between the two minima of the Landau free energy in the symmetry-broken phase [33], see Fig. 6(a). We can estimate the corresponding switching rate  $k_{\text{est}}$  by counting the number of sign changes of the transverse coordinate of the central ion  $P_{N/2}^x$  over the simulation length  $\Delta t$ :

$$k_{\text{est}} = P_{N/2}^x / \Delta t. \quad (7)$$

The inverse of this rate is the average dwelling time in one crystal configuration  $\tau_e = k_{\text{est}}^{-1}$ . We identify two regimes with the help of  $\tau_e$ . In the first regime  $\tau_e > T_{zz}$ , with  $T_{zz}$  being the characteristic period of oscillations of the (1,  $N-1$ ) mode, which is the slowest oscillation contributing to the

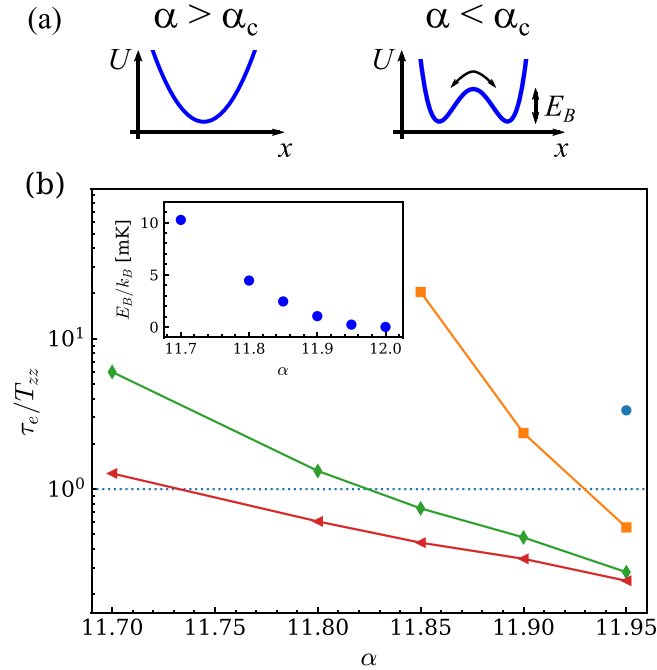


FIG. 6. (a) Schematic illustration of the Landau potential  $U$  in the 1D ( $\alpha > \alpha_c$ ) and in the 2D symmetry-broken phase ( $\alpha < \alpha_c$ ). The coordinate  $x$  indicates the transverse displacement of the central ion from the chain axis. Thermal excitations can overcome the barrier between the two degenerate zigzag configuration by inducing collective jumps of the crystal configuration. (b) Average dwelling time  $\tau_e = 1/k_{\text{est}}$ , Eq. (7), in units of the zigzag mode period  $T_{zz}$ . In the simulations, temperatures  $T$  are 0.1 mK (blue circles), 0.5 mK (orange squares), 2.0 mK (green diamonds), 3.5 mK (red triangles). The lines are a guide for the eye. For  $T = 0.1$  mK and 0.5 mK, missing points indicate no switches were observed during the simulation time. The dotted horizontal line indicates  $\tau_e = T_{zz}$ . Inset shows the potential barrier  $E_B$  for different trapping ratios  $\alpha$ .

movement between the two minima, see Fig. 6(a). Here the two crystalline configurations are well defined in the 2D phase and thermal noise gives rise to approximately instantaneous jumps, whose net effect is to broaden the linewidth of the resonance lines. In the second regime, where  $\tau_e \lesssim T_{zz}$ , the system switches rapidly between the minima and is on average in the 1D phase. Here, nonlinearities of the system are dominant and expected to modify the normal-mode spectrum. Figure 6(b) displays  $\tau_e$  as a function of the aspect ratio and, for different temperatures, the horizontal line indicates  $\tau_e = T_{zz}$ . We have verified that frequency deviations from the harmonic solution are observed when  $\tau_e \lesssim T_{zz}$ . This is visible, for instance, in Fig. 5, where the vertical dashed lines indicate the smallest aspect ratios of the simulations at which  $\tau_e \lesssim T_{zz}$ .

To gain insight into these dynamics, we analytically estimate the switching rate using an effective potential  $U$  that describes the double well structure. In the thermodynamic limit,  $U$  becomes the Landau free energy, see Sec. V. We interpret the switching rate as the rate of thermal activation [57] over the barrier separating the minima. To determine  $U$ , we calculate the potential energy along the adiabatic path connecting the two equilibrium configurations [58]. Since the two ground states stem from the breaking of the mirror symmetry,

we parameterize the path by the transverse crystal size,

$$g(\mathbf{u}) = x_{N/2} - x_{N/2+1},$$

where  $x_{N/2}$  is the transverse position of the ion left of the crystal center for even  $N$ . For the calculation, we minimize the crystal energy using a Lagrange multiplier with a constraint for the crystal transverse size  $g(\mathbf{u}) = X$ . For this, we numerically solve the following equation using Newton's method:

$$\nabla(V(\mathbf{u}) + \lambda(g(\mathbf{u}) - X)) = 0,$$

where  $V$  is given by Eq. (1), the gradient is given by  $\{\partial/\partial u_1, \dots, \partial/\partial u_{3N}, \partial/\partial \lambda\}^T$  and  $\lambda$  is the Lagrange multiplier. Afterward, the total potential energy for this configuration is taken as the energy  $U(X)$  of the potential at size  $X$ . As expected, in the 2D phase it has the shape of a double well with two minima, symmetric about  $X = 0$ . The energy barrier  $E_B$ , separating the two ground states, is then given as the difference between the potential energy at  $X = 0$  and the minimum potential energy:

$$E_B = U(0) - \min(U(X)).$$

Sufficiently close to the transition the energy barrier increases with  $|\alpha - \alpha_c|^2$ , see inset in Fig. 6(b), in agreement with the predictions of Ref. [33] and with the numerical simulations of the linear to zigzag transition in clusters of metallic beads [59].

The trajectory of the collective coordinate of the crystal that jumps between the minima of the bistable potential results from the interplay of driving, damping, and noise. Quantitatively accounting for the prefactors in the Kramer's escape formula [60] is beyond the scope of the current paper. Here, we perform an estimate using transition-state theory [57],

$$k_{\text{TST}} \approx \omega_a / (2\pi) \exp[-E_B / (k_B T)],$$

with  $\omega_a = \sqrt{U''(X_{\min})/m}$ , where  $U''$  is the second derivative with respect to  $X$  and  $X_{\min}$  is the transverse crystal size in equilibrium. For  $\alpha = 11.8$  and  $T = 2.0$  mK, the transition-state theory predicts a rate about  $16000 \text{ s}^{-1}$ . Taking into account that, in the simulations, the particles can also return to each minima the escape rate in the simulation from one minimum is about  $14000 \text{ s}^{-1}$ . In Appendix B, we compare the rates extracted from the simulations with the predictions of transition-state theory rates over a range of parameters. We find agreement within a factor of 2.

The molecular dynamics simulation validate the thermal fluctuations as the source of the observed frequency deviations. Moreover, they supply a deeper insight into the exact dynamics behind the nonlinear mechanism at hand, i.e., the frequent crossing of the potential barrier between the two degenerate ground states of the 2D phase.

## V. EFFECTIVE MODEL FOR THE MODES DYNAMICS

In this section, we use a simplified model to determine the temperature dependence of the mode spectrum close to the linear to zigzag instability. For this purpose, we use a complementary approach to the one based on dwelling times and consider the normal-mode expansion around the linear chain for aspect ratios at which the linear chain is mechanically unstable. We then evaluate the average effect of the higher modes

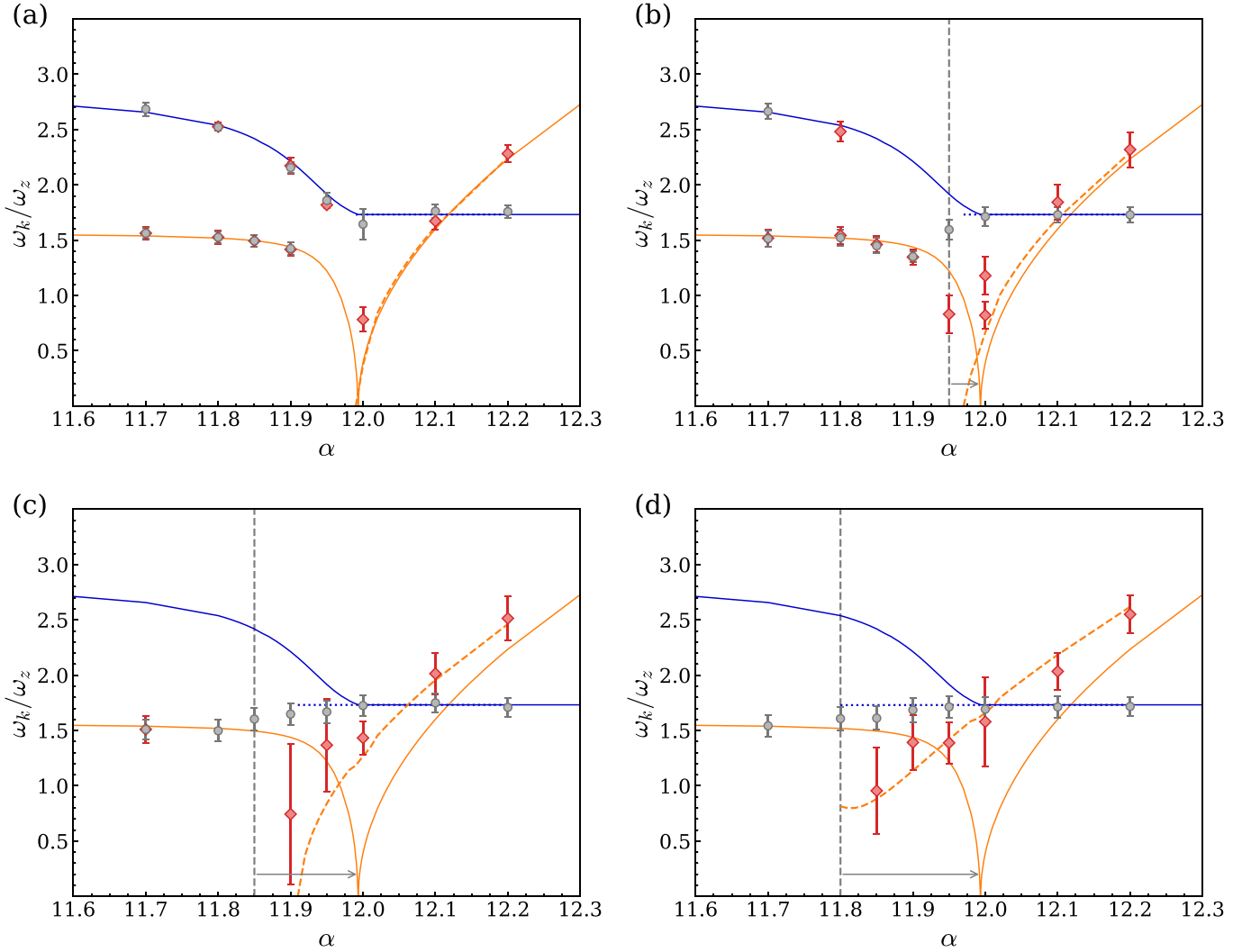


FIG. 7. The zigzag and breathing mode frequencies as a function of the aspect ratio  $\alpha$ . The parameters and legend are the same as Fig. 5. Moreover, the dashed and dotted lines correspond to the predictions of the analytical model:  $\tilde{\omega}_2$  (dark blue, dotted) and  $\tilde{\omega}_1$  (orange, dashed). The analytical solutions are shown until  $\tilde{\omega}_1$  becomes imaginary or until less than one switch per zigzag mode oscillation period  $T_{zz}$  is observed, i.e., for values of  $\alpha$  below the range marked by the gray dashed vertical lines and the gray arrows.

on the lowest part of the spectrum using a timescale separation ansatz and determine the resulting spectrum as a function of the temperature. The resulting normal-mode spectrum agrees with the numerical results close to the transition point, as we discuss below and summarize in Fig. 7.

### A. Normal modes at the instability

We first review the normal modes of the linear chain and the equations for the structural instability in the absence of damping and noise. Close to the linear to zigzag instability, we expand the total potential energy  $V$  of Eq. (1) to fourth order around the equilibrium positions of the linear chain,

$$V_4 = \frac{1}{2!} \sum_{ij=1}^{3N} K'_{ij} q_i q_j + \frac{1}{3!} \sum_{ijk=1}^{3N} L'_{ijk} q_i q_j q_k + \frac{1}{4!} \sum_{ijkl=1}^{3N} M'_{ijkl} q_i q_j q_k q_l, \quad (8)$$

where  $q_i$  are the displacements around the equilibrium positions  $u_i(0)$ ,  $q_i = u_i - u_i(0)$ , the tensors  $L'$  and  $M'$  are given by the expressions

$$L'_{ijk} = \frac{\partial^3 V}{\partial u_i \partial u_j \partial u_k} \Big|_{\mathbf{u}(0)}, \quad (9)$$

$$M'_{ijkl} = \frac{\partial^4 V}{\partial u_i \partial u_j \partial u_k \partial u_l} \Big|_{\mathbf{u}(0)}, \quad (10)$$

and  $K'$  is given by Eq. (2). Note that  $V_4$  approximates the total potential  $V$ , Eq. (1), in the limit in which the displacements around the equilibrium positions are much smaller than the interparticle distance at equilibrium.

As introduced in Sec. II,  $\Theta_j$  denote the normal modes of the linear chain, which diagonalize the matrix  $K'$  and have eigenvalues  $m\omega_j^2$ . The linear chain is stable provided that all eigenvalues are positive. In this regime, the  $\omega_j$  are real and correspond to the normal-mode frequencies. The condition  $\min_j \omega_j = 0$  identifies the classical transition point of the linear to zigzag instability. Potential Eq. (8) is cast in terms of

the normal mode by means of the dynamical matrix  $\lambda_{ij}$  such that  $q_i = \sum_j \lambda_{ij} \Theta_j$  and takes the form

$$V_4 = \frac{1}{2!} \sum_{i=1}^{3N} m \omega_i^2 \Theta_i^2 + \frac{1}{3!} \sum_{ijk=1}^{3N} L_{ijk} \Theta_i \Theta_j \Theta_k + \frac{1}{4!} \sum_{ijkl=1}^{3N} M_{ijkl} \Theta_i \Theta_j \Theta_k \Theta_l, \quad (11)$$

where now the tensors  $L$  and  $M$  are related to the tensors  $L'$  and  $M'$  by the relations

$$L_{ijk} = \sum_{mns=1}^{3N} L'_{mns} \lambda_{mi} \lambda_{nj} \lambda_{sk}, \quad (12)$$

$$M_{ijkl} = \sum_{mnst=1}^{3N} M'_{mnst} \lambda_{mi} \lambda_{nj} \lambda_{sk} \lambda_{tl}. \quad (13)$$

The total Lagrangian for the normal modes takes the form  $L = \frac{1}{2} m \sum_{i=1}^{3N} \dot{\Theta}_i^2 - V_4$ .

In an appropriately defined thermodynamic limit, for which the critical aspect ratio converges to a finite value as  $N \rightarrow \infty$ , the linear-zigzag transition can be cast in terms of the Landau potential,

$$U_{LG} = \mathcal{V} \Theta_{zz}^2 + A \Theta_{zz}^4, \quad (14)$$

where  $\Theta_{zz}$  is the amplitude of the zigzag mode in the linear chain,  $A > 0$  and  $\mathcal{V} \propto (\alpha^2 - \alpha_c^2)$ . This potential is determined from potential  $V_4$  in lowest order in a gradient expansion [33]. The one-dimensional model strictly exhibits a phase transition at zero temperature, where a quantum description becomes appropriate [45,46,49,61]. In what follows, instead we consider a finite system and do not scale the physical parameters with  $N$ .

### B. Thermal effects

We now discuss the low-frequency spectrum of the linear chain across the linear to zigzag instability and in the presence of laser cooling. We consider a finite chain and, starting from the Fokker-Planck equation [55], we model the dynamics of laser Doppler cooling in terms of Langevin equations. We denote the damping (cooling) rates of the normal modes by  $\gamma_i$  and write the corresponding Langevin equations as [62]

$$\ddot{\Theta}_i = -\frac{1}{m} \frac{\partial V_4}{\partial \Theta_i} - \gamma_i \dot{\Theta}_i + \Xi_i(t), \quad (15)$$

where  $\Xi_i(t)$  is the Langevin force for the normal mode  $\Theta_i$ , with  $\langle \Xi_i(t) \rangle = 0$ ,  $\langle \Xi_i(t) \Xi_j(t') \rangle = 2\gamma_i (k_B T / m) \delta_{ij} \delta(t - t')$  and we neglect here mode-mode correlations due to the dissipative dynamics.

For finite chains and in the 2D phase, the lowest frequency mode is a superposition of the zigzag mode and of the axial breathing mode of the linear chain as seen in Fig. 1(c).

The gap between the soft mode and all other normal modes remains finite. Thus, whenever thermal excitations and the line broadening are smaller than the gap, normal-mode spectroscopy of the chain shall provide in first approximation the mode spectrum obtained by diagonalizing the quadratic term of potential Eq. (1) about the stable equilibrium positions.

We now determine the effects of thermal excitation on the lowest energy spectrum by considering the equations of the lowest energy mode, here  $(0, N-1)$ , which we label  $\Theta_1$ , and the mode which is closest in frequency and to which it couples. This mode is labeled by  $\Theta_2$  and is according to our notation  $(1,0)$ . We then make the simplifying assumption that  $\omega_1, \omega_2 \ll \omega_\ell$ , where  $\omega_\ell$  are here the frequencies of the modes  $\Theta_\ell$  to which  $\Theta_1$  and  $\Theta_2$  appreciably couple through the anharmonicities. In this regime, we can identify the time scale  $\delta t$  for which  $\omega_1 \delta t, \omega_2 \delta t \ll 1$  and  $\omega_\ell \delta t \gg 1$ . Moreover, we assume that the modes  $\Theta_\ell$  are at thermal equilibrium. We now perform the time average of Eq. (15) over the grid with step  $\delta t$ . For convenience, we introduce the notation

$$\frac{1}{\delta t} \int_t^{t+\delta t} d\tau f(\tau) \equiv \langle f(t) \rangle_{\delta t}, \quad (16)$$

where  $f(t)$  is a function of time. Since  $\omega_1 \delta t, \omega_2 \delta t \ll 1$ , then  $\langle \Theta_{1,2}(t) \rangle_{\delta t} \approx \Theta_{1,2}(t)$ . Moreover, to provide an example, the contribution of the fourth-order term of Eq. (11), which we denote by  $W_4$ , takes the form

$$\left\langle \frac{\partial W_4}{\partial \Theta_1} \right\rangle_{\delta t} \approx \sum_\ell \left( \frac{1}{2} M_{11\ell\ell} \langle \Theta_\ell^2 \rangle_{\delta t} \Theta_1 + \frac{1}{2} M_{12\ell\ell} \langle \Theta_\ell^2 \rangle_{\delta t} \Theta_2 \right),$$

where the equation for  $\Theta_2$  is found by replacing  $1 \rightarrow 2$  and we used that for  $\ell \neq 1, 2$  the eigenmodes are at thermal equilibrium, thus  $\langle \Theta_\ell \rangle_{\delta t} = 0$  and  $\langle \Theta_\ell \Theta_{\ell'} \rangle_{\delta t} = \delta_{\ell,\ell'} \langle \Theta_\ell^2 \rangle_{\delta t}$ . Finally, assuming ergodicity, we obtain  $\langle \Theta_\ell^2 \rangle_{\delta t} = k_B T / (m \omega_\ell^2)$  from the classical equipartition theorem. This procedure leads to the two coupled equations:

$$\ddot{\Theta}_1 = -\tilde{\omega}_1^2 \Theta_1 - \frac{1}{2} v_{12}^2 \Theta_2 + \eta_1 - \gamma_1 \dot{\Theta}_1 + \Xi_1, \quad (17)$$

$$\ddot{\Theta}_2 = -\tilde{\omega}_2^2 \Theta_2 - \frac{1}{2} v_{12}^2 \Theta_1 + \eta_2 - \gamma_2 \dot{\Theta}_2 + \Xi_2, \quad (18)$$

where  $\tilde{\omega}_i, v_{12}$ , and  $\eta_i$  are explicitly dependent on the temperature. In particular, the frequency squared  $\tilde{\omega}_i^2$  now reads

$$\tilde{\omega}_i(T)^2 = \omega_i^2 + v_i(T)^2 = \omega_i^2 + v_{\text{eff},i}^2 T, \quad (19)$$

and it contains a shift proportional to the temperature with proportionality constant

$$v_{\text{eff},i}^2 = \frac{1}{2m} \sum_{k \neq 1,2} M_{iikk} \frac{k_B}{m \omega_k^2}. \quad (20)$$

The second and third terms on the right-hand side of Eqs. (17) and (18) describe an effective coupling between the two modes and a mean displacement force, respectively, with

$$v_{12}(T)^2 = \frac{1}{m} \sum_{k \neq 1,2} M_{12kk} \frac{k_B T}{m \omega_k^2} \equiv v_{\text{eff},12}^2 T, \quad (21)$$

$$\eta_i = -\frac{1}{2} \sum_{k \neq 1,2} L_{iikk} \frac{k_B T}{m \omega_k^2} \equiv -\eta_{\text{eff},i} T. \quad (22)$$

The effective, temperature-independent constants  $v_{\text{eff},i}^2$ ,  $v_{\text{eff},12}^2$ , and  $\eta_{\text{eff},i}$  for the two modes  $i = 1, 2$  are determined by carrying out the summation in Eqs. (20)–(22) over all other modes  $k$ . We remark that the shifts depend on  $\alpha$  through the coefficients of the expansion of  $V_4$ .

Equations (17) and (18) describe mode mixing and frequency shifts induced by the thermal excitation of the chain. Within this classical model, these terms are directly proportional to the temperature. We can now determine the resulting normal-mode frequencies. For this purpose, we note that the term  $\nu_{12} = 0$  for the expansion about the linear-chain equilibrium positions, see Table I of Appendix A. This is a consequence of the fact the breathing mode is an exact eigenmode of the linear chain [47]. In the underdamped limit, corresponding to  $\gamma_i \ll \omega_i$ , the characteristic frequencies are now given by Eqs. (19) and (20). Figure 7 displays the frequencies  $\tilde{\omega}_i$  as a function of the aspect ratio  $\alpha$  and for four increasing values of the temperature, ranging between 0.1 mK and 3.5 mK. For comparison, the results of the numerical simulation of Eq. (3) are reported, which agreed well with the experimental measurements presented in Sec. III for  $T = 3.5$  mK. The prediction of the analytical model and the result of the numerical simulation agree for aspect ratios close to the transition point  $\alpha_c$ : This is the regime where our model is plausible since the truncation of the Taylor expansion is justified. We note that, even though these analytical arguments have been applied to a finite chain, the considerations of our theoretical model are also valid in the thermodynamic limit and show that at finite temperatures the coupling with the high-frequency modes significantly modifies the properties at the instability. Loosely speaking, the thermal effects stabilize the linear chain also for aspect ratios beyond the critical point. This behavior might be interpreted as a shift of the transition point [39] in the sense that a measurement of the mean transverse displacement will give zero in the regime where the ion dynamics consists of thermally activated jumps between the two zigzag configurations. Thus, a linear chain will be effectively detected for aspect ratios  $\alpha$  below but close to  $\alpha_c$ . Nevertheless, in the classical regime this is the manifestation of a nonuniversal crossover dynamics.

## VI. CONCLUSION

In this paper, we investigated experimentally and theoretically the effect of thermal noise on the low-frequency spectrum of an ion chain near the symmetry-breaking linear to zigzag transition.

In the experiment, we employed resonant light force modulation with an amplitude modulated laser beam to excite collective oscillations in a crystal. The method is simple to implement and can also be used to measure trapping frequencies, replacing established excitation methods, such as modulation of the trapping potentials [63]. This allows for stronger filters in the rf and dc electronics of the Paul trap [51,52], reducing the heating by electrical noise of the trapped ion crystals. While we used an excitation beam profile encompassing multiple ions, a more focused beam or a spatially engineered beam

profile, e.g., generated by an spatial light modulator [64,65], would allow for arbitrary mode excitations.

The experimental measurements did not show the softening of the zigzag mode that is predicted at the structural phase transition. Also, the frequency of the breathing mode was nearly constant and independent of  $\alpha$  when sweeping into the 2D phase, instead of increasing as expected in the absence of thermal noise.

With the help of molecular dynamics simulations, we could reproduce the experimental observations within the uncertainties, thus confirming that this behavior is primarily due to thermal excitations. In particular, inspection of the trajectories show that finite temperature effects induce collective jumps of the ions between the two degenerate zigzag configurations. This microscopic picture is at the basis of the expected crossover behavior at finite temperatures.

We developed a simple analytical model that builds on these findings and predicts the experimentally observed frequency spectrum. This model shows that the temperature-dependent shift of the zigzag mode at the transition point is due to anharmonic coupling with high-frequency modes, which act as an effective phonon environment. Separation of timescales between the low-frequency soft mode and the higher frequency modes allows taking the averaged higher frequency modes as an effective potential that influences the soft mode. Note that the thermally excited phonon environment in our model could be replaced by nonthermal excitations. Single quanta excitations with coherent interaction in third order have been investigated in Ref. [66]. In future theoretical works, their method could be extended to describe the effects of finite temperatures. While we do not include the effects of micromotion induced by the rf of the trap in our theoretical models, it could be treated analytically following Ref. [67]. From our model it also follows that the observation of a low-frequency zigzag mode near the linear-zigzag transition at Doppler temperature of  $^{172}\text{Yb}^+$  is unlikely. However, it might be observed in a crystal with  $T \approx 100 \mu\text{K}$ . Therefore, in future experiments, methods of (near) ground-state cooling that can cool several modes in an ion Coulomb crystal, such as Sisyphus cooling [68–70] or electromagnetically induced-transparency cooling [71–75], need to be considered.

Our results suggest that a similar model can be developed to describe the experimental measurements of the Aubry-type transition in ion Coulomb crystals. Here the soft mode of the pinning to sliding transition exhibited a finite frequency at the critical point, when a finite temperature allowed the system to switch between different minima of the Peierls-Nabarro potential [12,76].

Our work is relevant for experiments operating close to phase transitions in ion chains such as studies of energy transport [77] or quantum information using the gapped topological defect mode [78,79]. According to the results presented, the cooling of high-frequency modes is crucial to avoid the heating of the soft mode due to higher-order coupling, showing the experimental complexity of these plans. Similar challenges were recently discussed for laser cooling a 2D planar crystal confined in a Penning trap [80].

### ACKNOWLEDGMENTS

We gratefully thank J. Keller for fruitful discussions. This project has been funded by the Deutsche Forschungsgemeinschaft (DFG, German Research Foundation) through Grant No. CRC 1227 (DQ-mat, project A07) and under Germanys Excellence Strategy EXC-2123 QuantumFrontiers 390837967. This project 17FUN07 CC4C has received funding from the EMPIR programme co-financed by the Participating States and from the European Union's Horizon 2020 research and innovation programme. G.M. acknowledges support by the Deutsche Forschungsgemeinschaft (DFG, German Research Foundation) through Grant No. CRC TRR 306 QuCoLiMa ("Quantum Cooperativity of Light and Matter") and by the German Ministry of Education and Research (BMBF) via the QuantERA project NAQUAS. Project NAQUAS has received funding from the QuantERA ERA-NET Cofund in Quantum Technologies implemented within the European Union's Horizon2020 program.

### APPENDIX A: EFFECTIVE ANALYTICAL CONSTANTS

In Table I, we present numerical values of the effective, temperature-independent constants defined in Eqs. (20)–(22) for  $N = 30$  ions near the linear to zigzag transition.

TABLE I. Effective higher order constants for a  $N = 30$  ion Coulomb crystal near the linear to zigzag phase transition for the zigzag mode and breathing mode. Crystal expanded around a linear chain.  $v_{\text{eff},i}^2$  and  $v_{\text{eff},12}^2$  are given in units of the squared axial frequency  $\omega_z^2$ . The constants  $\eta_{\text{eff},i}$  are given in units of  $m\omega_z^2 l_c$ , where  $l_c = [e^2/(4\pi\epsilon_0 m\omega_z^2)]^{1/3}$  is the length constant of a trapped ion Coulomb crystal.

| $\alpha$ | $v_{\text{eff},1}^2$ | $v_{\text{eff},2}^2$ | $v_{\text{eff},12}^2$ | $\eta_{\text{eff},1}$ | $\eta_{\text{eff},2}$ |
|----------|----------------------|----------------------|-----------------------|-----------------------|-----------------------|
| 11.70    | 3767.3904            | -6.4896              | -0.0039               | 0.0003                | -26.1177              |
| 11.80    | 1505.2251            | -2.7630              | -0.0021               | 0.0001                | -11.1188              |
| 11.85    | 1200.0101            | -2.2324              | 0.0020                | -0.0001               | -8.9835               |
| 11.90    | 1007.8599            | -1.8871              | 0.0021                | -0.0001               | -7.5937               |
| 11.91    | 977.3964             | -1.8312              | -0.0021               | 0.0001                | -7.3688               |
| 11.92    | 948.9239             | -1.7786              | 0.0022                | -0.0001               | -7.1572               |
| 11.93    | 922.2375             | -1.7290              | -0.0022               | 0.0001                | -6.9577               |
| 11.94    | 897.1609             | -1.6821              | 0.0023                | -0.0001               | -6.7689               |
| 11.95    | 873.5402             | -1.6377              | 0.0023                | -0.0001               | -6.5900               |
| 11.96    | 851.2413             | -1.5955              | -0.0024               | 0.0001                | -6.4201               |
| 11.97    | 830.1467             | -1.5553              | -0.0025               | 0.0001                | -6.2584               |
| 11.98    | 810.1524             | -1.5169              | -0.0027               | 0.0001                | -6.1041               |
| 11.99    | 791.1669             | -1.4803              | -0.0028               | 0.0001                | -5.9565               |
| 12.00    | 773.1083             | -1.4453              | -0.0030               | -0.0001               | 5.8158                |
| 12.05    | 694.4609             | -1.2899              | 0.0000                | 0.0000                | 5.1913                |
| 12.10    | 630.6453             | -1.1606              | 0.0000                | 0.0000                | 4.6702                |
| 12.20    | 532.5320             | -0.9539              | 0.0000                | 0.0000                | 3.8383                |

### APPENDIX B: SWITCHING RATES: SIMULATION AND TRANSITION-STATE THEORY

In Fig. 8, we show the time evolution of the transverse coordinate of the 15th ion for two different  $\alpha$  and for

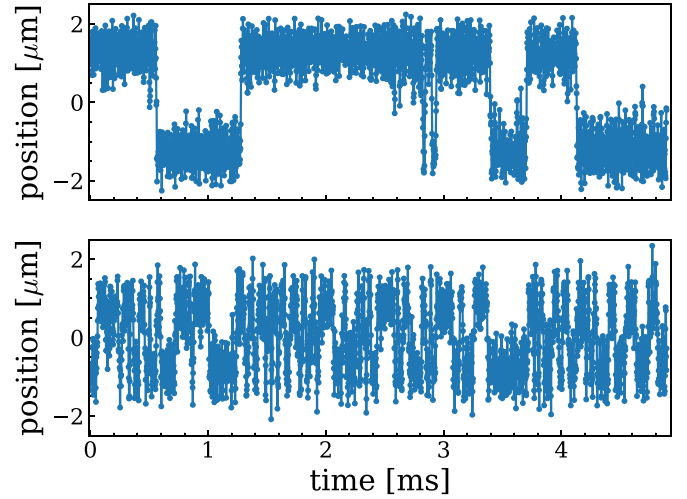


FIG. 8. Time evolution of transverse coordinate of ion 15. The top row is for  $\alpha = 11.7$  and the bottom row for  $\alpha = 11.85$ .  $T = 2.0$  mK closer to the transition at  $\alpha_c \approx 12.0$  the ion changes more often between the two ground-state configurations, about which the crystal oscillates.

$T = 2.0$  mK, to illustrate the switching of the crystal between the two ground-state configurations. In Fig. 9, we show the comparison between the escape rate obtained by transition-state theory from the double-well potentials calculated in Sec. IV C and the rates estimated from the simulation results. The latter have been corrected by a factor of 2 for the comparison to account for the possibility to come back to a potential minimum.

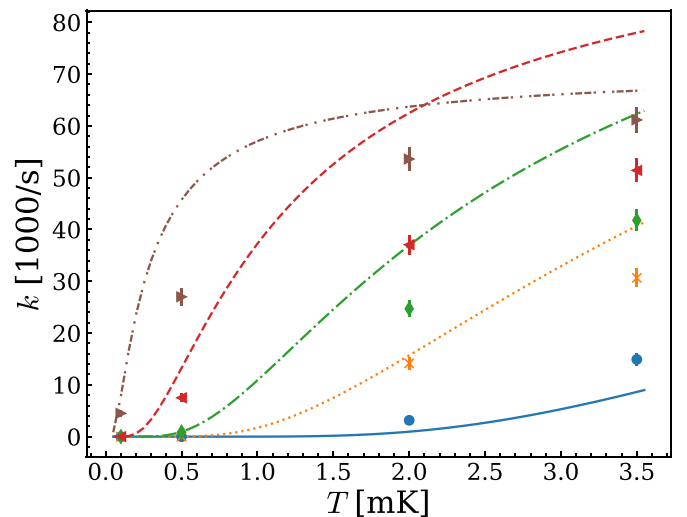


FIG. 9. Escape rate from transition-state theory  $k_{\text{TST}}$  (lines) and estimate rates from simulations  $k_{\text{est}}/2$  (symbols). Colors and markers are  $\alpha = 11.7$ ; blue circles and solid line,  $\alpha = 11.8$ ; orange crosses and dotted line,  $\alpha = 11.85$ ; green diamonds and dash-dotted line,  $\alpha = 11.9$ ; red left triangles and dashed line,  $\alpha = 11.95$ ; brown right triangles and double-dash-dotted line.

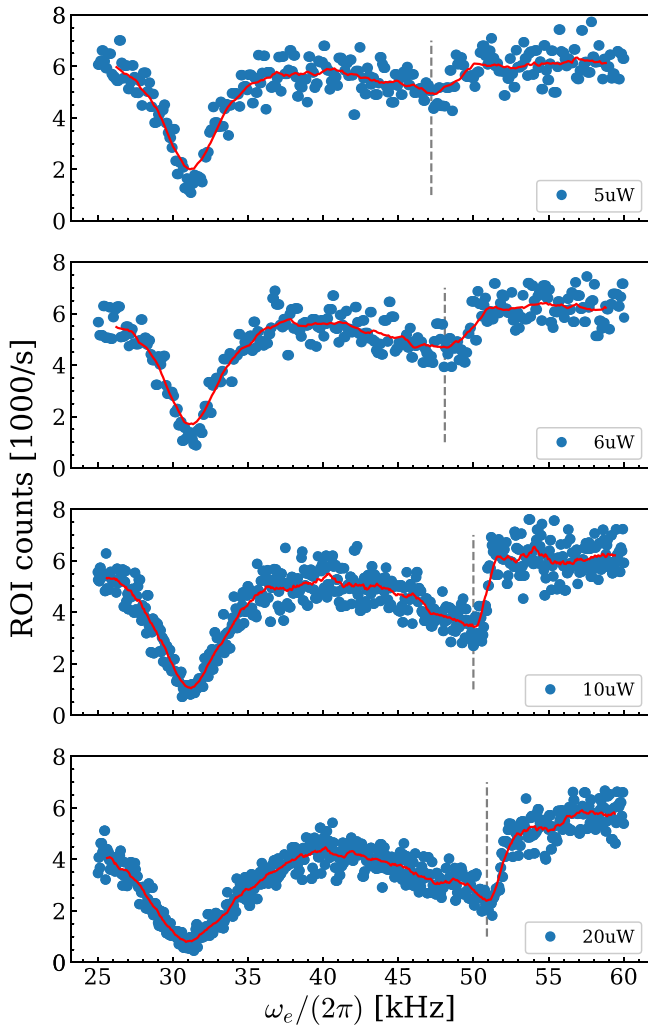


FIG. 10. Measured ROI fluorescence (blue dots) against modulation frequency  $\omega_e$  at  $\alpha \approx 11.72$ . The red line is a running mean over 50 points, acting as a guide to the eye. The dashed gray vertical lines indicate estimated maximum excitation for the breathing mode.

### APPENDIX C: POWER DEPENDENCY OF EXPERIMENTAL SIGNAL

Driving the intrinsically nonlinear Coulomb system can lead to additional frequency shifts due to further increased amplitudes. The excitation method employed in this paper can lead to such shifts, depending on the laser power of the modulated laser  $P_0$ .

In Fig. 10, we show the power dependence of recorded resonance features of measurement series (B) when sweeping over the axial center of mass and the breathing mode at  $\alpha \approx 11.72$ . It can be clearly seen that the position of maximum excitation of the breathing mode shifts when increasing the driving force. Additionally, the resonances become increasingly asymmetric with higher forces. The center-of-mass mode resonance around 31 kHz increases in width with higher forces.

Measurements presented in Sec. III C were carried out with  $P_m = 20 \mu\text{W}$  for series (A) and with  $P_m = 6 \mu\text{W}$  for series (B).

- 
- [1] D. H. E. Dubin and T. O’Neil, Trapped nonneutral plasmas, liquids, and crystals (the thermal equilibrium states), *Rev. Mod. Phys.* **71**, 87 (1999).
- [2] D. Leibfried, R. Blatt, C. Monroe, and D. Wineland, Quantum dynamics of single trapped ions, *Rev. Mod. Phys.* **75**, 281 (2003).
- [3] J. I. Cirac and P. Zoller, Quantum Computations with Cold Trapped Ions, *Phys. Rev. Lett.* **74**, 4091 (1995).
- [4] D. Leibfried, B. DeMarco, V. Meyer, D. Lucas, M. Barrett, J. Britton, W. M. Itano, B. Jelenkovi, C. Langer, T. Rosenband, and D. J. Wineland, Experimental demonstration of a robust, high-fidelity geometric two ion-qubit phase gate, *Nature* **422**, 412 (2003).
- [5] F. Schmidt-Kaler, H. Häffner, M. Riebe, S. Gulde, G. P. T. Lancaster, T. Deuschle, C. Becher, C. F. Roos, J. Eschner, and R. Blatt, Realization of the Cirac–Zoller controlled-NOT quantum gate, *Nature* **422**, 408 (2003).
- [6] P. Schindler, D. Nigg, T. Monz, J. T. Barreiro, E. Martinez, S. X. Wang, S. Quint, M. F. Brandl, V. Nebendahl, C. F. Roos, M. Chwalla, M. Hennrich, and R. Blatt, A quantum information processor with trapped ions, *New J. Phys.* **15**, 123012 (2013).
- [7] C. Monroe, R. Raussendorf, A. Ruthven, K. R. Brown, P. Maunz, L.-M. Duan, and J. Kim, Large-scale modular quantum-computer architecture with atomic memory and photonic interconnects, *Phys. Rev. A* **89**, 022317 (2014).
- [8] T. P. Harty, D. T. C. Allcock, C. J. Ballance, L. Guidoni, H. A. Janacek, N. M. Linke, D. N. Stacey, and D. M. Lucas, High-Fidelity Preparation, Gates, Memory, and Readout of a Trapped-Ion Quantum Bit, *Phys. Rev. Lett.* **113**, 220501 (2014).
- [9] T. Monz, D. Nigg, E. A. Martinez, M. F. Brandl, P. Schindler, R. Rines, S. X. Wang, I. L. Chuang, and R. Blatt, Realization of a scalable Shor algorithm, *Science* **351**, 1068 (2016).
- [10] K. Wright, K. M. Beck, S. Debnath, J. M. Amini, Y. Nam, N. Grzesiak, J.-S. Chen, N. C. Pisenti, M. Chmielewski, C. Collins, K. M. Hudek, J. Mizrahi, J. D. Wong-Campos, S. Allen, J. Apisdorf, P. Solomon, M. Williams, A. M. Ducore, A. Blinov, S. M. Kreikemeier, V. Chaplin, M. Keesan, C. Monroe, and



- J. Kim, Benchmarking an 11-qubit quantum computer, *Nat. Commun.* **10**, 5464 (2019).
- [11] A. Bylinskii, D. Gangloff, and V. Vuletić, Tuning friction atom-by-atom in an ion-crystal simulator, *Science* **348**, 1115 (2015).
- [12] J. Kiethe, R. Nigmatullin, D. Kalincev, T. Schmirander, and T. E. Mehlstäubler, Probing nanofriction and Aubry-type signatures in a finite self-organized system, *Nat. Commun.* **8**, 15364 (2017).
- [13] R. Matjeschk, C. Schneider, M. Enderlein, T. Huber, H. Schmitz, J. Glueckert, and T. Schaetz, Experimental simulation and limitations of quantum walks with trapped ions, *New J. Phys.* **14**, 035012 (2012).
- [14] K. Toyoda, Y. Matsuno, A. Noguchi, S. Haze, and S. Urabe, Experimental Realization of a Quantum Phase Transition of Polaritonic Excitations, *Phys. Rev. Lett.* **111**, 160501 (2013).
- [15] E. A. Martinez, C. A. Muschik, P. Schindler, D. Nigg, A. Erhard, M. Heyl, P. Hauke, M. Dalmonte, T. Monz, P. Zoller, and R. Blatt, Real-time dynamics of lattice gauge theories with a few-qubit quantum computer, *Nature* **534**, 516 (2016).
- [16] J. Zhang, G. Pagano, P. W. Hess, A. Kyprianidis, P. Becker, H. Kaplan, A. V. Gorshkov, Z.-X. Gong, and C. Monroe, Observation of a many-body dynamical phase transition with a 53-qubit quantum simulator, *Nature* **551**, 601 (2017).
- [17] M. Gärtner, J. G. Bohnet, A. Safavi-Naini, M. L. Wall, J. J. Bollinger, and A. M. Rey, Measuring out-of-time-order correlations and multiple quantum spectra in a trapped-ion quantum magnet, *Nat. Phys.* **13**, 781 (2017).
- [18] J. Brox, P. Kiefer, M. Bujak, T. Schaetz, and H. Landa, Spectroscopy and Directed Transport of Topological Solitons in Crystals of Trapped Ions, *Phys. Rev. Lett.* **119**, 153602 (2017).
- [19] D. J. Gorman, B. Hemmerling, E. Megidish, S. A. Moeller, P. Schindler, M. Sarovar, and H. Haefner, Engineering Vibrationally Assisted Energy Transfer in a Trapped-Ion Quantum Simulator, *Phys. Rev. X* **8**, 011038 (2018).
- [20] X. Zhang, K. Zhang, Y. Shen, S. Zhang, J.-N. Zhang, M.-H. Yung, J. Casanova, J. S. Pedernales, L. Lamata, E. Solano, and K. Kim, Experimental quantum simulation of fermion-antifermion scattering via boson exchange in a trapped ion, *Nat. Commun.* **9**, 195 (2018).
- [21] C. Kokail, C. Maier, R. van Bijnen, T. Brydges, M. K. Joshi, P. Jurcevic, C. A. Muschik, P. Silvi, R. Blatt, C. F. Roos, and P. Zoller, Self-verifying variational quantum simulation of lattice models, *Nature* **569**, 355 (2019).
- [22] M. Tamura, T. Mukaiyama, and K. Toyoda, Quantum Walks of a Phonon in Trapped Ions, *Phys. Rev. Lett.* **124**, 200501 (2020).
- [23] P. Jurcevic, H. Shen, P. Hauke, C. Maier, T. Brydges, C. Hempel, B. P. Lanyon, M. Heyl, R. Blatt, and C. F. Roos, Direct Observation of Dynamical Quantum Phase Transitions in an Interacting Many-Body System, *Phys. Rev. Lett.* **119**, 080501 (2017).
- [24] T. W. Kibble, Topology of cosmic domains and strings, *J. Phys. A: Math. Gen.* **9**, 1387 (1976).
- [25] W. H. Zurek, Cosmological experiments in superfluid helium? *Nature* **317**, 505 (1985).
- [26] A. del Campo, G. De Chiara, G. Morigi, M. B. Plenio, and A. Retzker, Structural Defects in Ion Chains by Quenching the External Potential: The Inhomogeneous Kibble-Zurek Mechanism, *Phys. Rev. Lett.* **105**, 075701 (2010).
- [27] S. Ulm, J. Roßnagel, G. Jacob, C. Degünther, S. T. Dawkins, U. G. Poschinger, R. Nigmatullin, A. Retzker, M. B. Plenio, F. Schmidt-Kaler, and K. Singer, Observation of the Kibble-Zurek scaling law for defect formation in ion crystals, *Nat. Commun.* **4**, 2290 (2013).
- [28] K. Pyka, J. Keller, H. L. Partner, R. Nigmatullin, T. Burgermeister, D. M. Meier, K. Kuhlmann, A. Retzker, M. B. Plenio, W. H. Zurek, A. del Campo, and T. E. Mehlstäubler, Topological defect formation and spontaneous symmetry breaking in ion Coulomb crystals, *Nat. Commun.* **4**, 2291 (2013).
- [29] M. Mielenz, J. Brox, S. Kahra, G. Leschhorn, M. Albert, T. Schaetz, H. Landa, and B. Reznik, Trapping of Topological-Structural Defects in Coulomb Crystals, *Phys. Rev. Lett.* **110**, 133004 (2013).
- [30] S. Ejtemaee and P. C. Haljan, Spontaneous nucleation and dynamics of kink defects in zigzag arrays of trapped ions, *Phys. Rev. A* **87**, 051401(R) (2013).
- [31] D. H. E. Dubin, Theory of Structural Phase Transitions in a Trapped Coulomb Crystal, *Phys. Rev. Lett.* **71**, 2753 (1993).
- [32] J. P. Schiffer, Phase Transitions in Anisotropically Confined Ionic Crystals, *Phys. Rev. Lett.* **70**, 818 (1993).
- [33] S. Fishman, G. De Chiara, T. Calarco, and G. Morigi, Structural phase transitions in low-dimensional ion crystals, *Phys. Rev. B* **77**, 064111 (2008).
- [34] G. Piacente, G. Q. Hai, and F. M. Peeters, Continuous structural transitions in quasi-one-dimensional classical Wigner crystals, *Phys. Rev. B* **81**, 024108 (2010).
- [35] I. García-Mata, O. Zhirov, and D. Shepelyansky, Frenkel-Kontorova model with cold trapped ions, *Eur. Phys. J. D* **41**, 325 (2007).
- [36] A. Benassi, A. Vanossi, and E. Tosatti, Nanofriction in cold ion traps, *Nat. Commun.* **2**, 236 (2011).
- [37] D. Mandelli, A. Vanossi, and E. Tosatti, Stick-slip nanofriction in trapped cold ion chains, *Phys. Rev. B* **87**, 195418 (2013).
- [38] S. Aubry, The twist map, the extended Frenkel-Kontorova model and the devil's staircase, *Physica D* **7**, 240 (1983).
- [39] Z.-X. Gong, G.-D. Lin, and L.-M. Duan, Temperature-Driven Structural Phase Transition for Trapped Ions and a Proposal for Its Experimental Detection, *Phys. Rev. Lett.* **105**, 265703 (2010).
- [40] J. Li, L. L. Yan, L. Chen, Z. C. Liu, F. Zhou, J. Q. Zhang, W. L. Yang, and M. Feng, Ion-crystal demonstration of a temperature-driven structural phase transition, *Phys. Rev. A* **99**, 063402 (2019).
- [41] G. Birkl, S. Kassner, and H. Walther, Multiple-shell structures of laser-cooled  $^{24}\text{Mg}^+$  ions in a quadrupole storage ring, *Nature* **357**, 310 (1992).
- [42] G. Piacente, I. V. Schweigert, J. J. Betouras, and F. M. Peeters, Generic properties of a quasi-one-dimensional classical Wigner crystal, *Phys. Rev. B* **69**, 045324 (2004).
- [43] A. Steane, The ion trap quantum information processor, *Appl. Phys. B* **64**, 623 (1997).
- [44] D. G. Enzer, M. M. Schauer, J. J. Gomez, M. S. Gulley, M. H. Holzschleiter, P. G. Kwiat, S. K. Lamoreaux, C. G. Peterson, V. D. Sandberg, D. Tupa, A. G. White, R. J. Hughes, and D. F. V. James, Observation of Power-Law Scaling for Phase Transitions in Linear Trapped Ion Crystals, *Phys. Rev. Lett.* **85**, 2466 (2000).
- [45] P. Silvi, T. Calarco, G. Morigi, and S. Montangero, *Ab initio* characterization of the quantum linear-zigzag transition using

- density matrix renormalization group calculations, *Phys. Rev. B* **89**, 094103 (2014).
- [46] D. Podolsky, E. Shimshoni, P. Silvi, S. Montangero, T. Calarco, G. Morigi, and S. Fishman, From classical to quantum criticality, *Phys. Rev. B* **89**, 214408 (2014).
- [47] G. Morigi and S. Fishman, Dynamics of an ion chain in a harmonic potential, *Phys. Rev. E* **70**, 066141 (2004).
- [48] S. Stenholm, The semiclassical theory of laser cooling, *Rev. Mod. Phys.* **58**, 699 (1986).
- [49] E. Shimshoni, G. Morigi, and S. Fishman, Quantum Zigzag Transition in Ion Chains, *Phys. Rev. Lett.* **106**, 010401 (2011).
- [50] S. Sachdev, *Quantum Phase Transitions* (Cambridge University Press, Cambridge, 2000).
- [51] K. Pyka, N. Herschbach, J. Keller, and T. E. Mehlstäubler, A high-precision segmented Paul trap with minimized micromotion for an optical multiple-ion clock, *Appl. Phys. B* **114**, 231 (2014).
- [52] J. Keller, T. Burgermeister, D. Kalincev, A. Didier, A. P. Kulosa, T. Nordmann, J. Kiethe, and T. E. Mehlstäubler, Controlling systematic frequency uncertainties at the  $10^{-19}$  level in linear Coulomb crystals, *Phys. Rev. A* **99**, 013405 (2019).
- [53] B. Liu, K. Avinash, and J. Goree, Transverse Optical Mode in a One-Dimensional Yukawa Chain, *Phys. Rev. Lett.* **91**, 255003 (2003).
- [54] G. Piacente, F. M. Peeters, and J. J. Betouras, Normal modes of a quasi-one-dimensional multichain complex plasma, *Phys. Rev. E* **70**, 036406 (2004).
- [55] G. Morigi and J. Eschner, Doppler cooling of a Coulomb crystal, *Phys. Rev. A* **64**, 063407 (2001).
- [56] R. Kubo, M. Toda, and N. Hashitsume, *Statistical Physics II: Nonequilibrium Statistical Mechanics*, Vol. 31 (Springer Science & Business Media, Berlin, Heidelberg, 2012).
- [57] P. Hänggi, P. Talkner, and M. Borkovec, Reaction-rate theory: Fifty years after Kramers, *Rev. Mod. Phys.* **62**, 251 (1990).
- [58] H. L. Partner, R. Nigmatullin, T. Burgermeister, K. Pyka, J. Keller, A. Retzker, M. B. Plenio, and T. E. Mehlstäubler, Dynamics of topological defects in ion Coulomb crystals, *New J. Phys.* **15**, 103013 (2013).
- [59] J.-B. Delfau, C. Coste, and M. Saint Jean, Noisy zigzag transition, fluctuations, and thermal bifurcation threshold, *Phys. Rev. E* **87**, 062135 (2013).
- [60] H. A. Kramers, Brownian motion in a field of force and the diffusion model of chemical reactions, *Physica* **7**, 284 (1940).
- [61] A. Retzker, R. C. Thompson, D. M. Segal, and M. B. Plenio, Double well Potentials and Quantum Phase Transitions in Ion Traps, *Phys. Rev. Lett.* **101**, 260504 (2008).
- [62] G. De Chiara, A. del Campo, G. Morigi, M. B. Plenio, and A. Retzker, Spontaneous nucleation of structural defects in inhomogeneous ion chains, *New J. Phys.* **12**, 115003 (2010).
- [63] Y. Ibaraki, U. Tanaka, and S. Urabe, Detection of parametric resonance of trapped ions for micromotion compensation, *Appl. Phys. B* **105**, 219 (2011).
- [64] S. Bergamini, B. Darquié, M. Jones, L. Jacubowicz, A. Browaeys, and P. Grangier, Holographic generation of micro-trap arrays for single atoms by use of a programmable phase modulator, *J. Opt. Soc. Am. B* **21**, 1889 (2004).
- [65] P. Zupancic, P. M. Preiss, R. Ma, A. Lukin, M. E. Tai, M. Rispoli, R. Islam, and M. Greiner, Ultra-precise holographic beam shaping for microscopic quantum control, *Opt. Express* **24**, 13881 (2016).
- [66] C. Marquet, F. Schmidt-Kaler, and D. F. V. James, Phonon-phonon interactions due to non-linear effects in a linear ion trap, *Appl. Phys. B* **76**, 199 (2003).
- [67] H. Kaufmann, S. Ulm, G. Jacob, U. Poschinger, H. Landa, A. Retzker, M. B. Plenio, and F. Schmidt-Kaler, Precise Experimental Investigation of Eigenmodes in a Planar Ion Crystal, *Phys. Rev. Lett.* **109**, 263003 (2012).
- [68] D. J. Wineland, J. Dalibard, and C. Cohen-Tannoudji, Sisyphus cooling of a bound atom, *J. Opt. Soc. Am. B* **9**, 32 (1992).
- [69] S. Ejtemaee and P. C. Haljan, 3D Sisyphus Cooling of Trapped Ions, *Phys. Rev. Lett.* **119**, 043001 (2017).
- [70] M. K. Joshi, A. Fabre, C. Maier, T. Brydges, D. Kiesenhofer, H. Hainzer, R. Blatt, and C. F. Roos, Polarization-gradient cooling of 1D and 2D ion Coulomb crystals, *New J. Phys.* **22**, 103013 (2020).
- [71] G. Morigi, J. Eschner, and C. H. Keitel, Ground State Laser Cooling Using Electromagnetically Induced Transparency, *Phys. Rev. Lett.* **85**, 4458 (2000).
- [72] G. Morigi, Cooling atomic motion with quantum interference, *Phys. Rev. A* **67**, 033402 (2003).
- [73] R. Lechner, C. Maier, C. Hempel, P. Jurcevic, B. P. Lanyon, T. Monz, M. Brownnutt, R. Blatt, and C. F. Roos, Electromagnetically-induced-transparency ground-state cooling of long ion strings, *Phys. Rev. A* **93**, 053401 (2016).
- [74] N. Scharnhorst, J. Cerrillo, J. Kramer, I. D. Leroux, J. B. Wübena, A. Retzker, and P. O. Schmidt, Experimental and theoretical investigation of a multimode cooling scheme using multiple electromagnetically-induced-transparency resonances, *Phys. Rev. A* **98**, 023424 (2018).
- [75] E. Jordan, K. A. Gilmore, A. Shankar, A. Safavi-Naini, J. G. Bohnet, M. J. Holland, and J. J. Bollinger, Near Ground-State Cooling of Two-Dimensional Trapped-Ion Crystals with More than 100 Ions, *Phys. Rev. Lett.* **122**, 053603 (2019).
- [76] J. Kiethe, R. Nigmatullin, T. Schmirander, D. Kalincev, and T. E. Mehlstäubler, Nanofriction and motion of topological defects in self-organized ion Coulomb crystals, *New J. Phys.* **20**, 123017 (2018).
- [77] L. Timm, H. Weimer, L. Santos, and T. E. Mehlstäubler, Energy localization in an atomic chain with a topological soliton, *Phys. Rev. Res.* **2**, 033198 (2020).
- [78] H. Landa, S. Marcovitch, A. Retzker, M. B. Plenio, and B. Reznik, Quantum Coherence of Discrete Kink Solitons in Ion Traps, *Phys. Rev. Lett.* **104**, 043004 (2010).
- [79] H. Landa, A. Retzker, T. Schaeetz, and B. Reznik, Entanglement Generation Using Discrete Solitons in Coulomb Crystals, *Phys. Rev. Lett.* **113**, 053001 (2014).
- [80] A. Shankar, C. Tang, M. Affolter, K. Gilmore, D. H. E. Dubin, S. Parker, M. J. Holland, and J. J. Bollinger, Broadening of the drumhead-mode spectrum due to in-plane thermal fluctuations of two-dimensional trapped ion crystals in a Penning trap, *Phys. Rev. A* **102**, 053106 (2020).

## 5 Summary and Outlook

In this thesis two structural phase transitions in ion Coulomb crystals at finite temperatures were investigated. The existence of the pinning-to-sliding transition for a finite system in an ion Coulomb crystal with a topological defect was demonstrated, allowing for further research of nanofriction between two atomic chains with intrinsic back action. The linear-to-zigzag transition was studied with respect to the temperature-dependent dynamics of the low-frequency vibrational spectrum, yielding a simple analytical model that describes the experimentally observed frequency shifts.

It was shown, that the pinning-to-sliding transition in the presented system (P1) exhibits a soft mode, a symmetry breaking, and the breaking of analyticity of the hull function at the transition. The symmetry-breaking was quantified by an order parameter, which exhibited a critical exponent of approximately 0.5, independent of the ion number, agreeing with calculations for the finite size FK model [37]. In the symmetry-broken regime, jumps between the multiple ground states of the crystal were observed. These ground states were identified with the Peierls-Nabarro potential [35] for the topological defects [67]. The overall potential confines the extended defects in the crystal, and exhibits periodic ground states. The periodicity of the zigzag crystal roughly defines the distance between neighboring ground states and is on the order of  $20 \mu\text{m}$ . Near the crystal center four reachable ground states exist, while in the experiment, most of the time only the two central ground states were occupied, see P1.

The soft mode of the pinning-to-sliding transition is the low-frequency topological defect mode [69]. The measurement of the soft mode frequency showed a finite value at the expected transition point, limited by the crystal's temperature. This was the first direct measurement of the low-frequency mode of the extended topological defect in an ICC. In numerical simulations, a direct dependence of the observed soft mode frequency on the temperature was found. From these simulations, it is estimated that a crystal temperature of  $50 \mu\text{K}$  might allow for the observation of the soft mode. Parallel to the above experiments, a measurement of the high-frequency defect mode was carried out in [83] by parametric excitation of the trapping potential. The excitation of the high-frequency mode led to nonlinear coupling to other modes that ultimately ejected the topological defect from the crystal in a preferred direction. The defects exit was analyzed in the context of directed transport with thermal activation, also known as a ratchet mechanism [84].

Two types of extended defects, the horizontal and vertical defect, were presented in P2. They have a distinct local structure by which they can be identified. Additionally, a differentiation by the ion density per chain is possible. For example, in a 30-ion crystal the horizontal defect shows two more ions in one chain, while the vertical defect shows the same number of ions per chain. The horizontal defect is necessary for the possible observation of the soft mode at the pinning-to-sliding transition. In contrast, the vertical defect mode does not exhibit a soft mode

behavior. This is due to the difference of the Peierls-Nabarro potential for the two defects at the transition. In the sliding phase, the global minimum of the Peierls-Nabarro potential for both defects is in the crystal center, where the topological defects are located. In the pinning phase, the Peierls-Nabarro potential for the horizontal defect has a local maximum in the crystal center, while the vertical defect has a local minimum. Only when the defects are on a local maximum can the soft mode be observed.

It was found, that the two defects can be locally morphed into the other type by employing differential forces. This leads to a shear motion between two ion chains of the 2D ICC along the axial direction, meaning one chain moving to the left, while the opposite chain moves to the right. Incidentally, this movement is similar to the mode vector of the topological defect mode. This shear movement can be used as a sensor for differential forces, as the frequency of the defect mode near the pinning-to-sliding transition changes drastically under them. Based on the measurement resolution, a differential force of just  $6 \times 10^{-24}$  N could be detected with the current experimental setup, if the crystal can be cooled near the vibrational ground state. This illustrates the sensitivity ion Coulomb crystals can achieve with regards to sensing forces [85].

In order to develop an analytical model that describes the thermal influence, the soft mode of the linear-to-zigzag transition, i.e. the transverse zigzag mode, was investigated in P3. In the experiment, the finite temperature of the crystal lead to a non-zero mode frequency at the transition, and jumps between the two ground-state configurations in the 2D phase, similar to the experimental results at the pinning-to-sliding transition. The jumps are a consequence of the stochastic process of thermal activation over the barrier separating the two ground states [86]. The likelihood of a jump can be characterized by the average dwelling time in one ground state, which can be compared to the characteristic period of the soft mode. This allows the differentiation between two regimes, one with less than one jump per soft-mode period and one regime with one or more jumps per period. In the latter regime, the average position of the crystal is that of the linear chain.

Based on this observation an analytical model was devised that extends the harmonic normal mode picture, by expanding the potential energy around the linear chain up to 4th order, even for trapping frequencies for which the crystal would be in the zigzag phase. With a time separation approach, the high frequency modes were averaged out. The resulting averaged interaction terms lead to an effective frequency shift of the two relevant modes, which are the breathing and the zigzag mode. These shifted frequencies agreed well with the numerical and experimental results.

The frequency shifts and the jumps between the two ground states are both manifestations of the crossover region between the linear and zigzag phase, where the system switches continuously between these two phases. From the model it also follows, that near ground state cooling of a soft mode in the vicinity of symmetry-breaking transition requires the cooling of high-frequency modes, as those strongly interact with the soft mode. If only the soft mode is cooled, the high-frequency modes would still induce a frequency shift due to their thermal amplitude. This might hinder experiments that want to utilize a soft mode near a phase transitions [69, 70]. While the presented model can only make predictions for the influence of the high-frequency modes on the soft and breathing mode, the mode interaction does generally go both ways. This might allow cooling of high-frequency modes via cooling of the soft mode near the LZT, similar to what was carried out in Ref. [87].

---

In future theory work, this analytical model could be adapted to the pinning-to-sliding transition. Here, the challenge lies in the presence of more than two possible ground states [67, 68]. They might invalidate the assumption that the ground state configuration of the sliding regime is the average crystal configuration for the symmetry-broken phase under thermal noise. Also the existence of a high frequency localized defect mode, that strongly couples to the soft mode of the transition [83], might hinder the time separation approach employed at the linear-to-zigzag transition. The analytical model could be extended to include micromotion by using the Floquet method [88, 89]. Currently, the model only considers non-resonant averaged interactions between modes. Resonant mode couplings with single quanta have been described previously [90] and extending that model to thermal states, might allow an alternative description of temperature effects presented in P3.

In future experiments, the implementation of near ground state cooling of many ions using, for example, electromagnetically-induced transparency cooling [91–93] or polarization-gradient cooling [94–96] is needed. This would allow for measurement of the soft modes at both the pinning-to-sliding and linear-to-zigzag transition. Additionally, this will open up experimental research into the quantum effects of friction [97, 98], and heat transport under the presence of a topological defect [70]. These novel experiments will require direct experimental determination of the ions temperature, e.g., by thermometry using electromagnetically-induced transparency on the Doppler cooling transition in  $^{172}\text{Yb}^+$ , similar to what was shown for  $^{88}\text{Sr}^+$  [99]. Additionally, the frequency measurement method using resonant light force modulation, can be extended by employing single ion addressing, which would allow the excitation of any mode. Using a shaped beam profile for the excitation laser, such as those generated by spatial light modulators [100, 101], might lead to experiments with arbitrary mode excitation in order to study the interaction between modes.



# Acronyms

**ICC** ion Coulomb crystal

**FK** Frenkel-Kontorova

**PST** pinning to sliding transition

**2D** two-dimensional

**LZT** linear to zigzag transition





# Bibliography

- [1] D. H. E. Dubin and T. O’Neil, “Trapped nonneutral plasmas, liquids, and crystals (the thermal equilibrium states)”, *Rev. Mod. Phys.* **71**, 87 (1999), DOI: 10.1103/RevModPhys.71.87.
- [2] F. Diedrich, E. Peik, J. M. Chen, W. Quint, and H. Walther, “Observation of a phase transition of stored laser-cooled ions”, *Phys. Rev. Lett.* **59**, 2931 (1987), DOI: 10.1103/PhysRevLett.59.2931.
- [3] D. J. Wineland, J. C. Bergquist, W. M. Itano, J. J. Bollinger, and C. H. Manney, “Atomic-ion Coulomb clusters in an ion trap”, *Phys. Rev. Lett.* **59**, 2935 (1987), DOI: 10.1103/PhysRevLett.59.2935.
- [4] C. D. Bruzewicz, J. Chiaverini, R. McConnell, and J. M. Sage, “Trapped-ion quantum computing: Progress and challenges”, *Applied Physics Reviews* **6**, 021314 (2019), DOI: 10.1063/1.5088164.
- [5] P. Schindler et al., “A quantum information processor with trapped ions”, *New J. Phys.* **15**, 123012 (2013), DOI: 10.1088/1367-2630/15/12/123012.
- [6] K. Wright et al., “Benchmarking an 11-qubit quantum computer”, *Nat. Commun.* **10**, 5464 (2019), DOI: 10.1038/s41467-019-13534-2.
- [7] C. Champenois, M. Marciante, J. Pedregosa-Gutierrez, M. Houssin, M. Knoop, and M. Kajita, “Ion ring in a linear multipole trap for optical frequency metrology”, *Phys. Rev. A* **81**, 043410 (2010), DOI: 10.1103/PhysRevA.81.043410.
- [8] J. B. Wübbena, S. Amairi, O. Mandel, and P. O. Schmidt, “Sympathetic cooling of mixed-species two-ion crystals for precision spectroscopy”, *Phys. Rev. A* **85**, 043412 (2012), DOI: 10.1103/PhysRevA.85.043412.
- [9] N. Herschbach, K. Pyka, J. Keller, and T. E. Mehlstäubler, “Linear Paul trap design for an optical clock with Coulomb crystals”, *Appl. Phys. B* **107**, 891–906 (2012), DOI: 10.1007/s00340-011-4790-y.
- [10] K. Arnold, E. Hajiyev, E. Paez, C. H. Lee, M. D. Barrett, and J. Bollinger, “Prospects for atomic clocks based on large ion crystals”, *Phys. Rev. A* **92**, 032108 (2015), DOI: 10.1103/PhysRevA.92.032108.
- [11] J. Keller, T. Burgermeister, D Kalincev, A. Didier, A. P. Kulosa, T. Nordmann, J. Kiethe, and T. E. Mehlstäubler, “Controlling systematic frequency uncertainties at the  $10^{-19}$  level in linear Coulomb crystals”, *Phys. Rev. A* **99**, 013405 (2019), DOI: 10.1103/PhysRevA.99.013405.

- [12] N. Ohtsubo, Y. Li, K. Matsubara, N. Nemitz, H. Hachisu, T. Ido, and K. Hayasaka, “Optical clock based on a sympathetically-cooled indium ion”, *Hyperfine Interact* **240**, 39 (2019), DOI: 10.1007/s10751-019-1585-8.
- [13] S. M. Brewer, J.-S. Chen, A. M. Hankin, E. R. Clements, C. W. Chou, D. J. Wineland, D. B. Hume, and D. R. Leibbrandt, “ $^{27}\text{Al}^+$  Quantum-Logic Clock with a Systematic Uncertainty below  $10^{-18}$ ”, *Phys. Rev. Lett.* **123**, 033201 (2019), DOI: 10.1103/PhysRevLett.123.033201.
- [14] S.-J. Chao, K.-F. Cui, S.-M. Wang, J. Cao, H.-L. Shu, and X.-R. Huang, “Observation of  $^1S_0 \rightarrow ^3P_0$  Transition of a  $^{40}\text{Ca}^+ - ^{27}\text{Al}^+$  Quantum Logic Clock”, *Chinese Physics Letters* **36**, 120601 (2019), DOI: 10.1088/0256-307x/36/12/120601.
- [15] Z. Y. Ma et al., “Investigation of experimental issues concerning successful operation of quantum-logic-based  $^{27}\text{Al}^+$  ion optical clock”, *Applied Physics B* **126**, 129 (2020), DOI: 10.1007/s00340-020-07479-4.
- [16] M. S. Safronova, D. Budker, D. DeMille, D. F. J. Kimball, A. Derevianko, and C. W. Clark, “Search for new physics with atoms and molecules”, *Rev. Mod. Phys.* **90**, 025008 (2018), DOI: 10.1103/revmodphys.90.025008.
- [17] R. Blatt and C. F. Roos, “Quantum simulations with trapped ions”, *Nat. Phys.* **8**, 277–284 (2012), DOI: 10.1038/nphys2252.
- [18] R. Matjeschk, C. Schneider, M. Enderlein, T. Huber, H. Schmitz, J. Glueckert, and T. Schaetz, “Experimental simulation and limitations of quantum walks with trapped ions”, *New J. Phys.* **14**, 035012 (2012), DOI: 10.1088/1367-2630/14/3/035012.
- [19] K. Toyoda, Y. Matsuno, A. Noguchi, S. Haze, and S. Urabe, “Experimental realization of a quantum phase transition of polaritonic excitations”, *Phys. Rev. Lett.* **111**, 160501 (2013), DOI: 10.1103/PhysRevLett.111.160501.
- [20] E. A. Martinez et al., “Real-time dynamics of lattice gauge theories with a few-qubit quantum computer”, *Nature* **534**, 516–519 (2016), DOI: 10.1038/nature18318.
- [21] J. Zhang, G. Pagano, P. W. Hess, A. Kyprianidis, P. Becker, H. Kaplan, A. V. Gorshkov, Z.-X. Gong, and C. Monroe, “Observation of a many-body dynamical phase transition with a 53-qubit quantum simulator”, *Nature* **551**, 601–604 (2017), DOI: 10.1038/nature24654.
- [22] X. Zhang et al., “Experimental quantum simulation of fermion-antifermion scattering via boson exchange in a trapped ion”, *Nat. Commun.* **9**, 195 (2018), DOI: 10.1038/s41467-017-02507-y.
- [23] D. Leibfried, R. Blatt, C. Monroe, and D. Wineland, “Quantum dynamics of single trapped ions”, *Rev. Mod. Phys.* **75**, 281–324 (2003), DOI: 10.1103/RevModPhys.75.281.

- 
- [24] A. Vanossi, N. Manini, M. Urbakh, S. Zapperi, and E. Tosatti, “Colloquium: Modeling friction: From nanoscale to mesoscale”, *Rev. Mod. Phys.* **85**, 529 (2013), DOI: 10.1103/RevModPhys.85.529.
- [25] S. Kumar and M. S. Li, “Biomolecules under mechanical force”, *Phys. Rep.* **486**, 1–74 (2010), DOI: 10.1016/j.physrep.2009.11.001.
- [26] A. K. Sieradzan, A. Niemi, and X. Peng, “Peierls-Nabarro barrier and protein loop propagation”, *Phys. Rev. E* **90**, 062717 (2014), DOI: 10.1103/PhysRevE.90.062717.
- [27] Y. Mo, K. T. Turner, and I. Szlufarska, “Friction laws at the nanoscale”, *Nature* **457**, 1116–1119 (2009), DOI: 10.1038/nature07748.
- [28] V. Bormuth, V. Varga, J. Howard, and E. Schäffer, “Protein friction limits diffusive and directed movements of kinesin motors on microtubules”, *Science* **325**, 870–873 (2009), DOI: 10.1126/science.1174923.
- [29] U. Seifert, “Stochastic thermodynamics, fluctuation theorems and molecular machines”, *Rep. Prog. Phys.* **75**, 126001 (2012), DOI: 10.1088/0034-4885/75/12/126001.
- [30] T. Kudernac, N. Ruangsapapichat, M. Parschau, B. Maciá, N. Katsonis, S. R. Harutyunyan, K.-H. Ernst, and B. L. Feringa, “Electrically driven directional motion of a four-wheeled molecule on a metal surface”, *Nature* **479**, 208–211 (2011), DOI: 10.1038/nature10587.
- [31] M. Dienwiebel, G. S. Verhoeven, N. Pradeep, J. W. M. Frenken, J. A. Heimberg, and H. W. Zandbergen, “Superlubricity of Graphite”, *Phys. Rev. Lett.* **92**, 126101 (2004), DOI: 10.1103/PhysRevLett.92.126101.
- [32] L. Prandtl, “Ein Gedankenmodell zur kinetischen Theorie der festen Körper”, *Z. Angew. Math. Mech.* **8**, 85–106 (1928), DOI: 10.1002/zamm.19280080202.
- [33] G. Tomlinson, “A molecular theory of friction”, *Philos. Mag.* **7**, 905–939 (1929), DOI: 10.1080/14786440608564819.
- [34] T. Kontorova and Y. Frenkel, “The model of dislocation in solid body”, *Zh. Eksp. Teor. Fiz* **8**, 1340–1348 (1938).
- [35] O. M. Braun and Y. S. Kivshar, *The Frenkel-Kontorova Model: Concepts, Methods, and Applications*, Berlin, Heidelberg: Springer Science & Business Media, 2004, DOI: 10.1007/978-3-662-10331-9.
- [36] S. Aubry, “The twist map, the extended Frenkel-Kontorova model and the devil’s staircase”, *Physica D* **7**, 240–258 (1983), DOI: 10.1016/0167-2789(83)90129-X.
- [37] Y. Braiman, J. Baumgarten, J. Jortner, and J. Klafter, “Symmetry-breaking transition in finite Frenkel-Kontorova chains”, *Phys. Rev. Lett.* **65**, 2398 (1990), DOI: 10.1103/PhysRevLett.65.2398.

- [38] M. Peyrard and S. Aubry, “Critical behaviour at the transition by breaking of analyticity in the discrete Frenkel-Kontorova model”, *J. Phys. C: Solid State Phys.* **16**, 1593 (1983), DOI: 10.1088/0022-3719/16/9/005.
- [39] M. Hirano, K. Shinjo, R. Kaneko, and Y. Murata, “Observation of Superlubricity by Scanning Tunneling Microscopy”, *Phys. Rev. Lett.* **78**, 1448 (1997), DOI: 10.1103/PhysRevLett.78.1448.
- [40] S. Kawai et al., “Superlubricity of graphene nanoribbons on gold surfaces”, *Science* **351**, 957–961 (2016), DOI: 10.1126/science.aad3569.
- [41] I. García-Mata, O. V. Zhirov, and D. L. Shepelyansky, “Frenkel-Kontorova model with cold trapped ions”, *Eur. Phys. J. D* **41**, 325–330 (2007), DOI: 10.1140/epjd/e2006-00220-2.
- [42] A. Benassi, A. Vanossi, and E. Tosatti, “Nanofriction in cold ion traps”, *Nat. Commun.* **2**, 236 (2011), DOI: 10.1038/ncomms1230.
- [43] D. Mandelli, A. Vanossi, and E. Tosatti, “Stick-slip nanofriction in trapped cold ion chains”, *Phys. Rev. B* **87**, 195418 (2013), DOI: 10.1103/PhysRevB.87.195418.
- [44] A. Bylinskii, D. Gangloff, and V. Vuletić, “Tuning friction atom-by-atom in an ion-crystal simulator”, *Science* **348**, 1115–1118 (2015), DOI: 10.1126/science.1261422.
- [45] A. Bylinskii, D. Gangloff, I. Counts, and V. Vuletić, “Observation of Aubry-type transition in finite atom chains via friction”, *Nat. Mater.* **15**, 717–721 (2016), DOI: 10.1038/nmat4601.
- [46] D. Gangloff, A. Bylinskii, I. Counts, W. Jhe, and V. Vuletić, “Velocity tuning of friction with two trapped atoms”, *Nat. Phys.* **11**, 915–919 (2015), DOI: 10.1038/nphys3459.
- [47] I. Counts, D. Gangloff, A. Bylinskii, J. Hur, R. Islam, and V. Vuletić, “Multislip Friction with a Single Ion”, *Phys. Rev. Lett.* **119**, 043601 (2017), DOI: 10.1103/PhysRevLett.119.043601.
- [48] D. A. Gangloff, A. Bylinskii, and V. Vuletić, “Kinks and nanofriction: Structural phases in few-atom chains”, *Phys. Rev. Research* **2**, 013380 (2020), DOI: 10.1103/PhysRevResearch.2.013380.
- [49] T. Bohlein, J. Mikhael, and C. Bechinger, “Observation of kinks and antikinks in colloidal monolayers driven across bordered surfaces”, *Nat. Mater.* **11**, 126–130 (2011), DOI: 10.1038/nmat3204.
- [50] T. Brazda, A. Silva, N. Manini, A. Vanossi, R. Guerra, E. Tosatti, and C. Bechinger, “Experimental Observation of the Aubry Transition in Two-Dimensional Colloidal Monolayers”, *Phys. Rev. X* **8**, 011050 (2018), DOI: 10.1103/PhysRevX.8.011050.

- 
- [51] H. Matsukawa and H. Fukuyama, “Theoretical study of friction: One-dimensional clean surfaces”, *Phys. Rev. B* **49**, 17286 (1994), DOI: 10.1103/PhysRevB.49.17286.
- [52] F. Kühner, J. Morfill, R. A. Neher, K. Blank, and H. E. Gaub, “Force-induced DNA Slippage”, *Biophys. J.* **92**, 2491–2497 (2007), DOI: 10.1529/biophysj.106.095836.
- [53] A. Ward, F. Hilitski, W. Schwenger, D. Welch, A. W. C. Lau, V. Vitelli, L. Mahadevan, and Z. Dogic, “Solid friction between soft filaments”, *Nat. Mater.* **14**, 583–588 (2015), DOI: 10.1038/nmat4222.
- [54] J. Kiethe, R. Nigmatullin, D. Kalincev, T. Schmirander, and T. E. Mehlstäubler, “Probing nanofriction and Aubry-type signatures in a finite self-organized system”, *Nat. Commun.* **8**, 15364 (2017), DOI: 10.1038/ncomms15364.
- [55] D. H. E. Dubin, “Theory of structural phase transitions in a trapped Coulomb crystal”, *Phys. Rev. Lett.* **71**, 2753 (1993), DOI: 10.1103/PhysRevLett.71.2753.
- [56] J. P. Schiffer, “Phase transitions in anisotropically confined ionic crystals”, *Phys. Rev. Lett.* **70**, 818 (1993), DOI: 10.1103/PhysRevLett.70.818.
- [57] A. del Campo, G. De Chiara, G. Morigi, M. B. Plenio, and A. Retzker, “Structural Defects in Ion Chains by Quenching the External Potential: The Inhomogeneous Kibble-Zurek Mechanism”, *Phys. Rev. Lett.* **105**, 075701 (2010), DOI: 10.1103/PhysRevLett.105.075701.
- [58] M. Mielenz, J. Brox, S. Kahra, G. Leschhorn, M. Albert, T. Schaetz, H. Landa, and B. Reznik, “Trapping of Topological-Structural Defects in Coulomb Crystals”, *Phys. Rev. Lett.* **110**, 133004 (2013), DOI: 10.1103/PhysRevLett.110.133004.
- [59] S. Ejtemaee and P. C. Haljan, “Spontaneous nucleation and dynamics of kink defects in zigzag arrays of trapped ions”, *Phys. Rev. A* **87**, 051401(R) (2013), DOI: 10.1103/PhysRevA.87.051401.
- [60] K. Pyka et al., “Topological defect formation and spontaneous symmetry breaking in ion Coulomb crystals”, *Nat. Commun.* **4**, 2291 (2013), DOI: 10.1038/ncomms3291.
- [61] S. Ulm et al., “Observation of the Kibble-Zurek scaling law for defect formation in ion crystals”, *Nat. Commun.* **4**, 2290 (2013), DOI: 10.1038/ncomms3290.
- [62] M. Cetina, A. Bylinskii, L. Karpa, D. Gangloff, K. M. Beck, Y. Ge, M. Scholz, A. T. Grier, I. Chuang, and V. Vuletić, “One-dimensional array of ion chains coupled to an optical cavity”, *New J. Phys.* **15**, 053001 (2013), DOI: 10.1088/1367-2630/15/5/053001.
- [63] L. Karpa, A. Bylinskii, D. Gangloff, M. Cetina, and V. Vuletić, “Suppression of Ion Transport due to Long-Lived Subwavelength Localization by an Optical Lattice”, *Phys. Rev. Lett.* **111**, 163002 (2013), DOI: 10.1103/physrevlett.111.163002.

- [64] T. W. Kibble, “Topology of cosmic domains and strings”, *J. Phys. A: Math. Gen.* **9**, 1387 (1976), DOI: 10.1088/0305-4470/9/8/029.
- [65] W. H. Zurek, “Cosmological experiments in superfluid helium?”, *Nature* **317**, 505–508 (1985), DOI: /10.1038/317505a0.
- [66] H. Landa, B. Reznik, J. Brox, M. Mielenz, and T. Schaetz, “Structure, dynamics and bifurcations of discrete solitons in trapped ion crystals”, *New J. Phys.* **15**, 093003 (2013), DOI: 10.1088/1367-2630/15/9/093003.
- [67] H. L. Partner, R. Nigmatullin, T. Burgermeister, K. Pyka, J. Keller, A. Retzker, M. B. Plenio, and T. E. Mehlstäubler, “Dynamics of topological defects in ion Coulomb crystals”, *New J. Phys.* **15**, 103013 (2013), DOI: 10.1088/1367-2630/15/10/103013.
- [68] J. Kiethe, R. Nigmatullin, T. Schmirander, D. Kalincev, and T. E. Mehlstäubler, “Nanofriction and motion of topological defects in self-organized ion Coulomb crystals”, *New J. Phys.* **20**, 123017 (2018), DOI: 10.1088/1367-2630/aaf3d5.
- [69] H. Landa, S. Marcovitch, A. Retzker, M. B. Plenio, and B. Reznik, “Quantum Coherence of Discrete Kink Solitons in Ion Traps”, *Phys. Rev. Lett.* **104**, 043004 (2010), DOI: 10.1103/PhysRevLett.104.043004.
- [70] L. Timm, H. Weimer, L. Santos, and T. E. Mehlstäubler, “Energy localization in an atomic chain with a topological soliton”, *Phys. Rev. Research* **2**, 033198 (2020), DOI: 10.1103/PhysRevResearch.2.033198.
- [71] D. J. Berkeland, J. D. Miller, J. C. Bergquist, W. M. Itano, and D. J. Wineland, “Minimization of ion micromotion in a Paul trap”, *J. Appl. Phys.* **83**, 5025–5033 (1998), DOI: 10.1063/1.367318.
- [72] K. Pyka, N. Herschbach, J. Keller, and T. E. Mehlstäubler, “A high-precision segmented Paul trap with minimized micromotion for an optical multiple-ion clock”, *Appl. Phys. B* **114**, 231–241 (2014), DOI: 10.1007/s00340-013-5580-5.
- [73] J. Keller, D. Kalincev, T. Burgermeister, A. P. Kulosa, A. Didier, T. Nordmann, J. Kiethe, and T. E. Mehlstäubler, “Probing Time Dilation in Coulomb Crystals in a High-Precision Ion Trap”, *Phys. Rev. Applied* **11**, 011002 (2019), DOI: 10.1103/PhysRevApplied.11.011002.
- [74] G. Birkl, S. Kassner, and H. Walther, “Multiple-shell structures of laser-cooled  $^{24}\text{Mg}^+$  ions in a quadrupole storage ring”, *Nature* **357**, 310 (1992), DOI: 10.1038/357310a0.
- [75] D. G. Enzer et al., “Observation of Power-Law Scaling for Phase Transitions in Linear Trapped Ion Crystals”, *Phys. Rev. Lett.* **85**, 2466 (2000), DOI: 10.1103/PhysRevLett.85.2466.
- [76] G. Morigi and S. Fishman, “Dynamics of an ion chain in a harmonic potential”, *Phys. Rev. E* **70**, 066141 (2004), DOI: 10.1103/PhysRevE.70.066141.

- 
- [77] S. Fishman, G. De Chiara, T. Calarco, and G. Morigi, “Structural phase transitions in low-dimensional ion crystals”, *Phys. Rev. B* **77**, 064111 (2008), DOI: 10.1103/PhysRevB.77.064111.
- [78] J. Kiethe, L. Timm, H. Landa, D. Kalincev, G. Morigi, and T. E. Mehlstäubler, “Finite-temperature spectrum at the symmetry-breaking linear to zigzag transition”, *Phys. Rev. B* **103**, 104106 (2021), DOI: 10.1103/physrevb.103.104106.
- [79] Z.-X. Gong, G.-D. Lin, and L.-M. Duan, “Temperature-Driven Structural Phase Transition for Trapped Ions and a Proposal for its Experimental Detection”, *Phys. Rev. Lett.* **105**, 265703 (2010), DOI: 10.1103/PhysRevLett.105.265703.
- [80] J. B. Delfau, C. Coste, C. Even, and M. Saint Jean, “Single-file diffusion of interacting particles in a finite-sized channel”, *Phys. Rev. E* **82**, 031201 (2010), DOI: 10.1103/PhysRevE.82.031201.
- [81] J.-B. Delfau, C. Coste, and M. Saint Jean, “Noisy zigzag transition, fluctuations, and thermal bifurcation threshold”, *Phys. Rev. E* **87**, 062135 (2013), DOI: 10.1103/PhysRevE.87.062135.
- [82] J.-B. Delfau, C. Coste, and M. Saint Jean, “Transverse single-file diffusion near the zigzag transition”, *Phys. Rev. E* **87**, 032163 (2013), DOI: 10.1103/PhysRevE.87.032163.
- [83] J. Brox, P. Kiefer, M. Bujak, T. Schaetz, and H. Landa, “Spectroscopy and Directed Transport of Topological Solitons in Crystals of Trapped Ions”, *Phys. Rev. Lett.* **119**, 153602 (2017), DOI: 10.1103/physrevlett.119.153602.
- [84] M. Salerno and N. R. Quintero, “Soliton ratchets”, *Phys. Rev. E* **65**, 025602(R) (2002), DOI: 10.1103/physreve.65.025602.
- [85] M. J. Biercuk, H. Uys, J. W. Britton, A. P. VanDevender, and J. J. Bollinger, “Ultrasensitive detection of force and displacement using trapped ions”, *Nat. Nanotechnol.* **5**, 646–650 (2010), DOI: 10.1038/nnano.2010.165.
- [86] P. Hänggi, P. Talkner, and M. Borkovec, “Reaction-rate theory: fifty years after Kramers”, *Rev. Mod. Phys.* **62**, 251–341 (1990), DOI: 10.1103/RevModPhys.62.251.
- [87] D. J. Gorman, P. Schindler, S. Selvarajan, N. Daniilidis, and H. Häffner, “Two-mode coupling in a single-ion oscillator via parametric resonance”, *Phys. Rev. A* **89**, 062332 (2014), DOI: 10.1103/PhysRevA.89.062332.
- [88] H. Landa, M. Drewsen, B. Reznik, and A. Retzker, “Modes of oscillation in radiofrequency Paul traps”, *New J. Phys.* **14**, 093023 (2012), DOI: 10.1088/1367-2630/14/9/093023.
- [89] H. Kaufmann, S. Ulm, G. Jacob, U. Poschinger, H. Landa, A. Retzker, M. B. Plenio, and F. Schmidt-Kaler, “Precise Experimental Investigation of Eigenmodes in a Planar Ion Crystal”, *Phys. Rev. Lett.* **109**, 263003 (2012), DOI: 10.1103/PhysRevLett.109.263003.

- [90] C. Marquet, F. Schmidt-Kaler, and D. F. V. James, “Phonon–phonon interactions due to non-linear effects in a linear ion trap”, *Appl. Phys. B* **76**, 199–208 (2003), DOI: 10.1007/s00340-003-1097-7.
- [91] G. Morigi, J. Eschner, and C. H. Keitel, “Ground State Laser Cooling Using Electromagnetically Induced Transparency”, *Phys. Rev. Lett.* **85**, 4458 (2000), DOI: 10.1103/PhysRevLett.85.4458.
- [92] R. Lechner, C. Maier, C. Hempel, P. Jurcevic, B. P. Lanyon, T. Monz, M. Brownnutt, R. Blatt, and C. F. Roos, “Electromagnetically-induced-transparency ground-state cooling of long ion strings”, *Phys. Rev. A* **93**, 053401 (2016), DOI: 10.1103/PhysRevA.93.053401.
- [93] N. Scharnhorst, J. Cerrillo, J. Kramer, I. D. Leroux, J. B. Wübbena, A. Retzker, and P. O. Schmidt, “Experimental and theoretical investigation of a multimode cooling scheme using multiple electromagnetically-induced-transparency resonances”, *Phys. Rev. A* **98**, 023424 (2018), DOI: 10.1103/physreva.98.023424.
- [94] D. J. Wineland, J. Dalibard, and C. Cohen-Tannoudji, “Sisyphus cooling of a bound atom”, *J. Opt. Soc. Am. B* **9**, 32–42 (1992), DOI: 10.1364/josab.9.000032.
- [95] S. Ejtemaee and P. C. Haljan, “3D Sisyphus Cooling of Trapped Ions”, *Phys. Rev. Lett.* **119**, 043001 (2017), DOI: 10.1103/PhysRevLett.119.043001.
- [96] M. K. Joshi, A. Fabre, C. Maier, T. Brydges, D. Kiesenhofer, H. Hainzer, R. Blatt, and C. F. Roos, “Polarization-gradient cooling of 1D and 2D ion Coulomb crystals”, *New J. Phys.* **22**, 103013 (2020), ISSN: 1367-2630, DOI: 10.1088/1367-2630/abb912.
- [97] T. Zanca, F. Pellegrini, G. E. Santoro, and E. Tosatti, “Frictional lubricity enhanced by quantum mechanics”, *Proc. Natl. Acad. Sci.* **115**, 3547–3550 (2018), DOI: 10.1073/pnas.1801144115.
- [98] P. M. Bonetti, A. Rucci, M. L. Chiofalo, and V. Vuletić, “Quantum effects in the Aubry transition”, *Phys. Rev. Research* **3**, 013031 (2021), DOI: 10.1103/physrevresearch.3.013031.
- [99] V. Tugayé, J.-P. Likforman, S. Guibal, and L. Guidoni, “Absolute single-ion thermometry”, *Phys. Rev. A* **99**, 023412 (2019), DOI: 10.1103/physreva.99.023412.
- [100] S. Bergamini, B. Darquié, M. Jones, L. Jacubowicz, A. Browaeys, and P. Grangier, “Holographic generation of microtrap arrays for single atoms by use of a programmable phase modulator”, *J. Opt. Soc. Am. B* **21**, 1889–1894 (2004), DOI: 10.1364/JOSAB.21.001889.
- [101] P. Zupancic, P. M. Preiss, R. Ma, A. Lukin, M. E. Tai, M. Rispoli, R. Islam, and M. Greiner, “Ultra-precise holographic beam shaping for microscopic quantum control”, *Opt. Express* **24**, 13881–13893 (2016), DOI: 10.1364/OE.24.013881.



- [102] H. Kurzke, J. Kiethe, A. Heuer, and A. Jechow, “Frequency doubling of incoherent light from a superluminescent diode in a periodically poled lithium niobate waveguide crystal”, *Laser Phys. Lett.* **14**, 055402 (2017), DOI: 10.1088/1612-202x/aa6889.
- [103] J. Kiethe, A. Heuer, and A. Jechow, “Second-order coherence properties of amplified spontaneous emission from a high-power tapered superluminescent diode”, *Laser Phys. Lett.* **14**, 086201 (2017), DOI: 10.1088/1612-202x/aa772c.



# Acknowledgments

At this point I would like to thank the many people that helped getting me to here. It certainly became a long list.

First, I would like to thank Tanja Mehlstäubler for offering me the opportunity to work on this project and for pushing me on, when needed. I truly enjoyed the discussions we had, even when the topic was not physics. I would also like to extend my thanks to Luis Santos and Michael Johanning for agreeing to referee this manuscript and to Klemens Hammerer for (once again) agreeing to be the chair for a PhD defense from QUEST.

I would not have finished my thesis if not for my colleagues in the laboratory. I thank Dimitri Kalincev for the long nights we spent in the lab trying to get the ion crystals to behave and for pushing on with measurements, when I already wanted to give up. Thank you, also to Jonas Keller, who introduced me to the experiment and for helpful discussion at (almost) any stage of my time. From Jonas, I inherited the oversight of our experimental control software when he left, which in an interesting turn of events I have now effectively given back to him. I thank Tobias Burgermeister for the help in the lab and the breaks in the Laue-Bau kitchen, where we tried to beat the records of the Perplexus labyrinth. I would also like to thank Tabea Nordmann, for the time spent building a new experimental setup. Hopefully, neither of us will stay until 6 a.m. again to install a trap. Since I started, many people joined the QUEST FG 2 and all of them helped me at some point, even if our overlap was short. My thanks also to the following colleagues in no particular order: Andre Kulosa, Alexandre Didier, Henning Fürst, Laura Dreissen, Indy Yeh, Nimrod Hausser, Hongli Liu, Daniel Vadlejš, Elena Jordan, Erik Jansson, Luca Rüffert, Lars Timm, Daniel Bennet and Nishant Bhatt.

During my PhD I also had help from several students and interns. I would like to thank Henrik Wingerath, Thorben Schmirander, Nimrod Hausser, Kai Dietze and Liza Surzhikova for always asking the questions I could not answer, allowing me to learn through you. Thank you to the interns Lars Timm and Michel Niklas-Senn for your help with simulations. A thanks also goes to the FWJ students for their help with many small and large projects: Achim Byl, Leander Thiessen, Kathrina Dudde, Ole Henseler, Michel Wolf and Angelika Klär.

I would also like to thank the other members of the QUEST institute, with no specific order: Piet Schmidt, Lennart Pelzer, Stephan Hannig, Kai Dietze, Fabian Wolf, Jan-Christoph Heip, Max Zawierucha, Steven King, Tobias Leopold, Peter Micke, Christian Ospelkaus, Henning Hahn and Giorgio Zarantonello. Special thanks to Johannes Kramer and Nils Scharnhorst for the many hours of escapism that we shared.

Not only did you help me by supporting me with work related tasks, but also by spending time outside of it, to cope with the stress and live life. I hope at some point we can get back together to play games or just spent a nice evening at a bar again.

It would not have been possible without the technical support from the mechanics workshop

Rebecca Müller, Leeroy Paulmann and Jan Rechenberg, and electronics workshops Burghard Lipphardt, Andreas Hoppmann, Peter Carstens, Julia Fenske, Nikolai Beev, David Weber and Tjeerd Pinkert. Also a big thank you to the administrative staff at QUEST Sandra Ludwig, Sina Bußmann, Katja Rosignol and Kathrin Reiff, who help with purchasing, travels and contracts, as well as Birgit Ohlendorf in Hanover for handling the PhD related bureaucracy.

I was lucky enough to be involved in many collaborations over the years. I would like to thank Hayasaka Kazuhiro and Nozomi Ohtsubo for their hospitality in Tokio. I especially express my gratitude to Ramil Nigmatullin, Haggai Landa and Giovanna Morigi for their theoretical insight and help with our joint publications.

Thanks, Henning and Nishant, for the feedback on the manuscript.

Last, but definitely not least, I would like to thank my family and friends for their support. Without my parents that always encouraged me to go on, and that allowed and supported me to freely choose what I want to do, I would not have gotten to the point of handing in this thesis. If I have forgotten to mention anyone here explicitly, I apologize, and thank you.

# Curriculum Vitae

## Jan Kiethe

### Personal Data

|                |                              |
|----------------|------------------------------|
| date of birth  | 26.10.1988, Dresden, Germany |
| nationality    | German                       |
| marital status | unmarried                    |

### Education

|            |  |
|------------|--|
|            | University   |
| 2015–today | <b>Doctorate</b> , <i>Physikalisch-Technische Bundesanstalt</i> , Braunschweig |
| 2011–2014  | <b>Master of Science</b> , Physics, <i>Universität Potsdam</i> , Potsdam       |
| 2008–2011  | <b>Bachelor of Science</b> , Physics, <i>Universität Potsdam</i> , Potsdam     |
|            | School   |
| 1999–2008  | <b>Abitur</b> , <i>Gesamtschule Bergheim</i> , Quadrath-Ichendorf              |

### Master thesis

|             |  |
|-------------|--|
| title:      | <i>Experimentelle Charakterisierung der zeitlichen Intensitätskorrelationen der Emission einer Superlumineszenzdiode mit Trapezgeometrie</i> |
| supervisor: | Prof. Dr. R. Menzel  |

### Bachelor thesis

|             |   |
|-------------|---|
| title:      | <i>Untersuchungen zur induzierten Kohärenz ohne induzierte Emission</i> |
| supervisor: | Prof. Dr. R. Menzel   |

## Publications

- [1] J. Kiethe, R. Nigmatullin, D. Kalincev, T. Schmirander, and T. E. Mehlstäubler, “Probing nanofriction and Aubry-type signatures in a finite self-organized system”, *Nat. Commun.* **8**, 15364 (2017), DOI: 10.1038/ncomms15364
- [2] H. Kurzke, J. Kiethe, A. Heuer, and A. Jechow, “Frequency doubling of incoherent light from a superluminescent diode in a periodically poled lithium niobate waveguide crystal”, *Laser Phys. Lett.* **14**, 055402 (2017), DOI: 10.1088/1612-202x/aa6889
- [3] J. Kiethe, A. Heuer, and A. Jechow, “Second-order coherence properties of amplified spontaneous emission from a high-power tapered superluminescent diode”, *Laser Phys. Lett.* **14**, 086201 (2017), DOI: 10.1088/1612-202x/aa772c
- [4] J. Kiethe, R. Nigmatullin, T. Schmirander, D. Kalincev, and T. E. Mehlstäubler, “Nanofriction and motion of topological defects in self-organized ion Coulomb crystals”, *New J. Phys.* **20**, 123017 (2018), DOI: 10.1088/1367-2630/aaf3d5
- [5] J. Keller, T. Burgermeister, D. Kalincev, A. Didier, A. P. Kulosa, T. Nordmann, J. Kiethe, and T. E. Mehlstäubler, “Controlling systematic frequency uncertainties at the  $10^{-19}$  level in linear Coulomb crystals”, *Phys. Rev. A* **99**, 013405 (2019), DOI: 10.1103/PhysRevA.99.013405
- [6] J. Keller, D. Kalincev, T. Burgermeister, A. P. Kulosa, A. Didier, T. Nordmann, J. Kiethe, and T. E. Mehlstäubler, “Probing Time Dilation in Coulomb Crystals in a High-Precision Ion Trap”, *Phys. Rev. Applied* **11**, 011002 (2019), DOI: 10.1103/PhysRevApplied.11.011002
- [7] J. Kiethe, L. Timm, H. Landa, D. Kalincev, G. Morigi, and T. E. Mehlstäubler, “Finite-temperature spectrum at the symmetry-breaking linear to zigzag transition”, *Phys. Rev. B* **103**, 104106 (2021), DOI: 10.1103/physrevb.103.104106